Study on Photo-functional Properties of Lanthanide Coordination Polymers Linked with Metal Ions

Masanori Yamamoto

Graduate School of Chemical Sciences and Engineering

Hokkaido University

CONTENTS

CHAPTER 4

CHAPTER 5

Chapter 1

General Introduction

1.1 Optical science technology in modern society

1.1.1 Development of optical technology

In modern society, advanced information technology are provided the convenience and safety for our lives. Information society is supported by the state-of-the-art information-communication technology. Various materials and products related to information communication technology exist close to our lives. In particular, optical functional materials which have been researched and developed in the fields of photochemistry, electrochemistry, and magnetochemistry are enable to transmission of a large amount of information and high-speed processing of information. In further advancement of information-communication technology, the research and development of optical functional materials will be greatly contributed to the future information society (Figure 1-1).

Optical functional materials are used for many products, including lighting,

displays, and optical fibers. Among them, luminescent materials are used for organic EL elements, optical sensors and so on. Inorganic fluorescent materials that composed of transition metal or lanthanide elements, and organic fluorescent materials which composed of organic molecules or polymers, are mainly used as raw materials of luminescent materials. In recent years, lanthanide complexes with organic molecule ligands as an inorganic material have been actively researched. Our laboratory have succeeded in development of lanthanide complexes that show strong emission by combination of lanthanide ions and ligands. Furthermore, these reported lanthanide complexes have been attracted attention as next-generation luminescent materials.

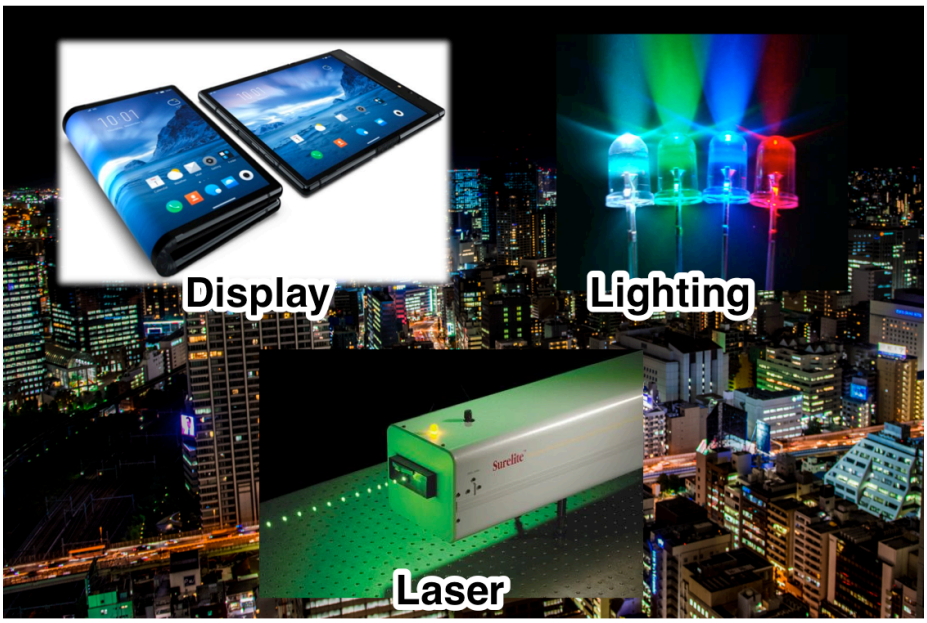

Figure 1-1. Application of optical functional materials.

1.1.2 Classification of luminescent materials

The luminescent materials are classified into two types. One is an inorganic luminescent material that composed of oxides, nitrides, and sulfides ceramics containing transition metals and lanthanide elements. The other is an organic luminescent material, which is mainly composed of carbon C, hydrogen H, and a few heteroatoms (Figure1-2).

Typical examples of inorganic luminescent materials are as follow. $SrAl_2O_4$ doped lanthanide elements such as Eu, Nd and Dy is known to a long-lasting phosphor.[1,2] $(SrCaBaMg)_5(PO4)_3Cl$:Eu, $LaPO_4$:CeTb and Y_2O_3:Eu are coated on the inner glass of fluorescent lamp.[3] SiAlON derivative ceramics are shown a high brightness phosphor by developed of National Institute for Materials Science (NIMS).[4,5]

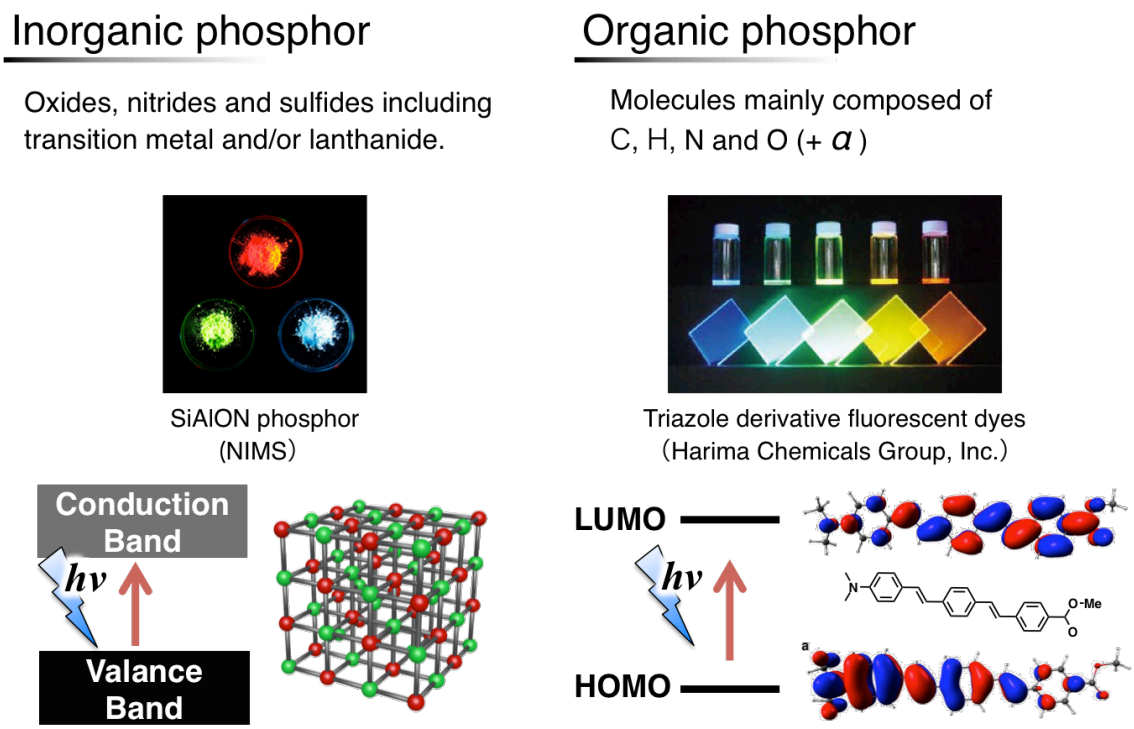

Figure 1-2. Inorganic and organic luminescent material.

Typical organic luminescent materials are shown in Figure 1-3. Organic luminescent materials are molecules with extended π-conjugation system. The organic molecules such as fluorescein, coumarin, Rhodamine and BODIPY derivatives[6-14] are known to excellent fluorescent dyes with high absorption coefficient, quantum yield and photostability. These fluorescent dye derivatives have been developed for novel bio-marker and emitting layer. The luminescent polymer such as poly(p-phenylene vinylene) (PPV), polyfluorene (PFO) and polythiophene (PT) derivatives[15-19] are applied to organic emitting layers for organic light emitting displays (OLED). On the other hand, the metal complex is composed of metal ion and organic molecules. In general, transition metal complexes with the d^6 and d^{10} electron configuration and lanthanide (III) complexes with f-f transition are widely known for the emitting materials.

In this thesis, the author deals with metal complex in organic luminescent materials. In the 1.3 and 1.4, general properties of metal complexes were described.

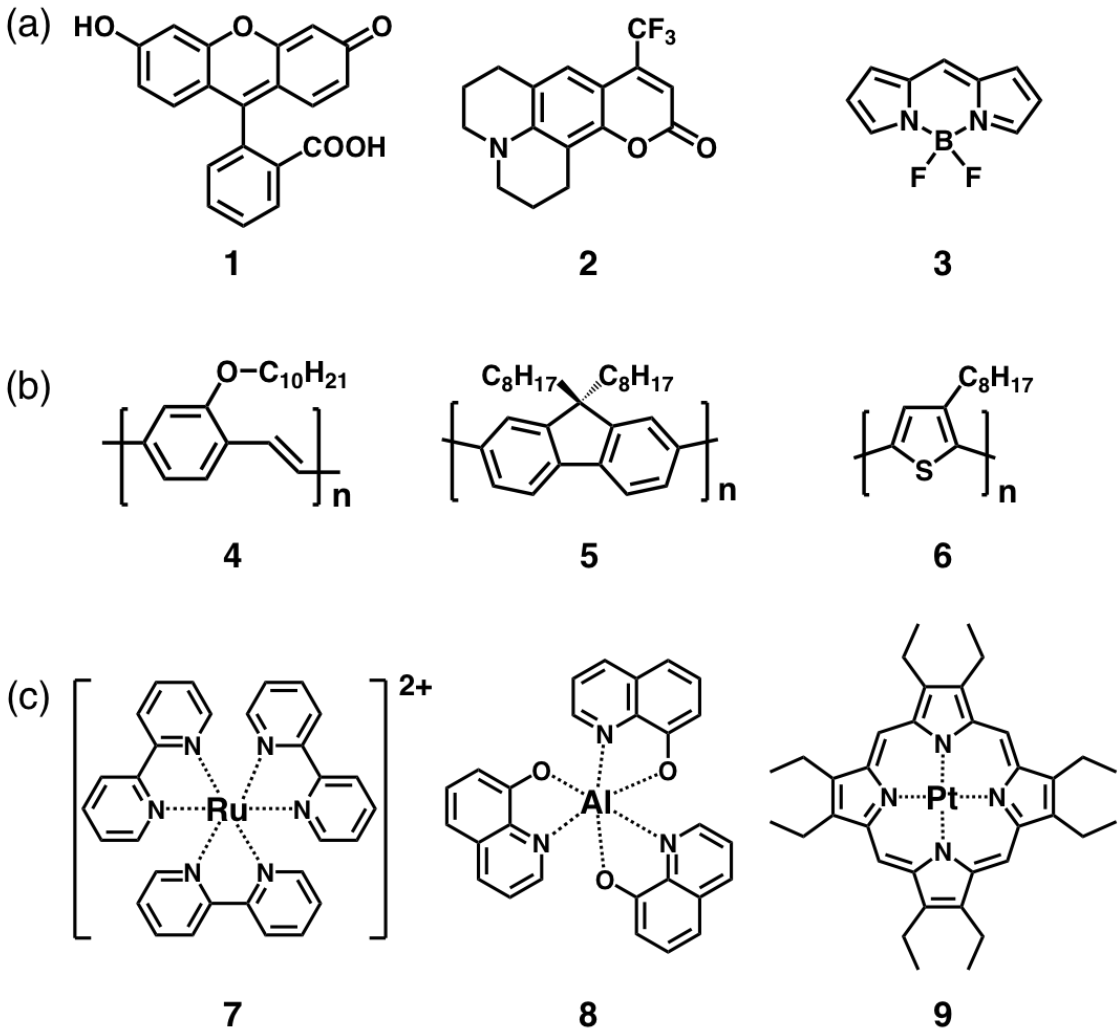

Figure 1-3. Luminescent materials of organic molecules and metal complexes.

1: fluorescein, 2: coumarin153, 3: BODIPY core structure,

4: poly(2-decyloxy-1,4-phenylene), 5: poly(9,9-dioctylfluoren), 6: poly(3-octylthiophene),

7: $[Ru(bpy)_3]^{2+}$, 8: Alq_3, 9: PtOEP

1.2 Introduction of photophysical properties

1.2.1 Emission mechanism of organic luminescent materials

To emit luminescence of molecules, it is necessary to have a large absorb ability and electronic transition corresponding to ultraviolet and visible regions (200 - 800 nm). The Jablonski diagram is shown in Figure 1-4, which is useful for explaining the emission mechanism of molecules. In general, the most stable state of molecules at room temperature is the ground states (S_0). Molecules absorb ultraviolet or visible light, resulting in excited singlet states (S_1). Many organic molecules emit the light from S_1 state, and return to S_0 state. The emission process between the same spin states ($\Delta S = 0$) is called "fluorescence". The features of fluorescence are as follows, (i) the absorption maximum wavelength and the fluorescence maximum wavelength are close (the Stokes shift is small), and (ii) the emission lifetime is short (> ns). Generally, it is known that the Stokes shift of organic molecule is smaller than that of metal complexes.

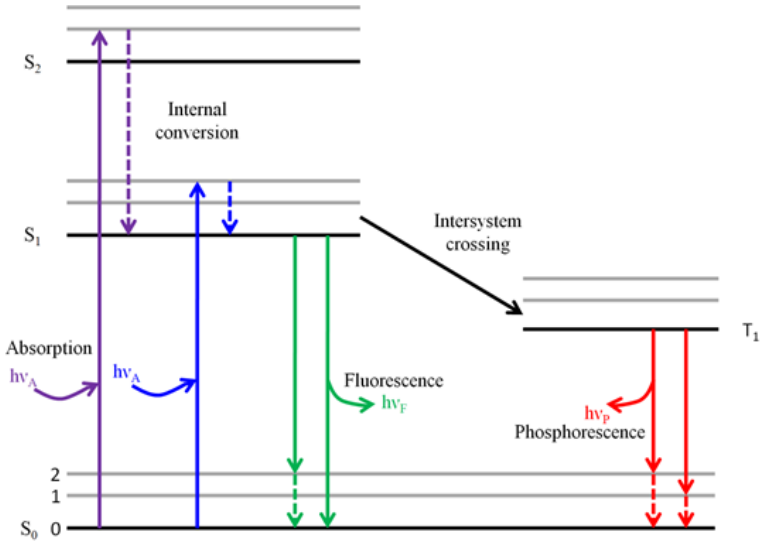

Figure 1-4. Jablonski diagram showing various processes following absorption of light.

On the other hand, the molecule with heavy atoms such as metal complexes absorbs excitation energy with ligand and become the excited singlet state (S_1). Then, the excited triplet state (T_1) is occurs quickly though intersystem crossing. (In the case of metal complexes, electronic spin reversal is occurred which spin orbit interaction called "heavy atom effect".) The molecule that excited to high energy states oscillates to stable vibration states at high speeds, and the lowest excited triplet state is occurred by internally convert. (Generally, emission and photo-reaction occur from the lowest excited state, which is called the Kasha rule.)[20] Therefore, in metal complexes, luminescence when returning from the lowest excited triplet state (T_1) to the base singlet state (S_0) is often observed. The emission process between different spin states is called "phosphorescence" ($\Delta S > 0$; $\Delta S = 1$ in the case of emission from the excited triplet state). Phosphorescence may be observed with organic molecules under low temperature conditions. The feature of phosphorescence is as follows, (i) the influence of reabsorption is small, because the difference between the absorption maximum and the emission maximum is large. (ii) The emission lifetime is long (generally from ns - ms order). In the case of many phosphorescent materials, (iii) temperature control is important because of temperature dependency. This is because there are many nonradiative velocity levels that can thermally transition from the excited triplet state.

1.2.2 Evaluation of photophysical propaties

There are four types of significant physical quantities to evaluate photophysical properties of luminescent materials, which are radiative rate constant k_r, non-radiative rate constant k_{nr}, emission lifetime τ and emission quantum yield Φ, respectively.[21] Each photophysical quantity is explained as follows. The k_r is the rate constant of the deactivation process returning from the excited state to the ground state with luminescence (fluorescence or phosphorescence). On the other hand, the k_{nr} is the rate constant of the othere deactivation process returning to the ground state without luminescence. The k_{nr} includes thermal relaxation of molecules and energy transfer to another excited state.

These two rate constants are estimated by measurements of the emission lifetime τ and the emission quantum yield Φ. The emission lifetime τ are determined by measuring the time-dependent emission intensity F(t) in the electron transition from the excited state to the ground state. The time-dependent emission intensity F(t) is given by the following equation.

$$F(t) = F_0^* \exp\left(-\frac{t}{t}\right) \qquad 1.1$$

Here, F_0* is the emission intensity at t = 0, and τ is the emission lifetime. Normally, the τ is expressed by the following equation using k_r and k_{nr}.

$$\tau = \frac{1}{k_r + k_{nr}} \qquad 1.2$$

The emission quantum yield Φ is defined as the ratio of the number of emitted photons $PN(em)$ to the number of absorbed photons $PN(abs)$. [22]

$$\Phi = \frac{PN(em)}{PN(abs)} \quad 1.3$$

Equation 1.3 is also expressed using k_r and k_{nr} as follows.

$$\Phi = \frac{k_r}{k_r + k_{nr}} \quad 1.4$$

The Φ is expressed by the ratio of the total rate constants (k_r + k_{nr}) to the k_{nr}.

1.3 Metal complexes and coordination polymers

1.3.1 Basic facts of luminescent metal complexes

Metal complex is defined as "a compound in which organic molecules or ions are coordinated to metal ions". The optical features of metal complexes are different from those of organic luminescent materials. Electronic states of metal complexes are dependent on the combination of metal ions and ligands. Charge transfer transitions of metal complexes are classified into four types as follows (Figure 1-5).[23] (i) Metal-centerd (MC) transition such as d-d or f-f transitions, (ii) Ligand-centerd (LC) transition such as π-π* or n-π* transitions, and charge transfer transition between metal ion and ligands such as (iii) Metal-to-Ligand charge transfer (MLCT) and (iv) Ligand-to-Metal charge transfer (LMCT).

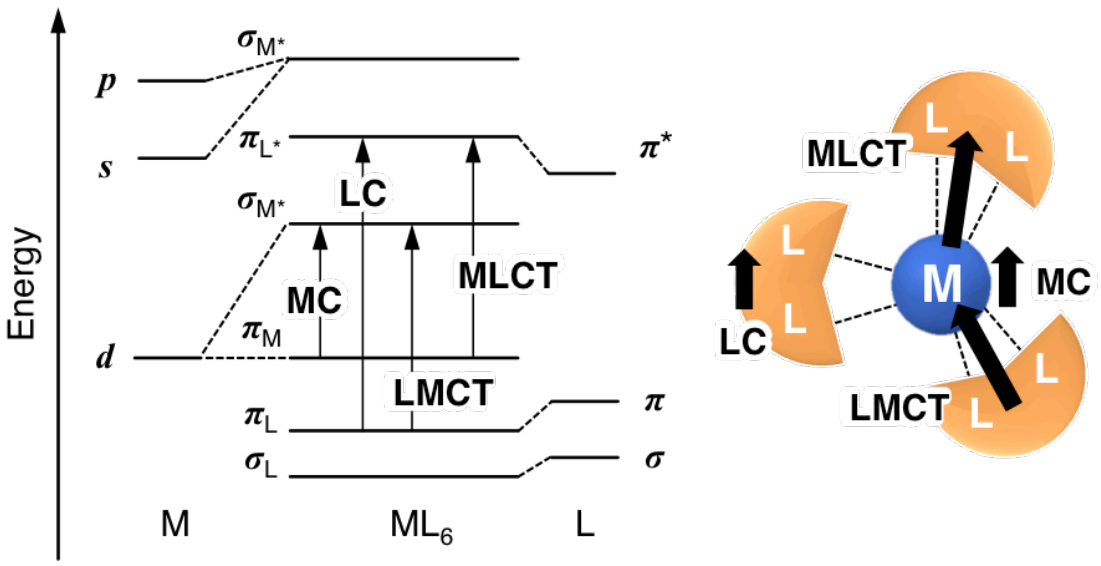

Figure 1-5. Schematic diagram of transition metal complex.

However, the transition probability of d-d and f-f transitions is usually small because of forbidden transition based on the Laporte rule. From these facts, photophysical properties of metal complexes are mainly affected by LC, MLCT and LMCT with large transition probability. The S_1 state of metal complexes is generated by exciting LC, MLCT and LMCT absorption bands. In metal complexes with heavy metal ions, the intersystem crossing process from S_1 to T_1 are enhanced by the heavy atom effect. Therefore, metal complexes are tended to show the phosphorescence.

Ruthenium (II) and iridium (III) complexes of d^6 group, [24-29] and platinum (II) and palladium (II) complexes of the d^8 group[30-33] have been reported as typical luminescent transition metal complexes. Copper (I), silver (I) and gold (I) complexes with d^{10} electron configuration are also known for the emitting materials. [33-38]

1.3.2 Structure of metal complexes based on self-assembly

The structure of metal complexes are classified into mononuclear complexes and polynuclear complexes. The mononuclear complex is composed of one metal ion and a plurality of organic ligands. Metal complexes are the smallest unit of inorganic-organic hybrid materials. The property of metal complexes is determined by the combination of the metal ion and organic ligands. Therefore, the scientific knowledge which were provided by research of mononuclear complexes have led to the discovery of the new electronic structure and property of metal complexes. [24-38]

On the other hand, the polynuclear complex is defined as complex containing a number of metal ions in the molecular unit. Polynuclear complexes are classified into

the following types depending on the coordination structure, (i) molecular polynuclear complexes which a plurality of metal ion are linked with organic ligands, and (ii) metal cluster with metal-metal bonding.[39,40] These polynuclear complex structures are retained within one molecule.

Furthermore, the coordination polymer which is composed of metal ions and bridge organic ligands is also a kind of polynuclear complex. The control of the ligand structure and the coordination structure of metal ions provides to the formation of one-dimensional coordination polymers,[41,42] two-dimensional coordination polymers with planarity, and three-dimensional coordination polymers with strong network structure.[42-47] In particular, the three-dimensional coordination polymer with lattice and pore structure is called metal-organic frameworks (MOF) or porous coordination polymers (PCP).[48] MOF and PCP are actively studied in the research field of inorganic-organic hybrid materials.

Polynuclear complexes provide to novel luminescent materials which are not found in mononuclear complexes by the combination of metal ion and organic ligands. [49-52] In addition, it is possible to enhance the photophysical property and the structural stability of the complex by inter- and intra-molecular interactions. The investigation of polynuclear complex is more important position than that of mononuclear complex by the thought of the diversity and functionality of metal complex.

1.4 Luminescent materials based on lanthanide ions

1.4.1 Characteristics of lanthanide elements

The lanthanide series of chemical elements comprises the 15 metallic chemical elements with atomic numbers 57 through 71, from Lanthanum: La through Lutetium: Lu. These elements, along with the chemically similar element scandium: Sc and yttrium: Y, are often collectively known as the rare earth elements (Figure 1-6). The most stable oxidation state of lanthanide ions is known to be trivalent. [53]

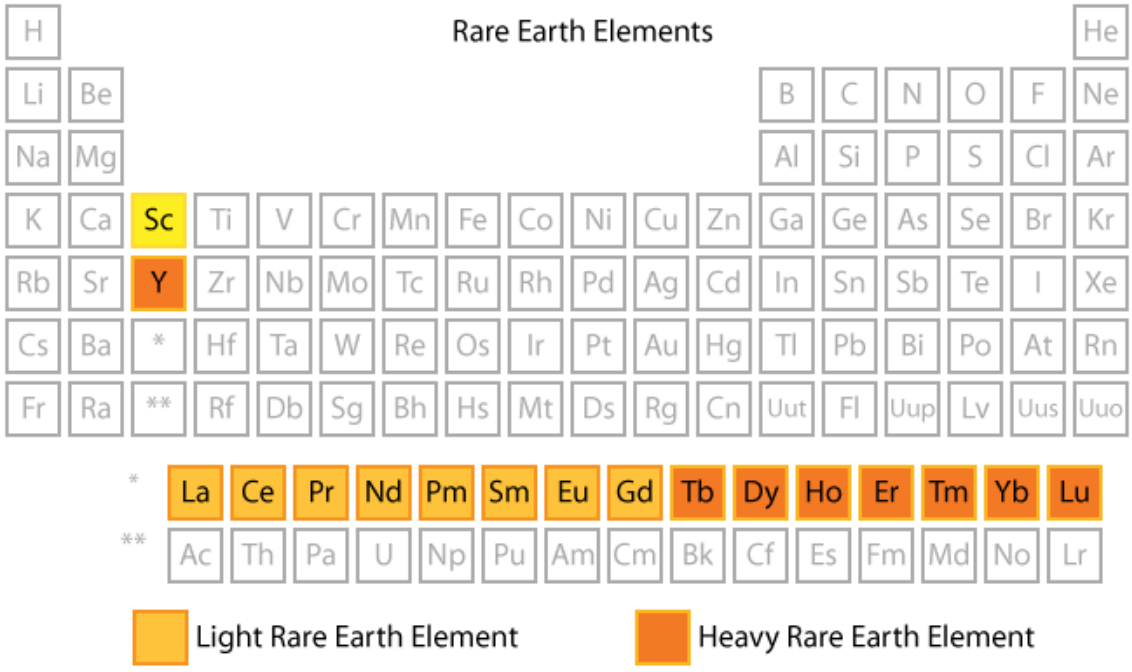

Figure 1-6. Rare earths and lanthanides in the periodic table.

The electronic configurations in neutral and trivalent states of lanthanide ions are summarized in Table 1-1. The specialty of lanthanide elements is owned 4f orbitals. The 4f orbitals, despite that 4f orbital has the highest energy, are not geometrically and structurally outermost shells. The 4f orbitals show special photophysical properties. General features based on the electronic structure of lanthanide ions are summarized in the following three points.

(i). In general, trivalent oxidation state is stable. Trivalent compounds are usually stable especially in aqueous solution. There are divalent states such as europium (Eu) and ytterbium (Yb) and tetravalent states such as cerium (Ce) and terbium (Tb), but these are not as stable as the trivalent state.

(ii). The coordination bond of ligands and lanthanide ions in lanthanide complexes is inclined to form ionic bonding. The replacement reaction of ligands easily occurs.

(iii). The 4f orbital of Ln^{3+}, despite that 4f orbital has the highest energy, is not directly involved in binding with ligands because of shield by 5s and 5p orbitals. Therefore, photophysical and magnetic properties based on lanthanide ions are not significantly affected by ligands and external environments.

Table1-1. Electronic configuration in neutral and trivalent states of lanthanide elements

Element	Atomic number	Neutral state	Trivalent state	Grand states ($^{2S+1}L_J$)
Sc	21	$[Ar]3d^14s^2$	[Ar]	$^1S_0$
Y	39	$[Kr]4d^15s^2$	[Kr]	$^1S_0$
La	57	$[Xe]5d^16s^2$	[Xe]	$^1S_0$
Ce	58	$[Xe]4f^15d^16s^2$	$[Xe]4f^1$	$^2F_{5/2}$
Pr	59	$[Xe]4f^36s^2$	$[Xe]4f^2$	$^3H_4$
Nd	60	$[Xe]4f^46s^2$	$[Xe]4f^3$	$^4I_{9/2}$
Pm	61	$[Xe]4f^56s^2$	$[Xe]4f^4$	$^5I_4$
Sm	62	$[Xe]4f^66s^2$	$[Xe]4f^5$	$^6H_{5/2}$
Eu	63	$[Xe]4f^76s^2$	$[Xe]4f^6$	$^7F_0$
Gd	64	$[Xe]4f^75d^16s^2$	$[Xe]4f^7$	$^8S_{7/2}$
Tb	65	$[Xe]4f^96s^2$	$[Xe]4f^8$	$^7F_6$
Dy	66	$[Xe]4f^{10}6s^2$	$[Xe]4f^9$	$^6H_{15/2}$
Ho	67	$[Xe]4f^{11}6s^2$	$[Xe]4f^{10}$	$^5I_8$
Er	68	$[Xe]4f^{12}6s^2$	$[Xe]4f^{11}$	$^4I_{15/2}$
Tm	69	$[Xe]4f^{13}6s^2$	$[Xe]4f^{12}$	$^3H_6$
Yb	70	$[Xe]4f^{14}6s^2$	$[Xe]4f^{13}$	$^2F_{7/2}$
Lu	71	$[Xe]4f^{14}5d^16s^2$	$[Xe]4f^{14}$	$^1S_0$

1.4.2 Luminescent materials of lanthanide elements

Lanthanide elements have unique photophysical properties to apply to many industrial materials. Application for the first time as industrial products in 1885, lanthanide mixed oxides with mainly Ce^{3+} was applied as the gas mantle which increased brightness to gas lamp. As modern applications, yttrium oxide containing Eu^{3+} (Y_2O_3:Eu) was used as red phosphors of CRT-based television (CRT: cathode-ray tube) in 1964. The importance of lanthanide elements was further raised from this time. In recent years, the applications of lanthanide elements have further expanded to optical materials such as lighting and display and so on.[54] Especially, lanthanide complexes are expected to use for valuable phosphors such as LEDs materials and emitting layer of organic EL materials.[53,54] Utilizing the features of low toxicity and long emission lifetime, the lanthanide complexes are also expected to use for bio-probe materials. [55]

1.4.3 Emission mechanism of lanthanide complexes

The lanthanide complex is composed of a lanthanide ion and organic ligands. Emission bands of lanthanide complexes are depended on metal-center ions, such as Eu^{3+} complexes are red, Tb^{3+} complexes are green, Nd^{3+}, Er^{3+} and Yb^{3+} complexes emit light in the near infrared region (Figure 1-7a and Table 1-2). These emissions bands are derived from 4f-4f transitions of lanthanide ions. [55]

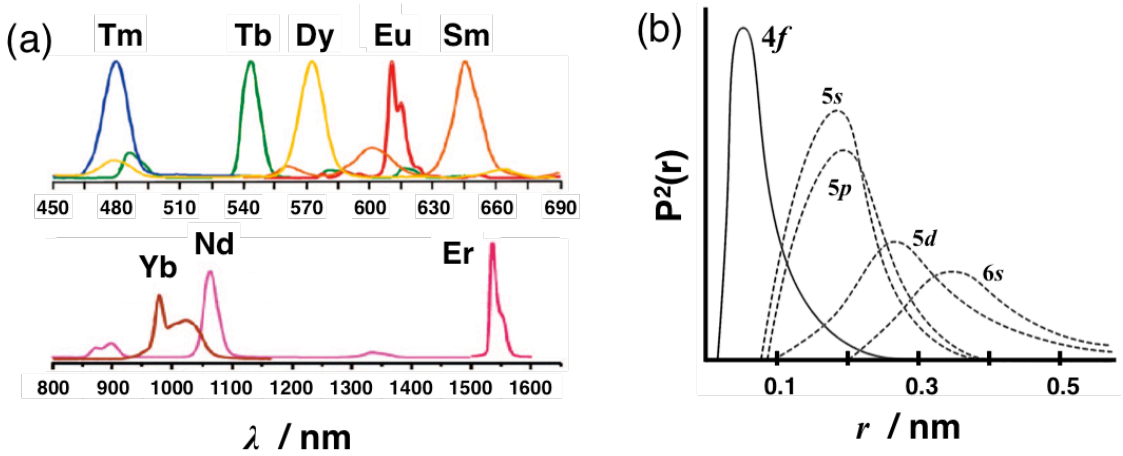

Figure 1-7. (a) Radial part of the wave function of orbitals, (b) Emission spectra of Lanthanide tris(*β*-diketonate) compounds. [55]

The electronic structure of lanthanide ions between ground states and excited states dose not almost change, because the 4f orbitals of lanthanide ions are shielded by 5s or 5p orbitals which located in the outer shell of 4f orbitals (Figure 1-7b). Therefore, the ligand field around lanthanide ions is not affected by organic ligands (the internal shielding effect). Even if the organic ligand changes, the emission bands of lanthanide complexes are not almost change. The lanthanide complexes are shown the high color purity emission bands based on the internal shielding effect.

Table 1-2. Luminescent properties of trivalent lanthanide ions

Element	Grand states	Main electric transition	λ / nm	τ_{rad} / ms
Nd	$^4I_{3/2}$	$^4F_{3/2} \rightarrow {}^4I_J$ (J = 9/2 – 13/2)	900, 1060, 1350	0.42
Sm	$^6H_{5/2}$	$^4G_{5/2} \rightarrow {}^6H_J$ (J = 5/2 – 13/2)	560, 595, 640, 700, 775	6.26
	$^6H_{5/2}$	$^4G_{5/2} \rightarrow {}^6F_J$ (J = 1/2 – 9/2)	870, 887, 926, 1010, 1150	
	$^6H_{5/2}$	$^4G_{5/2} \rightarrow {}^6H_{13/2}$	877	
Eu	$^7F_0$	$^5D_0 \rightarrow {}^7F_J$ (J = 0 – 6)	580, 590, 615, 650, 720, 750, 820	9.7
Gd	$^8S_{7/2}$	$^6P_{7/2} \rightarrow {}^8S_{7/2}$	315	10.9
Tb	$^7F_6$	$^5D_4 \rightarrow {}^7F_J$ (J = 6 – 0)	490, 540, 580, 620, 650, 660, 675	9.0
Dy	$^6F_{15/2}$	$^4F_{9/2} \rightarrow {}^6H_J$ (J = 15/2 – 9/2)	475, 570, 660, 750	1.85
	$^6F_{15/2}$	$^4F_{15/2} \rightarrow {}^6H_J$ (J = 15/2 – 9/2)	455, 540, 615, 695	3.22
Er	$^4I_{15/2}$	$^4S_{3/2} \rightarrow {}^4I_J$ (J = 15/2, 13/2)	545, 850	0.7
	$^4I_{15/2}$	$^4F_{9/2} \rightarrow {}^4I_{15/2}$	660	0.6
	$^4I_{15/2}$	$^4I_{9/2} \rightarrow {}^4I_{15/2}$	810	4.5
	$^4I_{15/2}$	$^4I_{13/2} \rightarrow {}^4I_{15/2}$	1540	0.66
Tm	$^3H_6$	$^1D_2 \rightarrow {}^7F_4, {}^3H_4, {}^3F_3, {}^3F_2$	450, 650, 740, 775	0.09
	$^3H_6$	$^1G_4 \rightarrow {}^3H_6, {}^3F_4, {}^3H_5$	470, 650, 770	1.29
	$^3H_6$	$^3H_4 \rightarrow {}^3H_6$	800	3.6
Yb	$^2F_{7/2}$	$^2F_{5/2} \rightarrow {}^2F_{7/2}$	980	2.0

However, it is difficult to gather the large excitation energy by direct excitation of lanthanide ions, because the 4f -4f transitions are Laporte forbidden. For this reason, lanthanide complexes are introduced organic ligands with a large absorption coefficient to improve the collecting efficiency of excitation energy (antenna effect). The energy transfer mechanism from organic ligands to lanthanide ion is shown in Figure 1- 8. The excited singlet state (S_1) of ligands is generated by photon-excitation, after that, the excited triplet state (T_1) is generated through the intersystem crossing. The excited state of lanthanide ions is formed by energy transfer (intramolecular energy transfer) from the excited triplet state of ligands through the Förster or Dexter electron transfer, and then, the lanthanide ions emit narrow width emission bands.

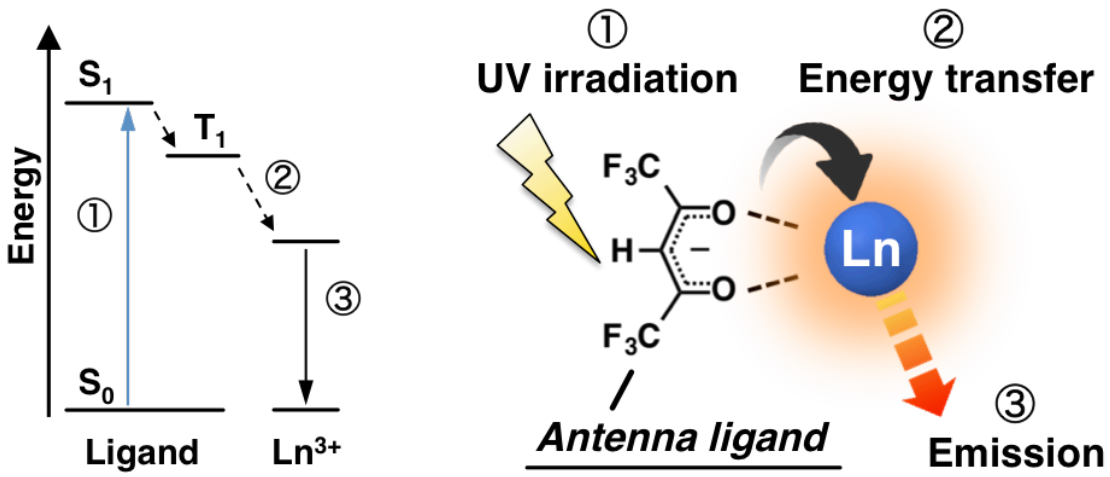

Figure 1-8. Emission mechanism of lanthanide complexes.

1.4.4 Molecular design of enhancement emission in lanthanide complexes

The luminescence of lanthanide complexes based on 4f-4f transitions is dominated by two type deactivation process, which are radiation and non-radiative deactivation process from excited states to ground state in 4f-4f transitions. Therefore, enhancement emission of lanthanide complexes is necessary to increase the radiative rate constant (k_r) and suppress the non-radiative rate constant (k_{nr}).

(i) Asymmetrization of the ligand field: promotion of k_r

The 4f-4f transitions are Laporte forbidden. However, most of the lanthanide complexes show luminescence and sometimes the emission intensity is relatively large. According to the Judd-Ofelt theory that is most famous theory in the field of lanthanide chemistry, admixture of states with opposite parity into the 4f wavefunctions in required for including electric dipole 4f-4f transitions.[56-58] Admixing the opposite states φ_{nl} into the 4f wavefunction $|f^N JM_J>$ via an opposite parity crystal field provides a new wavefunction |B> as shown in following equation.

$$|B\rangle = \frac{|f^N JM_J\rangle + \sum_{\varphi_{nl}} \langle (\langle |f^N JM_J|V|\varphi_{nl}) |\varphi_{nl}\rangle}{E(f^N JM_J) - E(\varphi_{nl})} \qquad 1.5$$

Here, $E(f^N JM_J)$-$E(\varphi_{nl})$ is the energy difference between 4f states and the perturbing opposite parity state and V is the crystal field interaction operator. In general, $4f^{N-1}5d^1$ state admixes into $4f^N$ states because its energy is the closest to the $4f^N$ states. The energy level of $4f^{N-1}5d^1$ state is dependent on crystal and/or ligands fields. Strong ligand

field and low-symmetrical crystal field are expected to provide large splitting.

Hasegawa has proposed that low-symmetrical coordination geometry induces enhancement of 4f-4f transitions probability, directly rerated k_r. According to the reports, the radiative rate constants of Eu^{3+} complexes with eight-coordinate trigonal-dodecahedron (D_{2d}) and nine-coordinate monocapped-square-antiprimatic (C_{4v}) structure are larger than those of eight-coordinatie square-antiprimatic structure (D_{4d}) that is the most typical geometrical structure.[59,60] Low-symmetrical coordination geometry is also expected to provide large radiative rate constant.

(ii) Introduction of low-vibration ligands: suppression of k_{nr}

In general, the non-radiative deactivation process from emission states is dependent on the energy gap between the ground state and the excited state. The non-radiative deactivation process of lanthanide complexes tends to occur, because of the energy gap of lanthanide complexes is smaller than ordinary organic molecules and metal complexes. Therefore, it is important to suppress the non-radiative deactivation process in order to enhancement luminescent of lanthanide complexes.

According to the energy gap theory, the transition probability W_{RT} from the excited state of lanthanide ions to the vibrational levels of solvent molecules is expressed by the following equation. [61]

$$W_{RW} = \left(\frac{2\pi\rho}{\hbar}\right) J^2 F \qquad 1.6$$

Here, ρ is the density of states, J is the overlapping constant of wave functions in

nuclear motion, and *F* is the Franck-Condon factor, respectively. From the above equation, if the *F* value can be decreased, it is possible to suppress energy transfer by vibrational deactivation. Further, this F value is given by the following equation.

$$F = \frac{\exp(-\gamma)\gamma^{v}}{v!} \quad 1.7$$

Here, γ is a variable in oscillator approximation of Hermitian polynomial, and v is oscillation quantum, respectively. The v is the harmonic number of the resonance energy with the energy gap of lanthanide ions. From this equation, the *F* value can be decreased exponentially by increasing the oscillation quantum. In other words, when surrounding the lanthanide ions with ligands containing low vibration bonds such as C-F bonds, the *F* value is decreased and vibrational deactivation can be suppressed. [62]

The Estimation of emission quantum yields in lanthanide complexes are described as follow. In general, the emission quantum yield of lanthanide complexes are evaluated two different physical quantities, the intrinsic quantum yield Φ_{ff} and overall quantum yield Φ_{tot}, respectively. The value of Φ_{ff} indicates the metal-centered luminescence upon direct excitation into the 4f levels. The Φ_{ff} is defined in equation 1.8. [55]

$$\Phi_{ff} = \frac{k_r}{k_r + k_{nr}} = \frac{\tau_{obs}}{\tau_{rad}} \quad 1.8$$

$$\tau_{rad} = \frac{1}{k_r} \quad 1.9$$

$$\tau_{obs} = \frac{1}{k_r + k_{nr}} \quad 1.10$$

where the k_r, k_{nr}, τ_{rad} and τ_{obs} is radiative rate constants, non-radiative constants,

radiative lifetimes and observed lifetimes, respectively. Especially in Eu^{3+} complexes, the value of τ_{rad} is estimated from emission spectra shapes using the following formula. [63,64]

$$\frac{1}{\tau_{rad}} = A_{MD} \cdot n^3 \cdot \left(\frac{I_{tot}}{I_{MD}}\right) \quad 1.11$$

where the k_r, k_{nr}, τ_{rad} and τ_{obs} is radiative rate constants, non-radiative constants, radiative lifetimes and observed lifetimes, respectively. In the case of the excitation via ligands in lanthanide complexes, the corresponding quantum yield is defined overall quantum yield Φ_{tot}. The Φ_{tot}. related to the Φ_{ff} by Equation 1. 12, [55]

$$\Phi_{tot} = \eta_{sens} \cdot \Phi_{ff} \quad 1.12$$

where the η_{sens} is overall sensitization efficiency. The η_{sens} indicate the transfer efficiency from antenna ligand to lanthanide ions in lanthanide complexes. Generally, the value of Φ_{ff} is larger than that of Φ_{tot}.

1.5 Objective

As described above, the ligand structure in lanthanide complexes and coordination polymers are influenced on photophysical properties of lanthanide ions. Therefore, the ligands design is very important for the creation of the lanthanide coordination polymers. In this thesis, the author focuses on introducing of metal complexes as bridging ligands in lanthanide coordination polymers, and reveal that the photophysical propaties of lanthanide ions were effected by introducing metal complex ligands.

Introducing of metal complexes as bridging ligands in lanthanide coordination polymers has advantages from in terms of structural and photophysical properties. One is that metal complexes are formed various steric structures depending on metal-center ions. Therefore, not only linear-type coordination polymers but also three-dimensional coordination polymers that maintain the molecular design of strong emission of lanthanide complexes could be expected to formation. The other is that metal complexes are exhibited various electronic structure and photophysical properties depending on combination of metal-center ions and organic ligands. Therefore, it is expected that the combination of metal complexes and lanthanide complexes lead to novel photo-functional properties.

1.6 Contents of this thesis

This thesis consists of five chapters.

In **Chapter 1**, various type of luminescent materials were introduced while including advanced research cases. The properties and evaluation methods of general luminescent materials were also described in detail. The basic properties of general metal and lanthanide complexes were summarized. The basic area of this doctoral thesis is described in Chapter 1. In **Chapter 2**, Eu^{3+} coordination polymer composed of luminescent Eu^{3+} and Zn^{2+} complexes was synthesized and evaluated photophysical properties. The novel structural design of Eu^{3+} coordination polymers linked with metal complexes is reported for first time. In **Chapter 3**, various $Tb(hfa)_3$ complexes / coordination polymers were synthesized and the effect on the thermo-sensitivity of the $Tb(hfa)_3$ complexs with introducing phosphine oxide ligands was investigated. It was revealed that the complex structure affected to change of temperature sensitive region. In **Chapter 4**, the photophysical properties of Eu^{3+} coordination polymer introduced palladium (heavy metal) and aluminium (light metal) complexes as bridging ligands are investigated. Electronic and structural properties of metal complex linker ligand were affected to the photophysical properties of lanthanide ions.

Finally, in **chapter 5**, summary and outlook of these studies are described.

1.7 References

[1] K. Van den Eeckhout, P. F. Smet, D. Poelman, *Materials,* **2010**, *3*, 2536-2566.

[2] T. Matsuzawa, Y. Aoki, N. Takeuch, Y. Murayama, *J. Electrochem. Soc.,* **1996**, *148*, 2670-2672.

[3] S. Ye, F. Xiao, Y. X. Pan, Y. Y. Ma, Q. Y. Zhang, *Mater. Sci. Eng. R. Rep.,* **2010**, *71*, 1-34.

[4] R. Xie, N. Hirosaki, Y. Yamamoto, T. Suehiro, M. Mitomo, K. Sakuma, *J. Ceram. Soc. Japan,* **2005**, *113*, 462-265.

[5] R. Xie, N. Hirosaki, K. Sakuma, Y. Yamamoto, M. Mitomo, *Appl. Phys. Lett.,* **2004**, *84*, 5404-5406.

[6] C. Würth, M. Grabolle, J. Pauli, M. Spieles, U. Resch-Genger, *Nat. Protoc.,* **2013**, *8*, 1535-1550.

[7] Z. Fu, X. Han, Y. Shao, J. Fang, Z. Zhang, Y. Wang, Y. Peng, *Anal. Chem.,* **2017**, *89*, 1937-1944.

[8] Z. Wang, Y. Cui, Y. Dan-oh, C. Kasada, A. Shinpo, K. Hara, *J. Phys. Chem. C,* **2007**, *111*, 7224-7230.

[9] Y. Hu, Z. Xu, S. Zhang, X. Wu, J. Ding, Z. Lv, L. Feng, *Eur. J. Med. Chem.,* **2017**, *136*, 122-130.

[10] M. Beija, C. A. M. Afonso, J. M. G. Martinho, *Chem. Soc. Rev.,* **2017**, *38*, 2410-2433.

[11] J. Zhao, K. Xu, W. Yang, Z. Wang, F. Zhong, *Chem. Soc. Rev.,* **2015**, *44*, 8904-8939.

[12] G. Ulrich, R. Ziessel, A. Harriman, *Angew. Chem. Int. Ed.,* **2008**, *47*, 1184-1201.

[13] N. Boens, V. Leen, W. Dehaen, *Angew. Chem. Soc. Rev.,* **2012**, *41*, 1130-1172.

[14] R. Martinez-Manez, F. Sancenon, *Chem. Rev.,* **2003**, *103*, 4419-4476.

[15] A. C. Grimsdale, K. L. Chan, R. E. Martin, p. G. Jokisz, A. B. Holmes, *Chem. Rev.,* **2009**, *109*, 897-1091.

[16] T. Lei, J. Dou, X. Cao, J. Wang, J. Pei, *J. Am. Chem. Soc.,* **2013**, *135*, 12168-12171.

[17] Y. Cheng, S. Yang, C. Hsu, *Chem. Rev.,* **2009**, *109*, 5868-5923.

[18] F. Huang, H. Wu, Y. Cao, *Chem. Soc. Rev.,* **2010**, *39*, 2500-2521.

[19] J. Bu, K. Watanabe, H. Hayasaka, K. Akagi, *Nat. Commun.,* **2014**, *5*, 3799-3806.

[20] M. Kasha, *Faraday Discuss.,* **1950**, *9*, 14-19.

[21] J. R. Lakowicz, *Principles of Fluoroescence spectroscopy Therd Edition,* **2006**.

[22] K. Suzuki, A. Kobayashi, S. Kaneko, K. Takehira, T. Yoshihara, H. Ishida, Y. Shiina, S. Oishi, S. Tobita, *Phys. Chem. Chem. Phys.,* **2009**, *11*, 9850-9860.

[23] V. Balzani, A. Juris, M. Venturi, *Chem. Rev.,* **1996**, *96*, 759-833.

[24] S. Lamansky, P. Djurovich, D. Murphy, F. Abdel-Razzaq, R. Kwong, I. Tsyba, M. Bortz, B. Mui, R. Bau, M. E. Thompson, *Inorg. Chem.,* **2001**, *40*, 1704-1711.

[25] S. Lamansky, P. Djurovich, D. Murphy, F. Abdel-Razzaq, H. Lee, C. Adachi, P. E. Burrows, S. R. Forrest, M. E. Thompson, *J. Am. Chem. Soc.,* **2001**, *123*, 4304-4312.

[26] T. Sajoto, P. I. Djurovich, A. B. Tamoya, J. Oxgaard, W. A. Goddard, M. E. Thompson, *J. Am. Chem. Soc.,* **2009**, *131*, 9813-9822.

[27] R. D. Costa, E. Orti, H. J. Bolink, F. Monti, G. Accorsi, N. Armaroli, *Angew. Chem. Int. Ed.,* **2012**, *51*, 8178-8211.

[28] V. Fernandez-Moreira, F. L. Thorp-Greenwood, M. P. Coogan, *Chem. Commun.,* **2010**, *46*, 186-202.

[29] R. M. Hartsborn, J. K. Barton, *J. Am. Chem. Soc.,* **1992**, *114*, 5919-5925.

[30] J. Ni, Y. Wang, H. Wang, L. Xu, Y. Zhao, Y. Pan, J. Zhang, *Dalton Trans.,* **2014**, *43*, 352-360.

[31] J. A. Gareth Williams, S. Develay, D. L. Rochester, L. Murphy, *Coord. Chem. Rev.,* **2008**, *252*, 2596-2611.

[32] A. Mills, A. Lepre, *Anal. Chem.,* **1997**, *69*, 4653-4659.

[33] V. W. Yam, V. K. Au, S. Y. Leung, *Chem. Rev.,* **2015**, *115*, 7589-7728.

[34] A. Barbieri, G. Accoris, N. Armaroli, *Chem. Commun.,* **2008**, 2185-2193.

[35] G. A. Filonenko, R. R. Fayzullin, J. R. Khusnutdinova, *J. Mater. Chem. C.,* **2017**, *5*, 1638-1645.

[36] M. Hashimoto, S. Igawa, M. Yashima, I. Kawata, M. Hoshino, M. Osawa, *J. Am. Chem. Soc.,* **2011**, *133*, 10348-10351.

[37] R. Czerwieniec, J. Yu, H. Yersin, *Inorg. Chem.,* **2011**, *50*, 8293-8301.

[38] T. Seki, K. Sakurada, H. Ito, *Angew. Chem. Int. Ed.,* **2013**, *52*, 12828-12832.

[39] M. Vitale, P. C. Ford, *Coord. Chem. Rev.,* **2001**, *219*, 3-16.

[40] N. Goswami, Q. Yao, Z. Luo, J. Li, T. Chen, J. Xie, *J. Phys. Chem. Lett.,* **2016**, *7*, 962-975.

[41] Y. Hirai, T. Nakanishi, Y. Kitagawa, K. Fshimi, T. Seki, H. Ito, Y. Hasegawa, *Angew. Chem. Int. Ed.,* **2016**, *55*, 12059-12062.

[42] K. Biradha, A. Ramanan, J. J. Vittal, *Cryst. Growth Des.,* **2009**, *9*, 2969-2970.

[43] H. A. Habib, A. Hoffmann, H. A. Höppe, G. Steinfeld, C. Janiak, *Inorg. Chem.,* **2009**, *48*, 2166-2180.

[44] R. Huang, Y. Wei, X. Dong, X. Wu, C. Du, S. Zang, T. C. W. Mak, *Nat. Chem.,* **2017**, *9*, 689-697.

[45] Z. Hu, B. J. Deibert, J. Li, *Chem. Soc. Rev.,* **2014**, *43*, 5815-5840.

[46] P.R. Matthes, C. J. Höller, M. Mai, J. Heck, S. J. Sedlmaier, S. Schmiechen, C. Feldmann, W. Schnick, K. Müller-Buschbaum, *J. Mater. Chem.,* **2012**, *22*, 10179-10187.

[47] L. V. Meyer, F. Schönfeld, K. Müller-Buschbaum, *Chem. Commun.,* **2014**, *50*, 8093-8108.

[48] S. R. Batten, N. R. Champness, X. Chen, J. Garcia-Martinez, S. Kitagawa, L. Öhrström, M. O'Keeffe, M. P. Suh, J. Reedijk, *Pure. Appl. Chem.,* **2013**, *85*, 1715-1724.

[49] B. Li, M. Chrzanowski, Y. Zhang, S. Ma, *Coord. Chem. Rev.,* **2016**, *307*, 106-129.

[50] P. Silva, S. M. F. Vilela, J. P. C. Teme, F. A. Almeida Paz, *Chem. Soc. Rev.,* **2015**, *44*, 6774-6803.

[51] E. Fresta, R. D. Costa, *J. Mater. Chem. C.,* **2017**, *5*, 5643-5675.

[52] C. Bizzarri, E. Spuling, D. M. Knoll, D. Volz, S. Bräse, *Coord. Chem. Rev.,* **2018**, *373*, 49-82.

[53] C. Huang, *Rare Earth Coordination Chemistry: Fundamentals And Applications,* John Wiley & Son (Asia) Pte. Ltd., **2010**.

[54] "1787~1987, Two hundred years of rare earths, IS-RIC 10" ed. by K. A. Gschneidner, Jr., J. Capellen, Rare-earth Information Center, Ames, Iowa. USA, **1987**.

[55] J. -C. G. Bünzli, *Chem. Rev.,* **2010**, *110*, 2729-2755.

[56] B. R. Judd, *Phys. Rev.,* **1962**, *127*, 750-761.

[57] G. S. Ofelt, *J. Chem. Phys.,* **1962**, *37*, 511-520.

[58] M. P. Hehlen, M. G. Brik. K. W. Krämer, *J. Lumin.,* **2013**, *136*, 221-239.

[59] K. Miyata, Y. Hasegawa, Y. Kuramochi, T. Nakagawa, T. Yokoo, T. Kawai, *Eur. J. Inorg. Chem.,* **2009**, *32*, 4777-4785.

[60] K. Miyata, T. Nakagawa, R. Kawakami, Y. Kita, K. Sugimoto, T. Nakashima, T. Harada, T. Kawai, Y. Hasegawa, *Chem. Eur. J.,* **2011**, *17*, 521-528.

[61] Y. Haas, G. Stein, E. Wurzberg, *J. Chem. Phys.,* **1974**, *60*, 258-263.

[62] Y. Hasegawa, Y. Wada, S. Yanagida, *J. Photochem. Photobiol. C.,* **2004**, *5*, 183-202.

[63] L. Prodi, M. Maestri, R. Ziessel, V. Balzani, *Inorg. Chem.* **1991**, *30*, 3798–3802

[64] M. H. V. Werts, R. T. F. Jukes, J. W. Verhoeven, *Phys. Chem. Chem. Phys.* **2002**, *4*, 1542–1548.

Chapter 2

Luminescent lanthanide coordination polymers cross-linked with Zinc complex ligands

Based on

Luminescent Eu(III) coordination polymer cross-linked with Zn(II) complexes

M. Yamamoto, T. Nakanishi, Y. Kitagawa, K. Fushimi, Y. Hasegawa, *Materials Letters*, **2016**, *167*, 183-187.

2.1 Introduction

Luminescent lanthanide complexes are expected to be useful in photonic properties with *4f-4f* transitions. The *4f-4f* transitions of lanthanide complexes lead to narrow emission bands (FWHM < 10 nm) and long emission lifetime ($\tau > 1$ μs), resulting in formation of remarkable luminescent materials such as display devices and bio-imaging applications[1,2]. The strong and characteristic luminescence of lanthanide complexes containing Eu^{3+}, Tb^{3+}, Sm^{3+}, Yb^{3+} and Pr^{3+} ions have been reported[3-5].

Recently, the lanthanide coordination polymers, which are composed of lanthanide ions and organic bridged ligands, have been reported as the new luminescent materials[6-8]. The lanthanide coordination polymers provide the characteristic chemical and physical properties such as thermostability[9], molecular-sensing[10] and strong luminescence[11], which can be synthesized using suitable selections of lanthanide ions and bridged organic ligands.

In the previous study, organic molecules were mainly used for bridge ligands of the lanthanide coordination polymer. The author has attempted to introduce the transition metal complex as bridge ligands for development of novel lanthanide coordination polymer.

In this chapter, Eu^{3+} coordination polymer cross-linked with Zn^{2+} complex (Eu-Zn) is reported for the first time (see Figure 2-1). The structures of Eu-Zn are characterized using XRD and TGA (thermogravimetric analysis). The photophysical properties are estimated using the emission spectra, the emission lifetimes, and the emission quantum yields. The preparations, structures and photophysical properties of

Eu-Zn are demonstrated as a new luminescent coordination polymer.

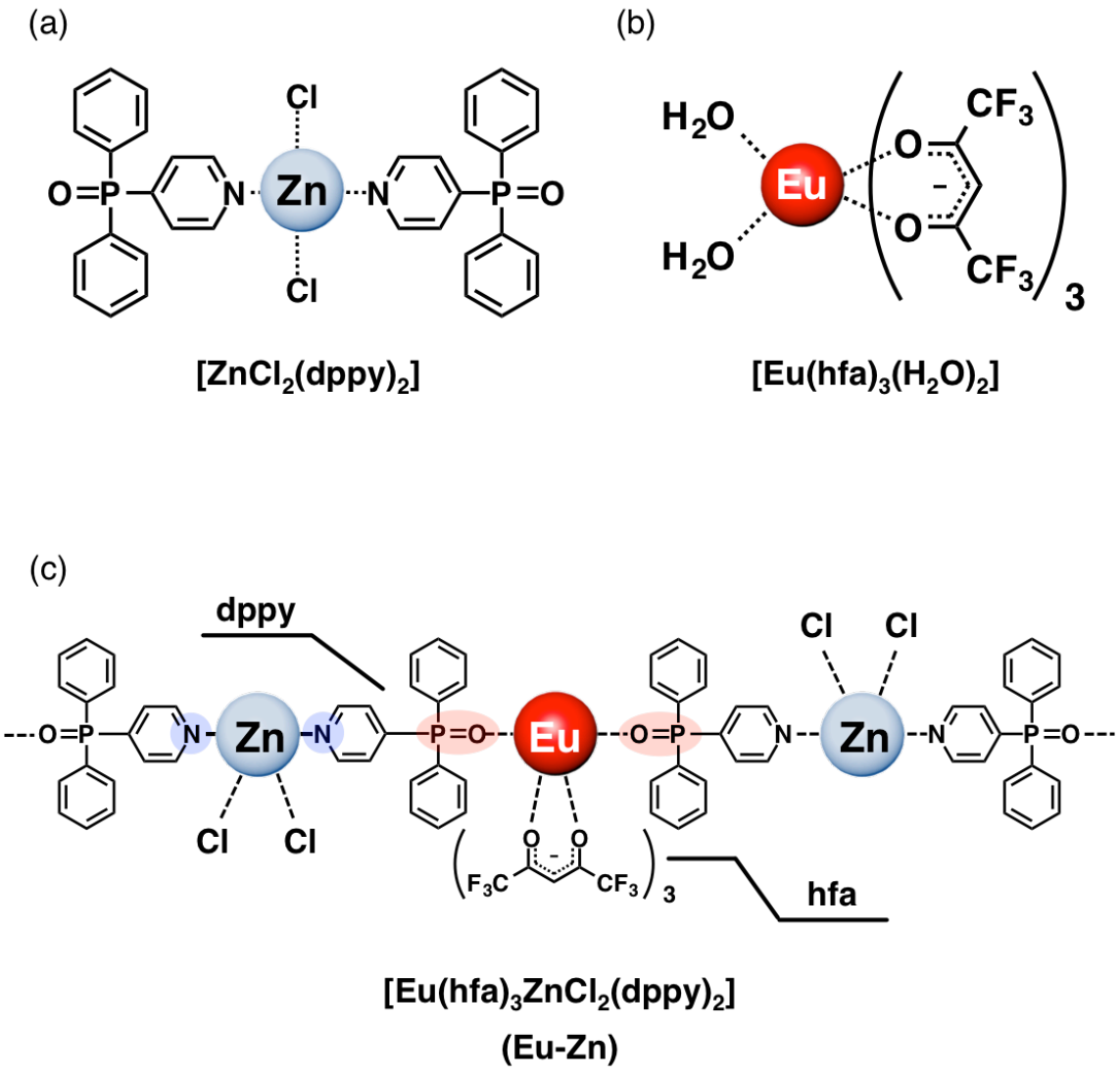

Figure 2-1. Chemical schematics of (a) $[ZnCl_2(dppy)_2]$, (b) $[Eu(hfa)_3(H_2O)_2]$, and (c) $[Eu(hfa)_3ZnCl_2(dppy)_2]_n$ (Eu-Zn).

2.2 Experimental section

Materials

4-Bromopyridine hydrochloride (>98%), tetrakis(triphenylphosphine)palladium(0) (>97%), diphenylphosphine (>90%) and hexafluoroacetylacetone (>95%) were purchased from Tokyo Chemical Industry co., ltd. Europium(III) acetate n-hydrate (>99.9%) and zinc(II) chloride (>99.9%) were obtained from Wako Pure Chemical Industries, ltd. All chemicals were reagent grade and were used without further purification.

Apparatuses

^{1}H NMR spectra were recorded on a JEOL JNM-ECS400 (400 MHz). ^{1}H NMR chemical shifts were determined by tetramethylsilane (TMS) as an internal standard. Elemental analyses were performed using a J-SCIENCE MICRO CORDER JM10. ESI-MS and FAB-MS were performed using a JEOL JMS-T100LP and a JEOL JMS-700TZ. Thermogravimetric analyses were performed using a MAC TG-DTA 2000 under an argon atmosphere at a heating rate of 1 K min^{-1}.

Preparation of 4-pyridyl diphenyl phosphine oxide (dppy) $C_{17}H_{14}NOP$

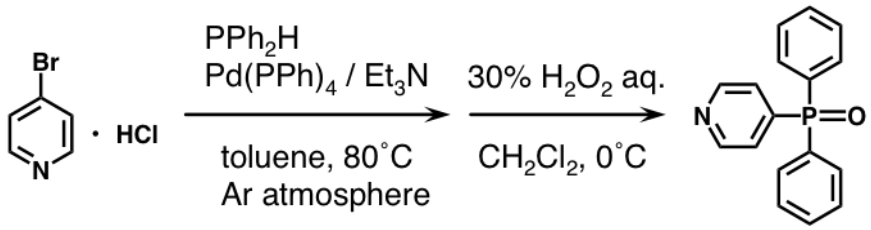

4-Bromopyridine hydrochloride (1.96 g, 10 mmol) and tetrakis (triphenylphosphine)palladium(0) (1.16 g, 10 mmol%) were added into a 40 mL of toluene under argon. Triethylamine (2.8 mL, 20 mmol) and diphenylphosphine (1.8 mL, 10 mmol) were added into the toluene solution. The reaction mixture was heated to 80°C for 18 h. After the reaction, the product was extracted with dichloromethane (30 mL × 3), and then washed with brine for three times. The dichloromethane solution was dried using anhydrous $MgSO_4$ and concentrated to dryness. The obtained brown oil added into 20 mL of dichloromethane, and cooled under 0˚C and then hydrogen peroxide aqueous solution (30%) was add to the solution. The reaction mixture was stirred for 3 h. After the reaction, the product was extracted with dichloromethane (30 mL × 3), and then washed with brine for three times. The dichloromethane solution was dried using anhydrous $MgSO_4$ and concentrated to dryness. The crude materials were separated using a silica-gel chromatography (hexane/acetone 1:4), and dppy was obtained as a white solid (1.24 g, 43%).

^{1}H NMR (400 MHz, $CDCl_3$ / TMS) : δ8.74-8.79 (t, 2H, py), 7.48-7.71 (m, 12H, Ar)ppm. ESI-MS calcd. for $[M + H]^+$: 280.09 Found, 280.09. Elemental analysis calcd. (%) for $C_{17}H_{14}NOP$: C 73.11, H 5.05, N 5.02; found: C 73.03, H 5.07, N 4.95.

Preparation of Zn^{2+} complex $[ZnCl_2(dppy)_2]$ $C_{34}H_{28}Cl_2N_2O_2P_2Zn$

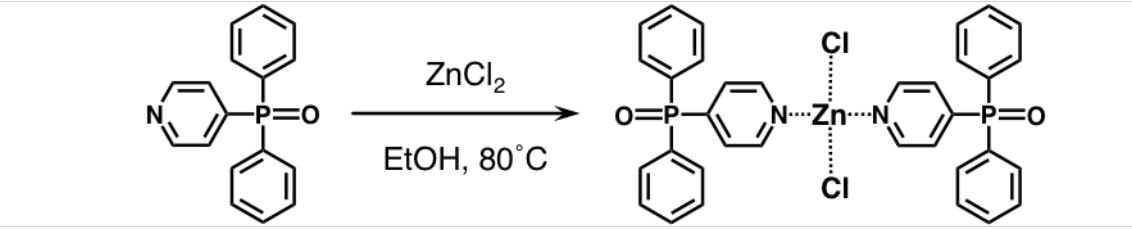

Zinc(II) chloride (0.28 g, 2.00 mmol) and 4-pyridyl diphenyl phosphine oxide (0.84 g, 3.00 mmol) were dissolved in ethanol (40 mL). The solution was heated at 80°C and refluxed while stirring for 24 h. The solvent was evaporated to afford a white powder of the titled compound. (0.42 g, 30%)

^{1}H NMR (400 MHz, $CDCl_3$ / TMS) : δ8.84-8.89 (t, 4H, py), 7.71-7.77 (d, 4H, py), 7.62-7.70 (m, 12H, Ar), 7.50-7.57 (m, 8H, Ar)ppm. ESI-MS calcd. for $[ZnCl(dppy)_2]^-$: 692.03 Found, 692.03. Elemental analysis calcd. (%) for $C_{34}H_{28}Cl_2N_2O_2P_2Zn$: C 58.77, H 4.06, N 4.03; found: C 59.27, H 4.31, N 3.73.

Preparation of $[Eu(hfa)_3(H_2O)_2]$ $C_{15}H_7F_{18}O_8Eu$:

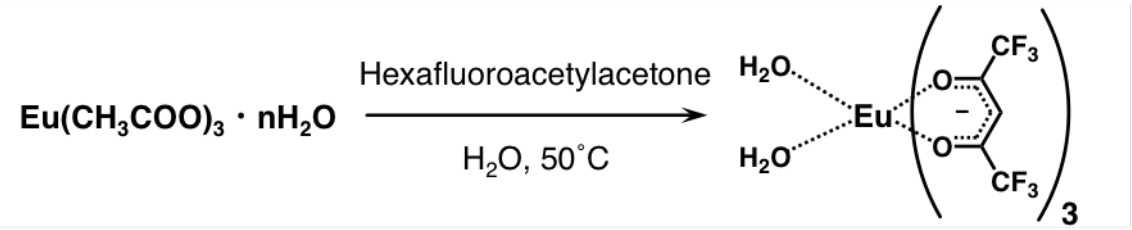

The precursor Eu^{3+} complex $[Eu(hfa)_3(H_2O)_2]$ was prepared according to the literature reference.[12]

Elemental analysis calcd. (%) for $C_{15}H_2O_8F_{18}Eu$: C, 22.48; H, 0.88, Found: C, 22.12; H, 1.01.

Preparation of mononuclear Eu^{2+} complex $[Eu(hfa)_3(dppy)_2]$ $C_{49}H_{31}F_{18}N_2O_8P_2Eu$

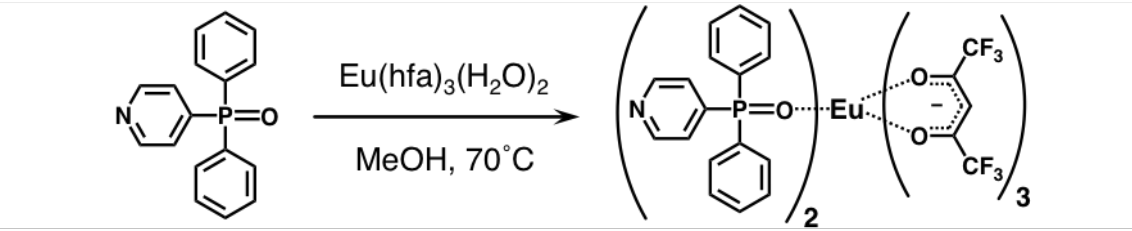

Methanol (50mL) containing $[Eu(hfa)_3(H_2O)_2]$ (294 mg, 0.36 mmol) and dppy (200 mg, 0.72 mmol) was fluxed under stirring for 3 h. The reaction mixture was concentrated with evaporator. The precipitate was filtered, washed with methanol for several times, and dried in vacuum. Yield: 150 mg (31%).

IR (ART): 1653 (st, C=O), 1250,1140 (st, C-F), 1161, 1122 (st, P=O) cm^{-1}. ESI-MS calcd. for $[Eu(hfa)_2(dppy)_2]^-$: 1125.06 Found, 1125.06. Elemental analysis calcd. (%) for $C_{49}H_{31}F_{18}N_2O_8P_2Eu$: C 44.20, H 2.35, N, 2.10; found: C 44.08, H 2.50, N 2.07.

Preparation of Eu-Zn complex $[Eu(hfa)_3(dppy)_2ZnCl_2]_n$ $C_{49}H_{31}Cl_2EuF_{18}N_2O_8P_2Zn$

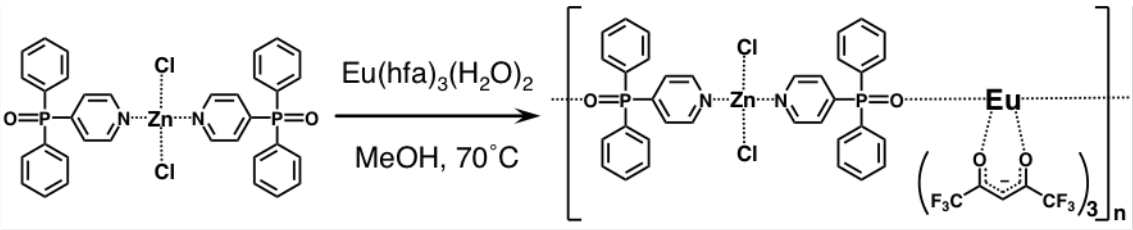

Zn^{2+} complex $[ZnCl_2(dppy)_2]$ (1 equiv.) and $[Eu(hfa)_3(H_2O)_2]$ (1 equiv.) were dissolved in methanol. The solution was refluxed while stirring for 5 h, and the reaction mixture was concentrated to dryness.

FAB-MS calcd. for $[Eu(hfa)_3(dppy)ZnCl_2]^+$: 1258.93 Found, 1259.9. Elemental analysis calcd (%) for $C_{49}H_{31}Cl_2EuF_{18}N_2O_2P_2Zn+2H_2O$: C 39.13, H 2.35, N 1.86; found: C 38.73, H 2.25, N 1.88.

Optical measurements

Emission spectra were measured with a HORIBA Fluorolog-3 spectrofluorometer and corrected for the response of the detector system. Emission lifetimes (τ_{obs}) were measured using the third harmonics (355 nm) of a Q-switched Nd:YAG laser (Spectra Physics, INDI-50, fwhm = 5 ns, λ = 1064 nm) and a photomultiplier (Hamamatsu Photonics, R5108, response time ≤ 1.1 ns). The Nd:YAG laser response was monitored with a digital oscilloscope (Sony Tektronix, TDS3052, 500 MHz) synchronized to the single-pulse excitation. Emission lifetimes were determined from the slope of logarithmic plots of the decay profiles.

2.3 Results and discussion

2.3.1 Structural analyses

Novel ligand 4-pyridyldiphenylphosphane oxide (dppy) contains selective coordinate sites P=O and N atoms for europium ions and zinc ions, respectively. The dppy was synthesized by the coupling reaction of 4-bromopyridine hydrochloride with diphenylphosphane and Pd(0) complex as a catalyst, and then oxidized using hydrogen peroxides. Zn^{2+} complex $[ZnCl_2(dppy)_2]$ was prepared by the complexation of zinc(II) chloride with dppy in ethanol under reflux condition. Finally, Eu^{3+} coordination polymer $[Eu(hfa)_3(dppy)_2ZnCl_2]_n$ (Eu-Zn) was prepared by the complexation of $[Eu(hfa)_3(H_2O)_2]$ with $[ZnCl_2(dppy)_2]$ for 5 h. These chemical structures were confirmed by MS (ESI- and FAB-MS) and elemental analyses. The X-ray diffraction patterns of Eu-Zn coordination polymer are shown in Figure 2-2a. The X-ray diffraction pattern of Eu-Zn is similar to amorphous glass without crystalline structure.

The TG-DTA of $[ZnCl_2(dppy)_2]$ and Eu-Zn were carried out for estimation of their thermal stabilities under an nitrogen atmosphere in the temperature range of 50–350˚C. TG-DTA data are shown in Figure 2-2b and 2c. Weight loss of Eu-Zn at 350˚C is approximately 50%, which are corresponded to eliminations of three hfa ligands per one unit of Eu^{3+} coordination polymers. The weight loss temperatures of Eu-Zn are observed at 150 and 250˚C. Phase transition temperature of Zn^{2+} complex was found to be 150˚C (see Figure 2-2c). This result suggested that Zn^{2+} complexes of Eu-Zn coordination polymer are transformed at around 150˚C. At around 150˚C, Eu-Zn might release any adsorbed water or methanol related to transportation of $[ZnCl_2(dppy)_2]$.

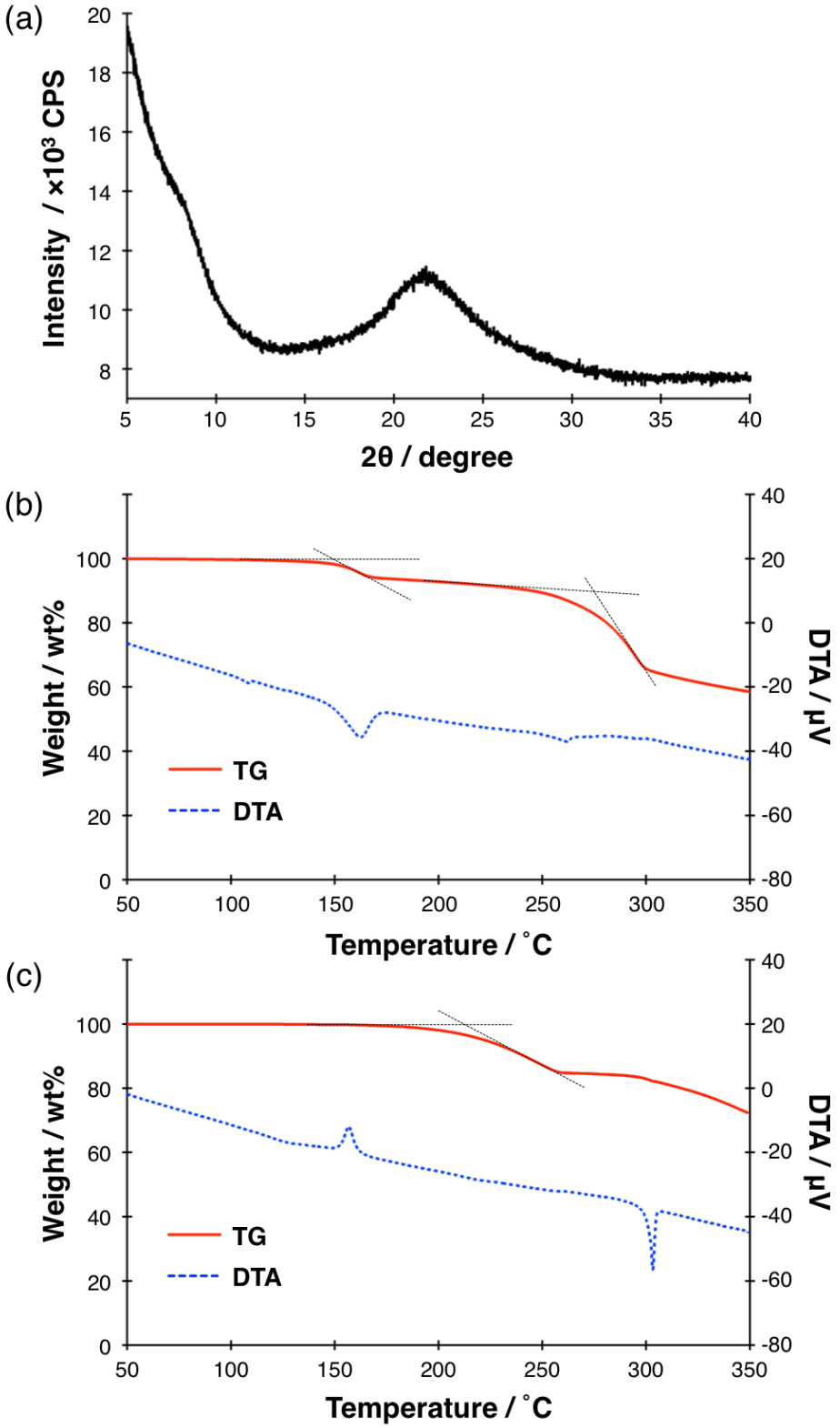

Figure 2-2. (a) The X-ray diffraction pattern of $[Eu(hfa)_3(dppy)_2ZnCl_2]_n$. TGA profiles for (b) $[Eu(hfa)_3(dppy)_2ZnCl_2]_n$ coordination polymer and (c) $[ZnCl_2(dppy)_2]$ joint ligand.

2.3.2 Photophysical properties

The emission spectra for $[Eu(hfa)_3(dppy)_2ZnCl_2]_n$ (Eu-Zn) , $[Eu(hfa)_3(dppy)_2]$ and precursor $[Eu(hfa)_3(H_2O)_2]$ in the solid state were shown in Figure 2-3a. The emission bands are observed at around 578, 592, 613, 650, and 698 nm, and are attributed to the 4*f*– 4*f* transitions of Eu^{3+} ($^5D_0 \rightarrow {}^7F_J$: J = 0, 1, 2, 3, and 4), respectively. The spectra were normalized with respect to the magnetic dipole transition intensities (MD) at around 592 nm ($^5D_0$–$^7F_1$), which are insensitive to the surrounding environment of the Eu^{3+} ions. The emission bands around 613 nm are due to the electric dipole transitions (ED), which are strongly dependent on the coordination geometry [13]. The spectral shapes of emission band at around 613 nm of Eu-Zn and $[Eu(hfa)_3(dppy)_2]$ are different from that of $[Eu(hfa)_3(H_2O)_2]$. The $^5D_0 \rightarrow {}^7F_2$ transition area of Eu-Zn and $[Eu(hfa)_3(dppy)_2]$ are larger than those of $[Eu(hfa)_3(H_2O)_2]$. The large ED is directly linked to the asymmetric geometric structure of Eu^{3+} ion and enhanced radiative rate constant (k_r).

The emission lifetimes observed from the $^5D_0$ excited level (τ_{obs}) were determined from the slope of the logarithmic decay profile (Figures 2-3b). The time-resolved emission profiles of En-Zn, $[Eu(hfa)_3(dppy)_2]$ and $[Eu(hfa)_3(H_2O)_2]$ show single-exponential decays with millisecond scale lifetimes. The emission lifetimes for En-Zn, $[Eu(hfa)_3(dppy)_2]$ and $[Eu(hfa)_3(H_2O)_2]$ were determined to be 850, 900 and 550 μs, respectively.

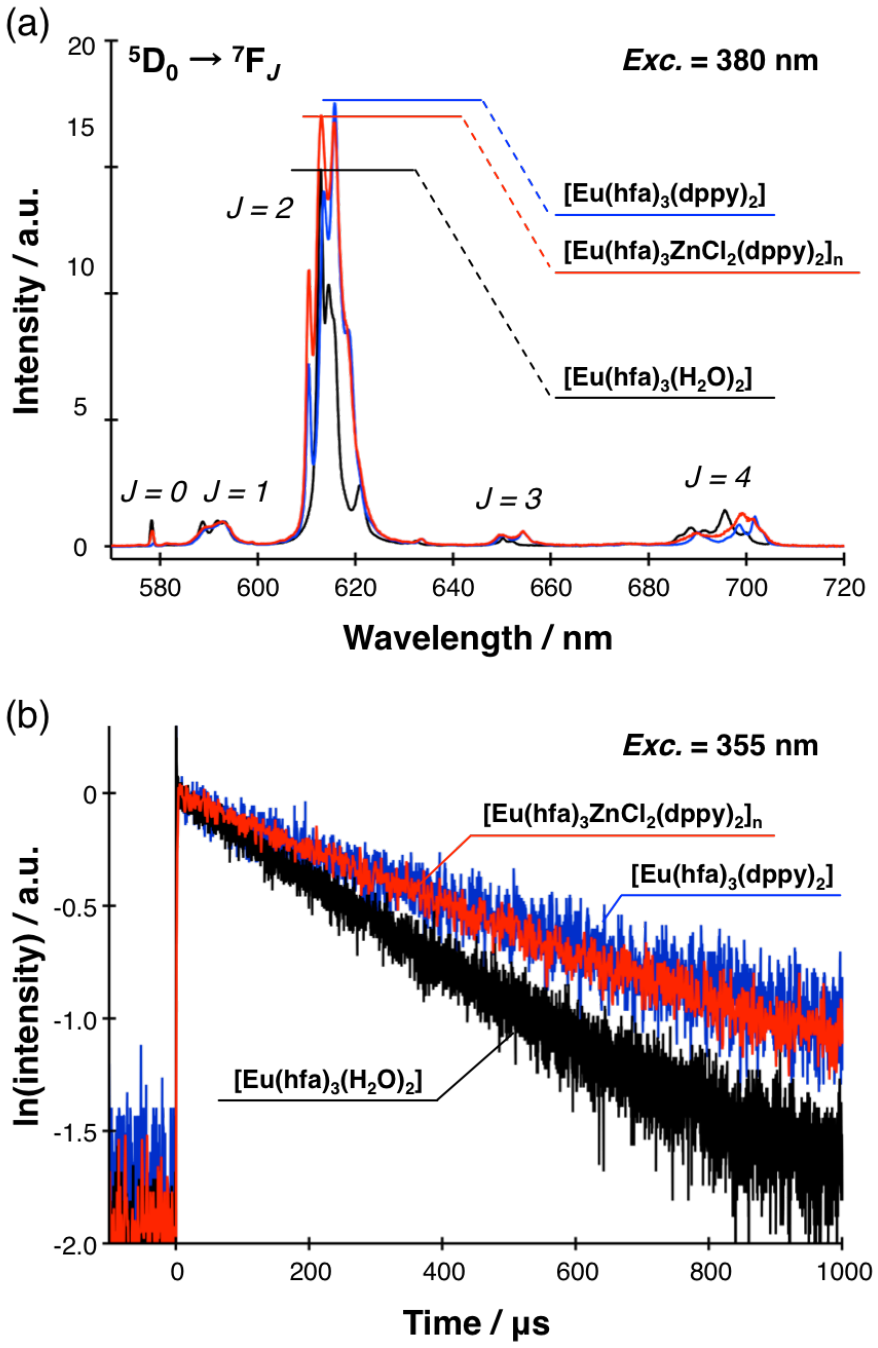

Figure 2-3. (a) Emission spectra of Eu-Zn coordination polymer (red line), $[Eu(hfa)_3(dppy)_2]$ (blue line) and $[Eu(hfa)_3(H_2O)_2]$ (black line) in solid state. (b) Emission decay profiles of Eu-Zn coordination polymer (red line), $[Eu(hfa)_3(dppy)_2]$ (blue line) and $[Eu(hfa)_3(H_2O)_2]$ (black line) in solid state.

Their τ_{obs}, k_r, k_{nr}, and Φ_{Ln} values are summarized in Table 1. The emission quantum yields were calculated using τ_{rad} constant based on the emission spectra. The emission quantum yields of Eu-Zn, $[Eu(hfa)_3(dppy)_2]$ and $[Eu(hfa)_3(H_2O)_2]$ in the solid state were estimated to be 59 73, and 31%, respectively. The Eu-Zn showed a large emission quantum yield (Φ_{Ln} = 59%), which was based on the large k_r and small k_{nr}. The large k_r of Eu-Zn was due to enhancement of the ED transition probability based on their asymmetric coordination geometries. Furthermore, the small k_{nr} of Eu-Zn was induced by the rigid coordination network structure.

Table 2-1. Photophysical properties of Eu-Zn coordination polymers, mononuclear $[Eu(hfa)_3(dppy)_2]$ and precursor $[Eu(hfa)_3(H_2O)_2]$ in the solid state.

	Φ_{ff}[a]	Φ_{tot}[b]	η_{sens}[c]	τ_{obs}[d]	k_r[e]	k_{nr}[f]
	%	%	%	μs	s^{-1}	s^{-1}
$[Eu(hfa)_3(H_2O)_2]$	31	-	-	550	5.7×10^2	1.2×10^3
$[Eu(hfa)_3(dppy)_2]$	73	64	87	900	7.7×10^2	2.9×10^2
$[Eu(hfa)_3ZnCl_2(dppy)_2]_n$	59	28	48	850	7.0×10^2	4.8×10^2

[a] The intrinsic emission quantum yields were calculated from $\Phi_{ff} = k_r/(k_r+k_{nr}) = \tau_{obs}/\tau_{rad}$. [b] The total emission quantum yields Φ_{tot} were measured by integrating sphere (excitation at 370 nm). [c] The photo-sensitization efficiencies were calculated from $\eta_{sens} = \Phi_{tot}/\Phi_{ff}$. [d] Emission lifetime (τ_{obs}) of Eu^{3+} complexes were measured by excitation at 355 nm (Nd:YAG 3ω). [e] Radiative rate constants (k_r) for Eu^{3+} complexes estimated from $1/\tau_{rad} = A_{MD}n^3(I_{tot}/I_{MD})$ [14,15]. [f] Non-radiative rate constant $k_{nr} = 1/\tau_{obs} - 1/\tau_{rad}$.

2.4 Conclusion

The novel structural design of Eu^{3+} coordination polymers $[Eu(hfa)_3ZnCl_2(dppy)_2]_n$ (Eu-Zn), which were composed of luminescent Eu^{3+} complexes and linker Zn^{2+} complexes, were successfully synthesized. The polymeric structure of Eu-Zn promotes enhancement of luminescent properties related to large k_r and small k_{nr}. The emission quantum yield of the Eu-Zn coordination polymer was larger than that of precursor $[Eu(hfa)_3(H_2O)_2]$. Luminescent lanthanide coordination polymers cross-linked with metal complexes are expected to open up new coordination polymers in the frontier field of materials science.

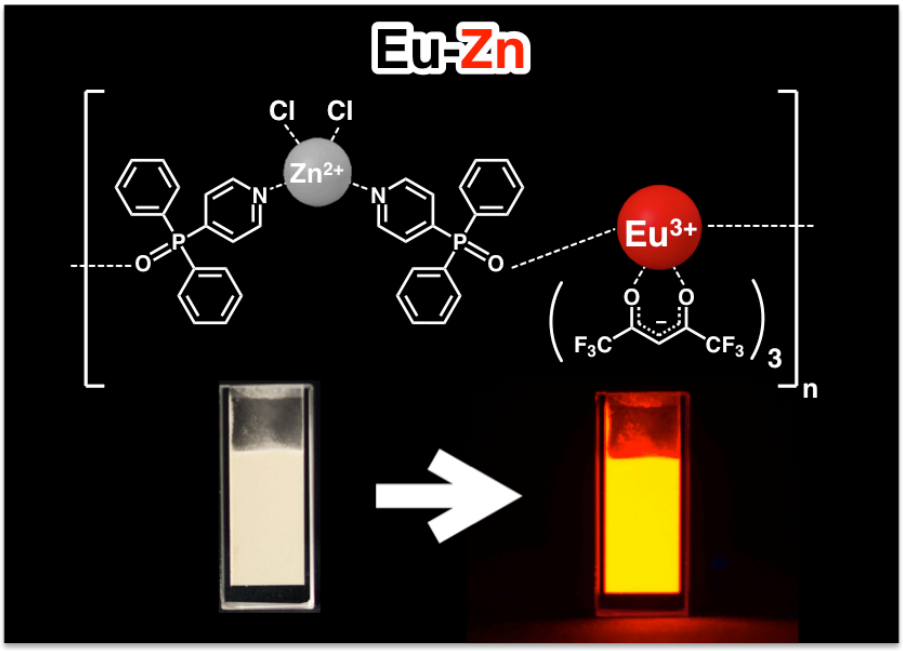

2.5 References

[1] S. J. Butler, L. Lamarque, R. Pal, D. Parker, *Chem. Sci.*, **2014**, *5*, 1750-1756.

[2] G. Shao, H. Yu, N. Zhang, Y. He, K. Feng, X. Yang, R. Cao, M. Gong, *Phys. Chem. Chem. Phys.*, **2014**, *16*, 695-702.

[3] L. J. Daumann, D. S. Tatum, B. E. R. Snyder, C. Ni, G. Law, E. I. Solomon, K. N. Reymond, *J. Am. Chem. Soc.*, **2015**, *137*, 2816-2819.

[4] N. M. Shavaleev, G. Accorsi, D. Virgili, Z. R. Bell, T. Lazarides, G. Calogero, N. Armaroli, M. D. Ward, *Inorg. Chem.*, **2005**, *44*, 61-72.

[5] A. Ishii, S. Kishi, H. Ohtsu, T. Iimori, T. Nakabayashi, N. Ohta, N. Tamai, M. Melnik, M. Hasegawa, Y. Shigesato, *ChemPhysChem*, **2007**, *8*, 1345-1351.

[6] V. Haquin, M. Etienne, C. Daiguebonne, S. Freslon, G. Calvez, K. Bernot, L. L. Pollès, S. E. Ashbrook, M. R. Mitchell. J. C. Bünzli, S. V. Eliseeva, O. Guillou, *Eur. J. Inorg. Chem.*, **2013**, *20* , 3464-3476.

[7] K. Miyata, Y. Konno, T. Nakanishi, A. Kobayashi, M. Kato, K. Fushimi, Y. Hasegawa, *Angew. Chem. Int. Ed.,* **2013**, *52*, 6413-6416.

[8] O. Kotova, R. Daly, C. M. G. Santos, M. Boese, P. E. Kruger, J. J. Boland, T. Gunnlaugsson, *Angew. Chem. Int. Ed.*, **2012**, *51*, 7208-7212.

[9] H. Zhang, L. Zhou, J. Wei, Z. Li, P. Lin, S. Du, *J. Mater. Chem.*, **2012**, *22*, 21210-21217.

[10] B. Chen, Y. Yang, F. Zapata, G. Lin, G. Qian, E. B. Lobkovsky, *Adv. Mater.*, **2017**, *19*, 1693-1696.

[11] K. Miyata, T. Ohba, A. Kobayashi, M. Kato, T. Nakanishi, K. Fushimi, Y. Hasegawa, *ChemPlusChem*, **2012**, *77*, 277-280.

[12] Y. Hasegawa, M. Yamamuro, Y. wada, N. Kanehisa, Y. Kai, S. Yanagida, *J. Phys. Chem. A*, **2003**, *107*, 1697-1702.

[13] Y. Hasegawa, Y. Wada, S. Yanagida, *J. Photochem. Photobiol. C.*, **2004**, *5*, 183-202.

[14] L. Prodi, M. Maestri, R. Ziessel, V. Balzani, *Inorg. Chem.*, **1991**, *30*, 3798–3802.

[15] M. H. V. Werts, R. T. F. Jukes, J. W. Verhoeven, *Phys. Chem. Chem. Phys.*, **2002**, *4*, 1542–1548.

Chapter 3

Ligand-assisted Back Energy Transfer in Luminescent Tb(III) Complexes for Thermo-sensing Properties

Based on

Ligand-assisted Back Energy Transfer in Luminescent Tb(III) Complexes for Thermo-sensing Properties

M. Yamamoto, Y. Kitagawa, T. Nakanishi, K. Fushimi, and Y. Hasegawa, *Chem. Eur. J.,* **2018**, in press.

3.1 Introduction

Thermosensitive paints containing luminescent materials enable temperature information about the substance surface to be obtained with high spatial resolution and a fast response.[1] Luminescent thermosensors are expected to be useful for capturing surface temperature dynamics of vehicles, aircrafts and chemical reactors.[2,3] The sensing mechanism is based on the temperature-depended luminescence intensities and lifetimes of organic compounds[4-6], metal complexes[7-9] and nanoparticles[10-12]. In particular, luminescent thermosensors containing lanthanide complexes have attracted attention for precise temperature imaging with narrow emission bands (full-width at half maximum (FWHM) < 10 nm) and long emission lifetimes (emission lifetime > 1 μs) based on the 4*f*-4*f* transitions.[13-16] In 2003, Amao and co-workers reported luminescent thermosensitive paint using the vibrational relaxation process of a red luminescent Eu^{3+} complex.[14] In 2004, Hasegawa described the temperature-sensing ability of a green luminescent Tb^{3+} complex based on the back energy transfer (BEnT).[16] The energy transfer process from Tb^{3+} to Eu^{3+} in lanthanide coordination polymer has also been used for a ratiometric luminescent thermosensor.[17] The thermosensitive paints containing luminescent lanthanide complexes have also been widely investigated. [18-22] Luminescent Tb^{3+} complexes with BEnT are the most useful in molecular design unit for high-speed thermosensor. Here, Hasegawa focus on the BEnT from excited state of Tb^{3+} ($^5D_4$) to excited triplet state of the aromatic ligand (T_1) for thermosensing. The small energy gap between the $^5D_4$ and T_1 states (<1850 cm^{-1}) leads to effective BEnT in Tb^{3+} complexes.[23] To control of the energy gap, pyridyl, diketonate and carbonyl ligands

with aromatic derivatives in Tb^{3+} complexes have been investigated.[24-28] Among these ligands, the hexafluoroacetylacetonate (hfa) ligand is one of the most promising candidates for development of thermosensitive luminescent Tb^{3+} complexes (energy gap of hfa = 1700 cm^{-1}). [24,25] The hfa ligand also forms hydrogen bond networks in solid Tb^{3+} complexes, which promotes the thermal stability in the high-temperature range.[29,30] The luminescent units composed of $Tb(hfa)_3$ complexes are suitable for thermosensitive paints based on the BEnT.

In general, the BEnT is depended on the activation energy (ΔE_a) and frequency factor (A) in the Arrhenius analysis.[27, 31] Controlling ΔE_a and A in $Tb(hfa)_3$ complexes improves the thermosensing ability for adjustable sensing range and temperature. In this chapter, activation energy control in BEnT of $Tb(hfa)_3$ complex is reported using activation energy controllers (AECs). The conceptual image of AECs is shown in Figure 3-1a. Here, the author selects the aromatic phosphine oxide ligand as an AEC molecule. The ΔE_a and A values of BEnT can be tuned by introducing the phosphine oxide ligand with a specific interaction with hfa ligand. The phosphine oxide ligand strongly coordinates to the lanthanide ion by P=O group.[32] The P=O group is also useful for enhancing the luminescence of lanthanide complexes based on suppression of nonradiative process via vibrational relaxation.[32] Luminescent Tb^{3+} complexes with hfa and phosphine oxide ligands, mononuclear $[Tb(hfa)_3(AEC)]$ and polynuclear $[Tb(hfa)_3(AEC)]_n$: $[Tb(hfa)_3(tppo)_2]$, $[Tb(hfa)_3(biphepo)]$, $[Tb(hfa)_3(dppy)_2]$, $[Tb(hfa)_3(dpb)]_n$, $[Tb(hfa)_3(dpbp)]_n$ and $[Tb(hfa)_3ZnCl_2(dppy)_2]_n$ (tppo: trisphenylphosphine oxide, biphepo: [1,1'-biphenyl]-2,2'-diylbis(diphenylphosphine

oxide), dppy: 4-pyridyldiphenylphosphine oxide, dpb: 1,4-phenylenebis(diphenylphosphine oxide), dpbp: [1,1'-biphenyl]-4,4'-diylbis(diphenylphosphine oxide)), were prepared for estimation of tunable ΔE_a and A values in their BEnT (Figure 3-1b). The emission properties of $[Tb(hfa)_3(AEC)]$ were evaluated using the emission spectra, emission lifetimes and emission quantum yields. To estimate the ΔE_a and A values in BEnT, Arrhenius analysis was performed using temperature-dependent emission lifetimes measurements. The triplet state lifetimes of hfa ligands were estimated using polynuclear and mononuclear Gd^{3+} complexes. Introduction of phosphine oxide ligands to $Tb(hfa)_3$ complexes leads to control of the BEnT process, which is called ligand-assisted BEnT. This is the first report of control of thermosensing properties of the $Tb(hfa)_3$ complex by ligand-assisted BEnT.

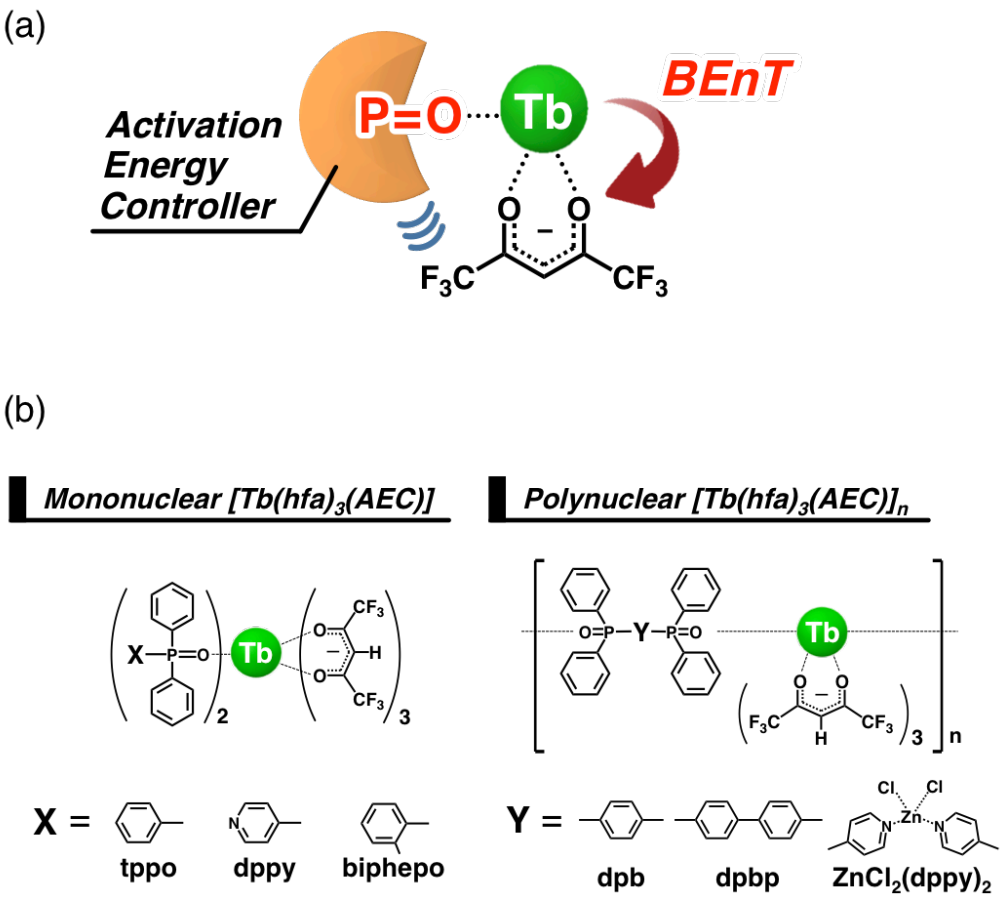

Figure 3-1. (a) Conceptual images of this chapter. (b) Chemical structure of $Tb(hfa)_3$(phosphine oxide) complexes.

3.2 Experimental section

Materials:

Terbium acetate tetrahydrate (>99.9%), *n*-BuLi (in *n*-hexane, 1.6 M) and hydrogen peroxide were purchased from Kanto Chemical Co., Inc. Hexafluoroacetylacetone (>95.0%), triphenylphosphine oxide (>98.0%), 2,2'-bis(diphenylphosphino)biphenyl (>98.0%), 1,4-dibromobenzene (>99.0%), 4,4'-dibromobiphenyl (>98.0%) and chlorodiphenylphosphine (>97.0%) were obtained from Tokyo Chemical Industry Co., Ltd. All chemicals and solvents were reagent grade and were used without further purification.

Apparatuses

^{1}H NMR spectra were recorded using a JEOL JNM-ECS400 (400 MHz). ^{1}H NMR chemical shifts were determined by tetramethylsilane (TMS) as an internal standard. Infrared spectra were recorded using a JASCO FT/IR-4600. Elemental analyses were performed using an Exeter Analytical, Inc. CE-440 Elemental Analyzer.

Preparation of [1,1'-biphenyl]-2,2'-diylbis(diphenylphosphine oxide) (biphepo) $C_{36}H_{28}O_2P_2$:

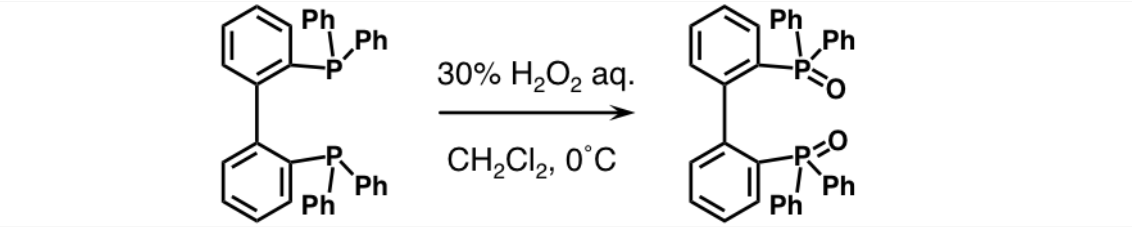

Biphepo was obtained by the same method as previously reported by Nakamura et al.[33] 2,2'-Bis(diphenylphosphino)biphenyl (500 mg, 1.60 mmol) added into 20 mL of dichloromethane, and cooled under 0˚C and then 30% H_2O_2 aqueous solution (30%) was add to the solution. The reaction mixture was stirred for 3 h. After the reaction, the product was extracted with dichloromethane (30 mL × 3), and then washed with brine for three times. The dichloromethane solution was dried using anhydrous $MgSO_4$ and concentrated to dryness. The biphepo was recovered as a white solid. Yield: 336 mg (38%).

^{1}H NMR (400 MHz, $CDCl_3$ / TMS): δ7.73-7.69(t, 4H), 7.66-7.63(t, 4H), 7.53-7.50(t, 2H), 7.47-7.43(t, 4H), 7.36-7.33(t, 2H), 7.31-7.28(t, 4H), 7.20-7.15(m, 6H), 7.00(t, 2H)ppm. IR (ART): 1210 (st, P=O) cm^{-1}.

Preparation of 4-pyridyl diphenyl phosphine oxide (dppy) $C_{17}H_{14}NOP$:

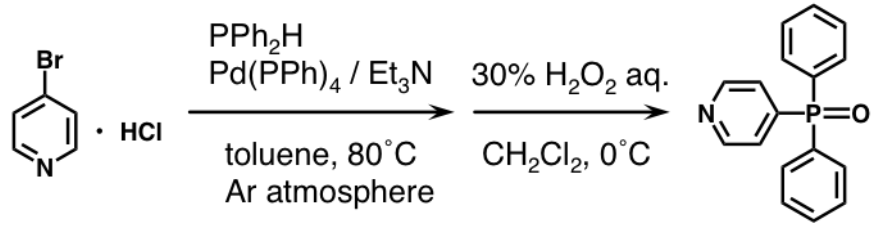

The dppy ligand was prepared according to chapter 2.2.[34]

^{1}H NMR (400MHz, $CDCl_3$/TMS): δ8.74-8.79 (t, 2H, py), 7.48-7.71 (m, 12H, Ar) ppm. ESI-MS calcd. for $[M+H]^+$: 280.09 Found, 280.09. Elemental analysis calcd (%) for $C_{17}H_{14}NOP$: C 73.11, H 5.05, N 5.02; found: C 73.03, H, 5.07; N, 4.95.

Preparation of 1,4-phenylenebis(diphenylphosphine oxide) (dpb) $C_{30}H_{24}O_2P_2$:

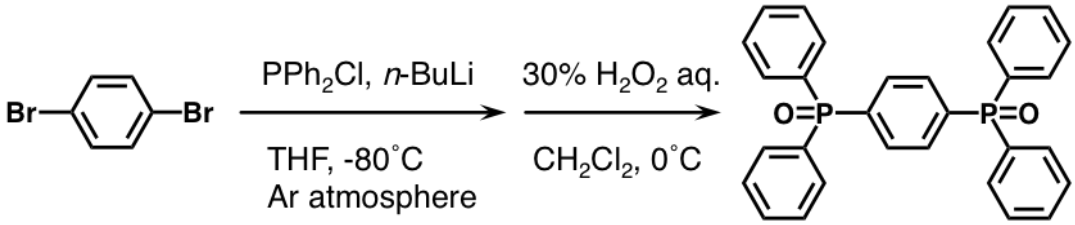

1,4-phenylenebis(diphenylphosphine oxide) was synthesized according to the published procedure.[35] A solution of *n*-BuLi (12.5 mL, 1.6 M, 20 mmol), was added dropwise to a solution of 1,4-dibromobenzene (2.36 g, 10 mmol) in dry THF (30 mL) at –80˚C. The addition was completed in ca. 15 min during which time a yellow precipitate was formed. The mixture was allowed to stir for 3 h at –10˚C, after which a chlorodiphenylphosphine (2.7 mL, 20 mmol) was added dropwise at –80˚C. The mixture was gradually brought to room temperature, and stirred for 14 h. The product was extracted with dichloromethane, the extracts washed with brine for three times and dried over anhydrous $MgSO_4$. The obtained white solid and dichloromethane (ca. 40 mL) were placed in a flask. The solution was cooled to 0˚C and then 30% H_2O_2 aqueous solution (5 mL) was added to it. The reaction mixture was stirred for 2 h. The product was extracted with dichloromethane, the extracts washed with brine for three times and dried over anhydrous $MgSO_4$. The solvent was evaporated, and resulting residue was washed with ethyl acetate for several times, and filtered in vacuum to afford a white

powder. Yield: 2.5 g (52%).

^{1}H NMR (400 MHz, $CDCl_3$ / TMS): δ7.48-7.78 (m, 24H, *p*-C_6H_5, C_6H_4) ppm. IR (ART): 1121 (st, P=O) cm^{-1}.

Preparation of [1,1'-biphenyl]-4,4'-diylbis(diphenylphosphine oxide) (dpbp) $C_{36}H_{28}O_2P_2$:

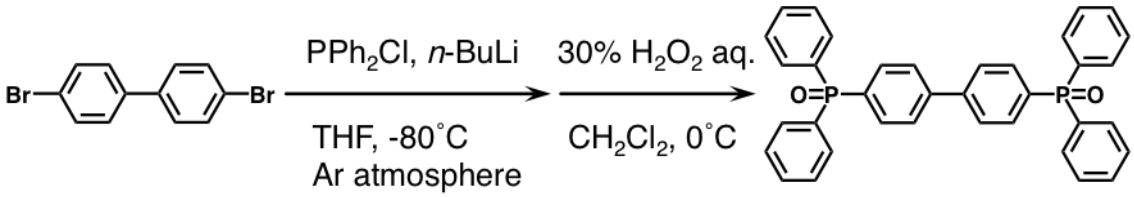

4,4'-bis(diphenylphosphoryl)biphenyl was synthesized according to the published procedure. [35] A solution of *n*-BuLi (9.3 mL, 1.6 M hexane, 15 mmol), was added dropwise to a solution of 4,4'-dibromobiphenyl (1.9 g, 6.0 mmol) in dry THF (30 mL) at –80˚C. The addition was completed in about 15 min, after that a yellow precipitate was formed. The mixture was allowed to stir for 3 h at –10˚C, after which a chlorodiphenylphosphine (2.7 mL, 15 mmol) was added dropwise at –80˚C. The mixture was gradually brought to room temperature, and stirred for 14 h. The product was extracted with dichloromethane, the extracts washed with brine for three times and dried over anhydrous $MgSO_4$. The obtained white solid and dichloromethane (ca. 40 mL) were placed in a flask. The solution was cooled to 0˚C and then 30% H_2O_2 aqueous solution (5 mL) was added to it. The reaction mixture was stirred for 2 h. The product was extracted with dichloromethane, the extracts washed with brine for three times and dried over anhydrous $MgSO_4$. The solvent was evaporated, and resulting residue was

washed with ethyl acetate for several times, and filtered in vacuum to afford a white powder. Yield: 1.1 g (33%).

^{1}H NMR (400 MHz, $CDCl_3$ / TMS): δ7.67-7.80 (m, 16H, *p*-C_6H_5, C_6H_4), 7.45-7.60 (m, 12H, *p*-C_6H_5, C_6H_4) ppm. IR (ART): 1120 (st, P=O) cm^{-1}.

Preparation of [$ZnCl_2(dppy)_2$] $C_{34}H_{28}Cl_2N_2O_2P_2Zn$:

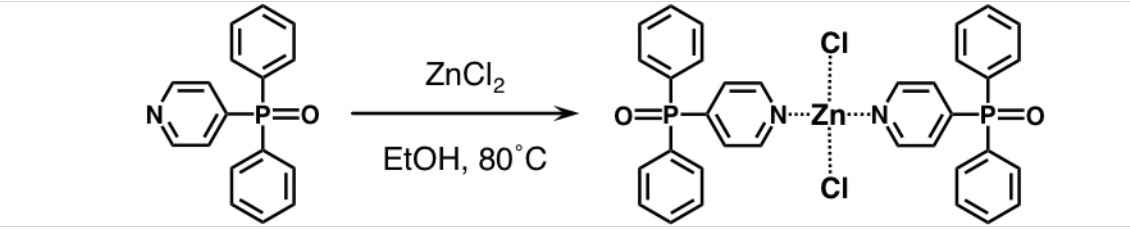

The [$ZnCl_2(dppy)_2$] was prepared according to chapter 2.2.[34]

^{1}H NMR (400MHz, $CDCl_3$/TMS): δ8.84-8.89 (t, 4H, py), 7.71-7.77 (d, 4H, py), 7.62-7.70 (m, 12H, Ar), 7.50-7.57 (m, 8H, Ar) ppm. ESI-MS calcd. for $[ZnCl(dppy)_2]^+$: 692.03 Found, 692.03. Elemental analysis calcd. (%) for $C_{34}H_{28}Cl_2N_2O_2P_2Zn$: C 58.77, H 4.06, N 4.03; found: C 59.27, H 4.31, N 3.73.

Preparation of [$Tb(hfa)_3(H_2O)_2$] $C_{15}H_7F_{18}O_8Tb$:

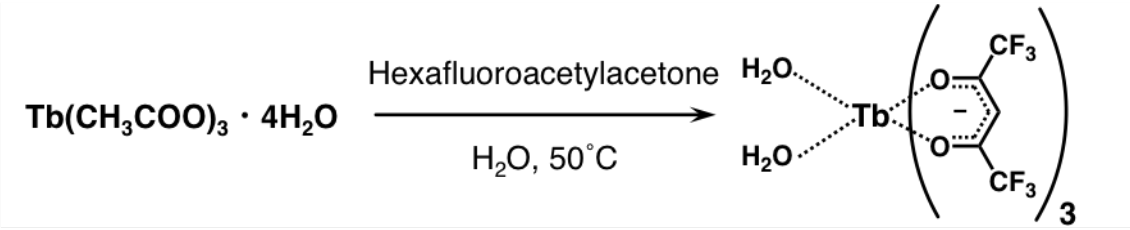

[$Tb(hfa)_3(H_2O)_2$] was prepared according to literature reference.[16] Terbium acetate tetrahydrate (2.4 g, 5.9 mmol) was dissolved in distilled water (30 mL). Hexafluoroacetylacetone (4.0 g, 19 mmol) was added dropwise to the solution and let

stirred for 3 h at room temperature to form pale yellow precipitates. The reaction mixture was filtered and washed with distilled water. The resulting powder was used without further purification for the next step. Yield 4.1 g (85%).

IR (ART): 1647 (st, C=O), 1251, 1204,1135 (st, C-F) cm^{-1}. Elemental analysis calcd. (%) for $C_{34}H_{28}Cl_2N_2O_2P_2Zn$: C 58.77, H 4.06, N 4.03; found: C 59.27, H 4.31, N 3.73.

Preparation of $[Tb(hfa)_3(tppo)_2]$ $C_{51}H_{33}F_{18}O_8P_2Tb$:

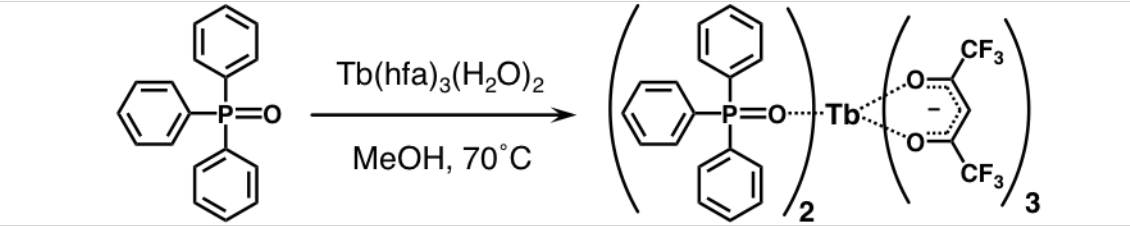

Methanol (50mL) containing $[Tb(hfa)_3(H_2O)_2]$ (294 mg, 0.36 mmol) and triphenylphosphine oxide: tppo (200 mg, 0.72 mmol) was fluxed under stirring for 3 h. The reaction mixture was concentrated with evaporator. Recrystallization from methanol gave colorless crude crystals. Yield: 150 mg (31%).

IR (ART): 1653 (st, C=O), 1250,1140 (st, C-F), 1161, 1122 (st, P=O) cm^{-1}. Elemental analysis calcd. (%) for $C_{51}H_{33}F_{18}O_8P_2Tb$: C 45.83, H 2.49; found: C 45.19, H 2.49.

Preparation of $[Tb(hfa)_3(biphepo)]$ $C_{51}H_{31}F_{18}O_8P_2Tb$:

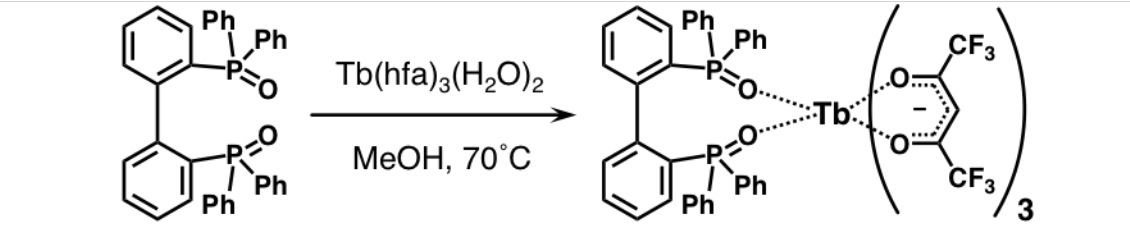

Methanol (100 mL) containing $[Tb(hfa)_3(H_2O)_2]$ (294 mg, 0.36 mmol) and biphepo (200

mg, 0.36 mmol) was refluxed under stirring for 3 h. The reaction mixture was concentrated with evaporator. Recrystallization from methanol gave white crystal. Yield: 176 mg (36%). IR (ART): 1654 (st, C=O), 1253, 1140 (st, C-F), 1180, 1124 (st, P=O) cm^{-1}. Elemental analysis calcd. (%) for $C_{51}H_{31}F_{18}O_8P_2Tb$: C 45.90, H 2.34; found: C 45.53, H 2.43.

Preparation of $[Tb(hfa)_3(dppy)_2]$ $C_{49}H_{31}F_{18}N_2O_8P_2Tb$:

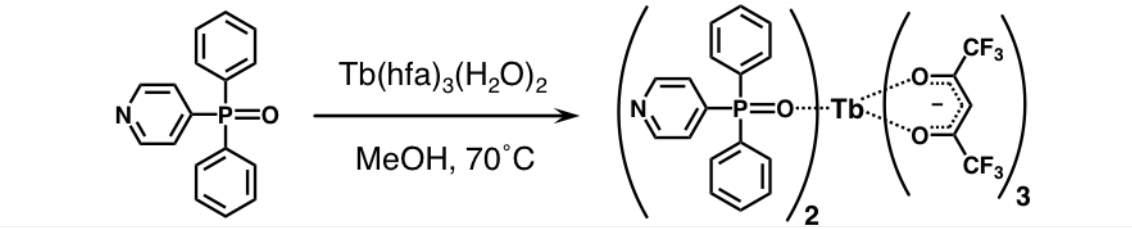

Methanol (50mL) containing $[Tb(hfa)_3(H_2O)_2]$ (294 mg, 0.36 mmol) and dppy (200 mg, 0.72 mmol) was fluxed under stirring for 3 h. The reaction mixture was concentrated with evaporator. Recrystallization from methanol gave colorless crude crystals. Yield: 110 mg (23%).

IR (ART): 1652 (st, C=O), 1251, 1140 (st, C-F), 1170-1108 (st, P=O) cm^{-1}. Elemental analysis calcd. (%) for $C_{49}H_{31}F_{18}N_2O_8P_2Tb$: C 43.97, H 2.33, N 2.09; found: C 44.19, H 2.45, N 1.87.

Preparation of $[Tb(hfa)_3(dpb)]_n$ $C_{45}H_{27}F_{18}O_8P_2Tb$:

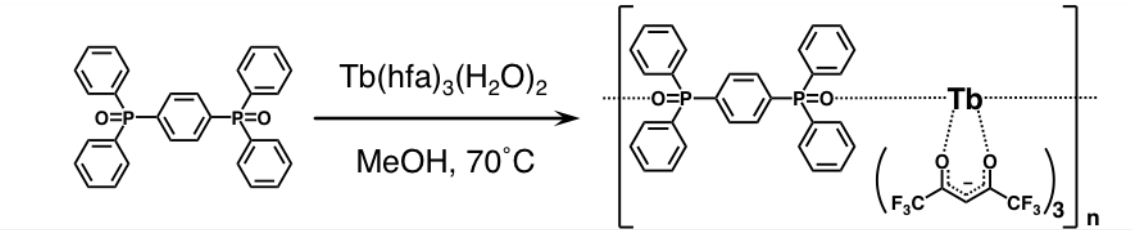

$[Tb(hfa)_3(H_2O)_2]$ (343 mg, 0.42 mmol) and dpb (200 mg, 0.42 mmol) were dissolved in methanol (15 mL). The solution was refluxed while stirring for 3 h to give a white precipitate. The precipitate was filtered, washed with methanol for several times, and dried in vacuum. Yield: 213 mg (40%).

IR (ART): 1652 (st, C=O), 1252, 1138 (st, C-F), 1186-1106 (st, P=O) cm^{-1}. Elemental analysis calcd. (%) for $C_{45}H_{27}F_{18}O_8P_2Tb$: C 42.95, H 2.16; found: C 43.28, H 2.04.

Preparation of $[Tb(hfa)_3(dpbp)]_n$ $C_{51}H_{31}F_{18}O_8P_2Tb$:

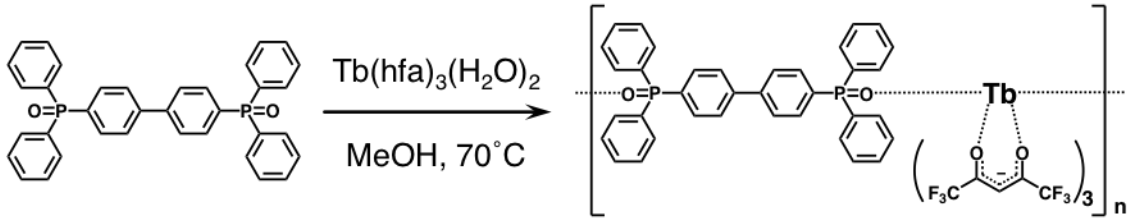

$[Tb(hfa)_3(H_2O)_2]$ (294 mg, 0.36 mmol) and dpbp (200 mg, 0.36 mmol) were dissolved in methanol (15 mL). The solution was refluxed while stirring for 3 h to give a white precipitate. The precipitate was filtered, washed with methanol for several times, and dried in vacuum. Yield: 184 mg (38%).

IR (ART): 1652 (st, C=O), 1250, 1139 (st, C-F), 1182, 1123 (st, P=O) cm^{-1}. Elemental analysis calcd. (%) for $C_{51}H_{31}F_{18}O_8P_2Tb$: C 45.90, H 2.34; found: C 45.65, H 2.19.

Preparation of $[Tb(hfa)_3ZnCl_2(dppy)_2]_n$ $C_{49}H_{31}Cl_2F_{18}N_2O_8P_2TbZn$:

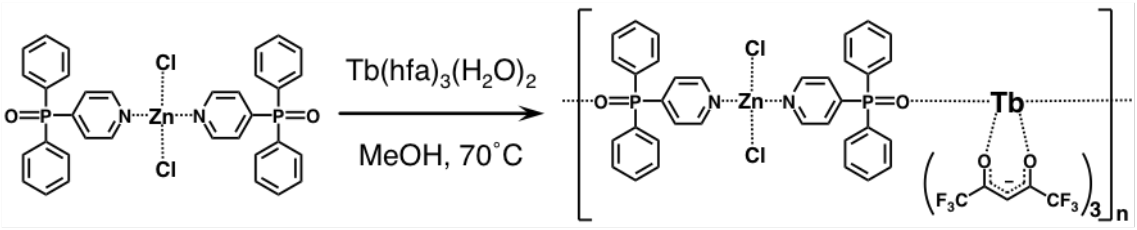

$[Tb(hfa)_3(H_2O)_2]$ (237 mg, 0.29 mmol) and $[ZnCl_2(dppy)_2]$ (200 mg, 0.29 mmol) were dissolved in methanol (15 mL). The solution was refluxed while stirring for 3 h to give a white precipitate. The precipitate was filtered, washed with methanol for several times, and dried in vacuum. Yield: 123 mg (29%). IR (ART): 1649 (st, C=O), 1253, 1181-1132 (st, C-F), 1217-1106 (st, P=O) cm^{-1}. Elemental analysis calcd (%) for $C_{49}H_{31}Cl_2F_{18}N_2O_8P_2TbZn$: C 39.90, H 2.12, N 1.90; found: C 39.56, H 2.35, N 1.86.

Crystallography:

Colorless single crystals of $Tb(hfa)_3$ complexes were mounted on the MiTeGen micromesh using paraffin oil. All measurements were made by using a Rigaku RAXIS RAPID imaging-plate area detector with graphite-monochromated Mo-Kα radiation. Non-hydrogen atoms were refined anisotropically. All calculations were performed by using the crystal-structure crystallographic software package. CIF data was confirmed by using the checkCIF/PLATON service. CCDC-1862802 {for $[Tb(hfa)_3(TPPO)_2]$} , -1862803 {for $[Tb(hfa)_3(dpb)]_n$} and -1862804 {for $[Tb(hfa)_3(dpbp)]_n$} contain the supplementary crystallographic data for this chaper. These data can be obtained free of charge from The Cambridge Crystallographic Data Centre via www.ccdc.cam.ac.uk/data_request/cif.

Optical measurements:

UV−Vis absorption spectra were recorded on a JASCO V-670 spectrometer. Emission and excitation spectra of $Tb(hfa)_3$ complexes were measured with a HORIBA Fluorolog-3 spectrofluorometer and corrected for the response of the detector system. Emission lifetimes (τ_{obs}) of coordination polymers were measured using the third harmonics (355 nm) of a Q-switched Nd:YAG laser (Spectra Physics, INDI-50, FWHM = 5 ns, λ = 1064 nm) and a photomultiplier (Hamamatsu Photonics, R5108, response time ≤ 1.1 ns). The Nd:YAG laser response was monitored with a digital oscilloscope (Sony Tektronix, TDS3052, 500 MHz) synchronized to the single-pulse excitation. Emission lifetimes were determined from the slope of logarithmic plots of the decay profiles. Emission lifetimes in the range 100–400 K were measured using a cryostat (Thermal Block Company, SA-SB245T) and a temperature controller (Oxford Instruments, ITC 502S). The emission quantum yields excited at 350 nm ($\Phi_{\pi\pi^*}$) were estimated using a JASCO F-6300-H spectrometer attached with JASCO ILF-533 integrating sphere unit (ϕ = 100 nm). The wavelength dependence of the detector response and the beam intensity of the Xe light source for each spectrum were calibrated using a standard light source.

3.3 Results and discussion

3.3.1 Structural analyses

The mononuclear $[Tb(hfa)_3(AEC)]$ and polynuclear $[Tb(hfa)_3(AEC)]_n$ ($[Tb(hfa)_3(tppo)_2]$, $[Tb(hfa)_3(biphepo)]$, $[Tb(hfa)_3(dppy)_2]$, $[Tb(hfa)_3(dpb)]_n$, $[Tb(hfa)_3(dpbp)]_n$ and $[Tb(hfa)_3ZnCl_2(dppy)_2]_n$) were synthesized by reacting $[Tb(hfa)_3(H_2O)_2]$ precursor with phosphine oxide ligands in methanol under reflux. Single crystals of mononuclear $[Tb(hfa)_3(AEC)]$ and polynuclear $[Tb(hfa)_3(AEC)]_n$ were prepared by recrystallization from methanol solutions at room temperature (RT). The structural images and crystal data of $[Tb(hfa)_3(tppo)_2]$, $[Tb(hfa)_3(dpb)]_n$ and $[Tb(hfa)_3(dpbp)]_n$ are shown in Figure 3-2 and Table 3-1, respectively. From the single-crystal X-ray structural analysis results, the coordination sites of the Tb^{3+} ion are comprised of three hfa and two phosphine oxide ligands (AEC ligands). Their coordination geometries based on the shape measure estimations are categorized as eight coordinate square antiprism structures (see Table 3-2 and 3-3). Single crystals of $[Tb(hfa)_3(biphepo)]$, $[Tb(hfa)_3(dppy)_2]$ and $[Tb(hfa)_3ZnCl_2(dppy)_2]_n$ were not obtained, and these structure could not be determined.

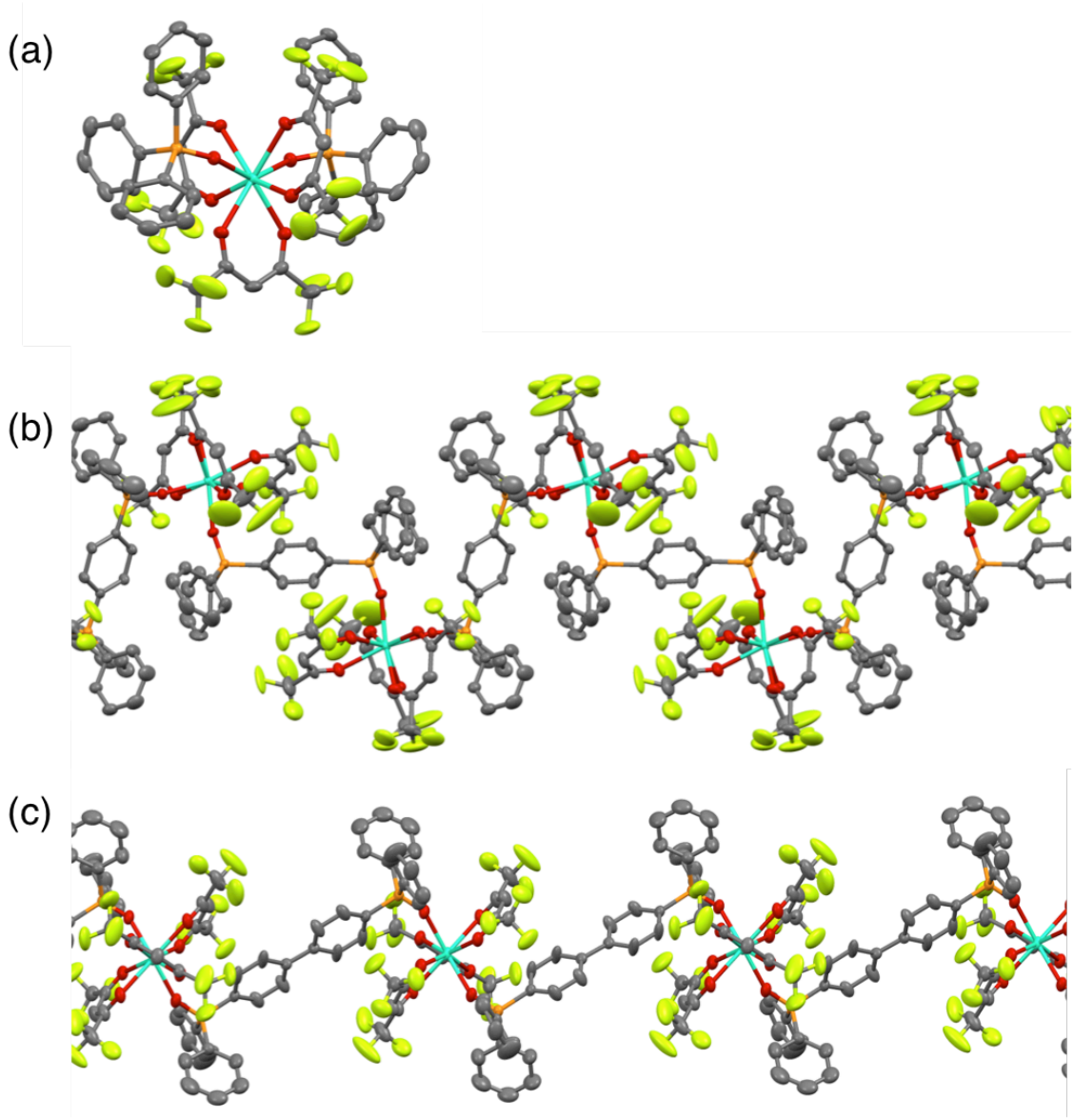

Figure 3-2. Molecular structure of (a)[Tb(hfa)$_3$(tppo)$_2$], (b)[Tb(hfa)$_3$(dpb)]$_n$, and (c)[Tb(hfa)$_3$(dpbp)]$_n$, showing 50% probability displacement ellipsoids. Hydrogen atoms have been omitted for clarity. Green: Tb, red: O, gray: C, yellow: F, and orange: P.

Table 3-1. Crystal data for $[Tb(hfa)_3(tppo)_2]$, $[Tb(hfa)_3(dpb)]_n$ and $[Tb(hfa)_3(dpbp)]_n$

	$[Tb(hfa)_3(tppo)_2]$	$[Tb(hfa)_3(dpb)]_n$	$[Tb(hfa)_3(dpbp)]_n$
chemical formula	$C_{51}H_{33}F_{18}O_8P_2Tb$	$C_{45}H_{27}F_{18}O_8P_2Tb$	$C_{51}H_{31}F_{18}O_8P_2Tb$
formula weight	1336.63	1258.52	1334.62
crystal color, habit	colorless	colorless	colorless
crystal system	monoclinic	triclinic	monoclinic
space group	P 21/n	P -1	C 2/c
a / Å	17.0886(12)	13.1438(8)	23.3994(12)
b / Å	15.4046(10)	13.6705(8)	13.3589(6)
c / Å	20.6049(12)	14.5492(8)	17.0919(8)
α / deg	90	75.619(5)	90
β / deg	93.9897(7)	83.641(6)	97.404(7)
γ / deg	90	76.577(5)	90
V / Å	5411.6(6)	2459.2(3)	5298.2(4)
Z	4	2	4
d_{calc} / g cm^{-3}	1.641	1.700	1673
T / ˚C	-150	23	-150
μ(Mo Kα) / cm^{-1}	1479	1622	1511
max 2θ / deg	27.483	27.482	27.467
measured reflections	12356	11182	6068
unique reflections	721	694	362
R ($I > 2\sigma(I)$)[a)]	0.0338	0.0360	0.0293
R_w ($I > 2\sigma(I)$)[b)]	0.0810	0.0869	0.0748

a) $R = \Sigma||F_o| - |F_c|| / \Sigma|F_o|$.

b) $R_w = [\Sigma w(|F_o| - |F_c|)^2 / \Sigma wF_o^2]^{1/2}$.

Table 3-2. Observed dihedral angles (δ_i), dihedral angles of idealized square antiprism (θ_i) and measure shape criteria, S (D_{4d}) for $[Tb(hfa)_3(tppo)_2]$, $[Tb(hfa)_3(dpb)]_n$ and $[Tb(hfa)_3(dpbp)]_n$.

	$[Tb(hfa)_3(tppo)_2]$			$[Tb(hfa)_3(dpb)]_n$			$[Tb(hfa)_3(dpbp)]_n$		
Edge	θ_i	δ_i	$\delta_i - \theta_i$	θ_i	δ_i	$\delta_i - \theta_i$	θ_i	δ_i	$\delta_i - \theta_i$
O1-O2	0	15.73	15.73	0	11.98	11.98	0	5.05	5.05
O6-O7	77.1	72.87	-4.23	77.1	74.38	-2.72	77.1	74.97	-2.13
O1-O3	77.1	79.15	2.05	77.1	75.06	-2.04	77.1	72.28	-4.82
O1-O4	77.1	81.08	3.98	77.1	73.83	-3.27	77.1	75.52	-1.58
O2-O3	77.1	77.24	0.14	77.1	77.76	0.66	77.1	79.58	2.48
O2-O4	0	12.88	12.88	0	4.08	4.08	0	5.39	5.39
O6-O5	77.1	78.53	1.43	77.1	78.59	1.49	77.1	72.28	-4.82
O6-O8	77.1	79.11	2.01	77.1	81.85	4.75	77.1	79.58	2.48
O7-O8	77.1	77.61	0.51	77.1	72.54	-4.56	77.1	75.52	-1.58
O7-O5	77.1	75.9	-1.2	77.1	77.04	-0.06	77.1	74.97	-2.13
O5-O2	51.6	41.69	-9.91	51.6	49.95	-1.65	51.6	52.33	0.73
O5-O4	51.6	52.48	0.88	51.6	56.39	4.79	51.6	46.43	-5.17
O6-O1	51.6	51.38	-0.22	51.6	43.28	-8.32	51.6	46.43	-5.17
O6-O4	51.6	58.79	7.19	51.6	52.5	0.9	51.6	60.65	9.05
O8-O1	51.6	42.83	-8.77	51.6	49.63	-1.97	51.6	52.33	0.73
O8-O3	51.6	53.75	2.15	51.6	57.72	6.12	51.6	46.47	-5.13
O7-O2	51.6	53.3	1.7	51.6	47.28	-4.32	51.6	46.47	-5.13
O7-O3	51.6	58.88	7.28	51.6	54.88	3.28	51.6	60.18	8.58
	$S(D_{4d}) = 6.44$			$S(D_{4d}) = 4.68$			$S(D_{4d}) = 4.66$		

Table 3-3. Observed dihedral angles (δ_i), dihedral angles of idealized trigonal dodecahedron (θ_i) and measure shape criteria, S (D_{2d}) for $[Tb(hfa)_3(tppo)_2]$, $[Tb(hfa)_3(dpb)]_n$ and $[Tb(hfa)_3(dpbp)]_n$.

	$[Tb(hfa)_3(tppo)_2]$			$[Tb(hfa)_3(dpb)]_n$			$[Tb(hfa)_3(dpbp)]_n$		
Edge	θ_i	δ_i	$\delta_i - \theta_i$	θ_i	δ_i	$\delta_i - \theta_i$	θ_i	δ_i	$\delta_i - \theta_i$
O1-O2	29.86	15.73	-14.13	29.86	11.98	-17.88	29.86	5.05	-24.81
O6-O7	61.48	72.87	11.39	61.48	74.38	12.9	61.48	74.97	13.49
O1-O3	74.29	79.15	4.86	74.29	75.06	0.77	74.29	72.28	-2.01
O1-O4	74.29	81.08	6.79	74.29	73.83	-0.46	74.29	75.52	1.23
O2-O3	61.48	77.24	15.76	61.48	77.76	16.28	61.48	79.58	18.1
O2-O4	29.86	12.88	-16.98	29.86	4.08	-25.78	29.86	5.39	-24.47
O6-O5	61.48	78.53	17.05	61.48	78.59	17.11	61.48	72.28	10.8
O6-O8	74.29	79.11	4.82	74.29	81.85	7.56	74.29	79.58	5.29
O7-O8	76.62	77.61	0.99	76.62	72.54	-4.08	76.62	75.52	-1.1
O7-O5	74.84	75.9	1.06	74.84	77.04	2.2	74.84	74.97	0.13
O5-O2	54.51	41.69	-12.82	54.51	49.95	-4.56	54.51	52.33	-2.18
O5-O4	48.09	52.48	4.39	48.09	56.39	8.3	48.09	46.43	-1.66
O6-O1	47.76	51.38	3.62	47.76	43.28	-4.48	47.76	46.43	-1.33
O6-O4	54.48	58.79	4.31	54.48	52.5	-1.98	54.48	60.65	6.17
O8-O1	52.57	42.83	-9.74	52.57	49.63	-2.94	52.57	52.33	-0.24
O8-O3	52.85	53.75	0.9	52.85	57.72	4.87	52.85	46.47	-6.38
O7-O2	47.34	53.3	5.96	47.34	47.28	-0.06	47.34	46.47	-0.87
O7-O3	52.63	58.88	6.25	52.63	54.88	2.25	52.63	60.18	7.55
	$S(D_{2d}) = 9.54$			$S(D_{2d}) = 10.4$			$S(D_{2d}) = 10.6$		

3.3.2 Photophysical properties at room temperature

The emission spectra of the mononuclear [Tb(hfa)$_3$(AEC)] and polynuclear [Tb(hfa)$_3$(AEC)]$_n$ complexes in solid state at RT are shown in Figure 3-3. Emission bands are observed at 487, 548, 582, and 623 nm, which are attributed to 4*f*–4*f* transitions of the Tb^{3+} complexes ($^5D_4 \rightarrow {}^7F_J$, where J = 6, 5, 4, and 3, respectively). The Stark splitting shapes at 548nm ($^5D_4 \rightarrow {}^7F_5$) for mononuclear [Tb(hfa)$_3$(AEC)] are similar to those for polynuclear [Tb(hfa)$_3$(AEC)]$_n$. Generally, the Stark splitting shape of emission spectrum of a lanthanide complex is dependent on the coordination geometry. From these result, the coordination geometries of [Tb(hfa)$_3$(biphepo)], [Tb(hfa)$_3$(dppy)$_2$] and [Tb(hfa)$_3$ZnCl$_2$(dppy)$_2$]$_n$ should also be eight-coordinate square antiprism structures.

The time-resolved emission decay profiles of mononuclear [Tb(hfa)$_3$(AEC)] and polynuclear [Tb(hfa)$_3$(AEC)]$_n$ complexes in solid state at 300 K are shown in Figure 3-4. The emission lifetimes of the [Tb(hfa)$_3$(AEC)] complexes (τ_{obs}) were determined from the slope of the logarithmic decay profiles. The time-resolved emission profiles of the mononuclear [Tb(hfa)$_3$(AEC)] and polynuclear [Tb(hfa)$_3$(AEC)]$_n$ complexes showed microsecond-scale emission lifetime by estimating single-exponential fitting.

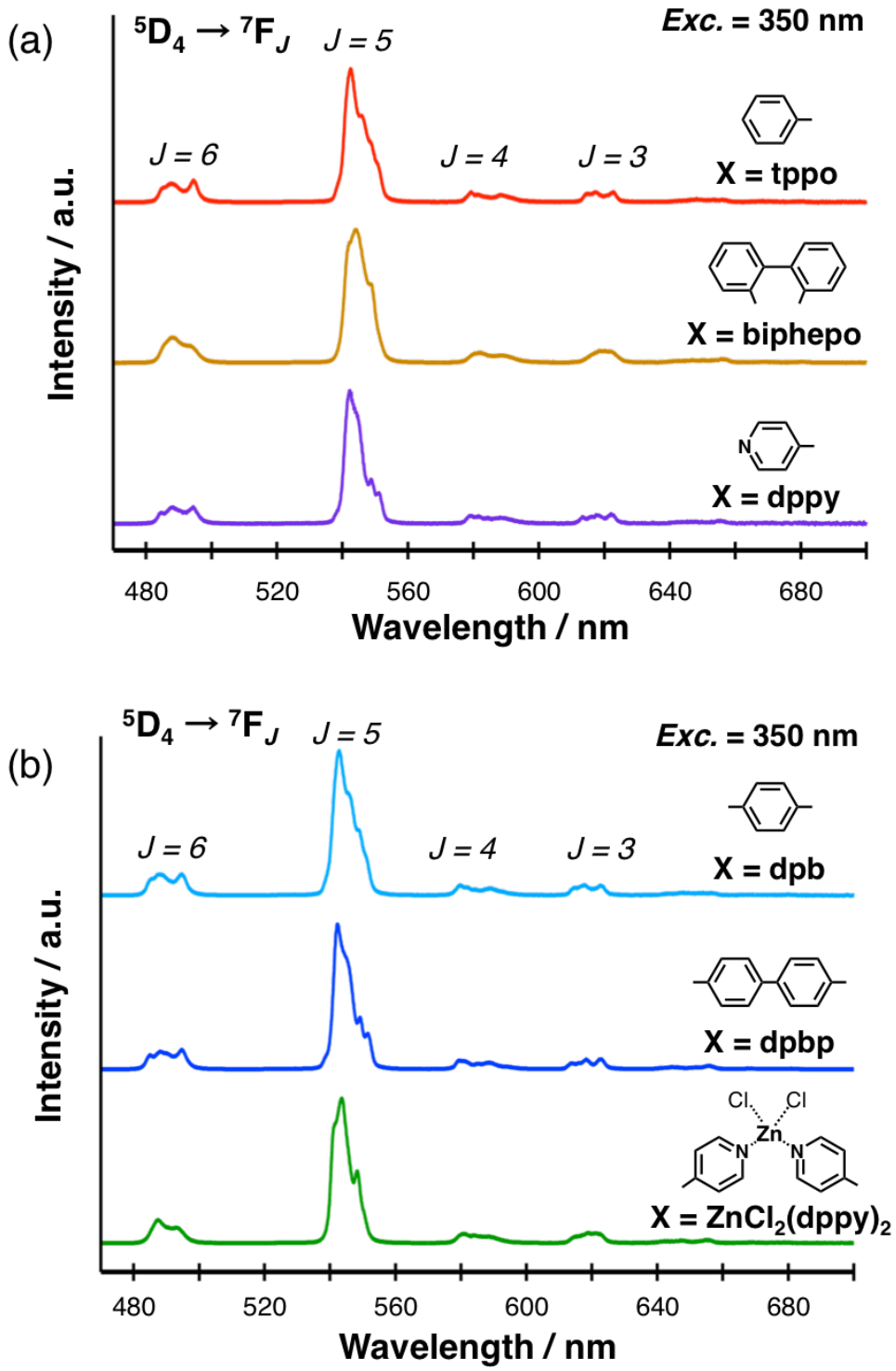

Figure 3-3. Emission spectra of (a) mononuclear [Tb(hfa)$_3$(AEC)] and (b) polynuclear [Tb(hfa)$_3$(AEC)]n in the solid state at room temperature. Excited at 350 nm.

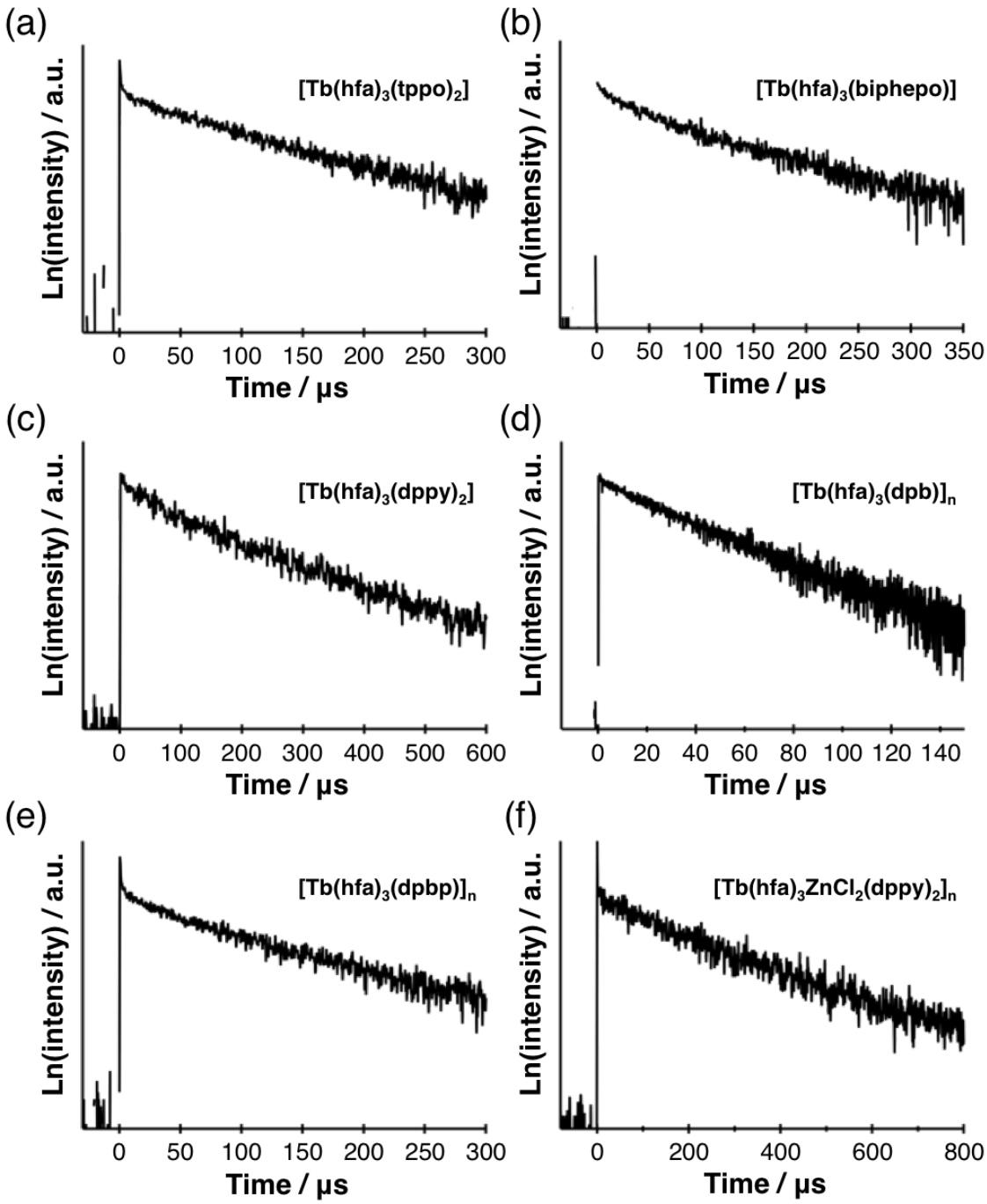

Figure 3-4. Emission lifetime decays of each $Tb(hfa)_3$ complex in the solid state at 300 K. Excited at 355 nm. (Third harmonics of Q-switched Nd:YAG laser. fwhm =5 ns, λ = 1064 nm).

The overall emission quantum yields ($\Phi_{\pi\pi^*}$) by excitation of the hfa ligands in solid state at RT were measured using the integration sphere. The photophysical parameters ($\Phi_{\pi\pi^*}$ and $\tau_{obs,\ RT}$) are summarized in Table 3-4. The $\Phi_{\pi\pi^*}$ values of $[Tb(hfa)_3(tppo)_2]$, $[Tb(hfa)_3(biphepo)]$ and $[Tb(hfa)_3(dppy)_2]$ are 9.2, 11, and 10%, respectively. In contrast, the $\Phi_{\pi\pi^*}$ values of $[Tb(hfa)_3(dpbp)]_n$ (17%) and $[Tb(hfa)_3ZnCl_2(dppy)_2]_n$ (35%) are significantly larger than those of mononuclear $[Tb(hfa)_3(AEC)]$ complexes, although the $\Phi_{\pi\pi^*}$ value of $[Tb(hfa)_3(dpb)]_n$ (10%) is similar to those of mononuclear $[Tb(hfa)_3(AEC)]$ complexes. These results indicate that the photosensitized emission quantum yields of polynuclear Tb^{3+} complexes are dependent on the phosphine oxide linker moiety. The author considers that introduction of phosphine oxide ligand affects the photosensitized energy transfer process between the hfa ligands and the Tb^{3+} ion.

Table 3-4. Photophysical properties of $Tb(hfa)_3(AEC)$.

	Confomation	Φ_{tot}	$\tau_{obs,\ RT}$
		%	μs
$[Tb(hfa)_3(tppo)_2]$	Mononuclear	9.2	209
$[Tb(hfa)_3(biphepo)]$	Mononuclear	11	267
$[Tb(hfa)_3(dppy)_2]$	Mononuclear	10	482
$[Tb(hfa)_3(dpb)]_n$	Polynuclear	9.7	73
$[Tb(hfa)_3(dpbp)]_n$	Polynuclear	17	215
$[Tb(hfa)_3ZnCl_2(dppy)_2]_n$	Polynuclear	35	610

3.3.3 Temperature-dependent emission properties

To estimate the effect of BEnT in the mononuclear [$Tb(hfa)_3(AEC)$] and polynuclear [$Tb(hfa)_3(AEC)]_n$, the temperature-dependent emission lifetimes in solid state were measured in the range 90-400 K. The logarithmic lifetime profiles of a typical Tb^{3+} complex with tppo ligands, [$Tb(hfa)_3(tppo)_2$], are shown in Figure 3-5a. From Figure 3-5a, emission decay profiles from 100 K to 200 K were shown single-exponential decays. Emission decay profiles from 250 K to 400 K were shown multi-exponential decays. In higher temperature range, the author considers that at least two types of emission species are coexisted in solid states. The time-resolved emission profiles of [$Tb(hfa)_3(tppo)_2$] analyzed single-exponential decays at each temperature by treating emission lifetime as an average value. The emission lifetimes of [$Tb(hfa)_3(tppo)_2$] at 100, 200, 300, and 400 K were 806, 709, 86, and 5.6 μs, respectively. The emission lifetimes of [$Tb(hfa)_3(tppo)_2$] were gradually shorter with increasing temperature, because the BEnT process from emitting level of the Tb^{3+} ion ($^5D_4$) to the triplet state of the hfa ligand (T_1) are enhanced. The temperature-dependent emission lifetimes were observed for all of the mononuclear [$Tb(hfa)_3(AEC)$] and polynuclear [$Tb(hfa)_3(AEC)]_n$（see Figures 3-5 and 3-6）.

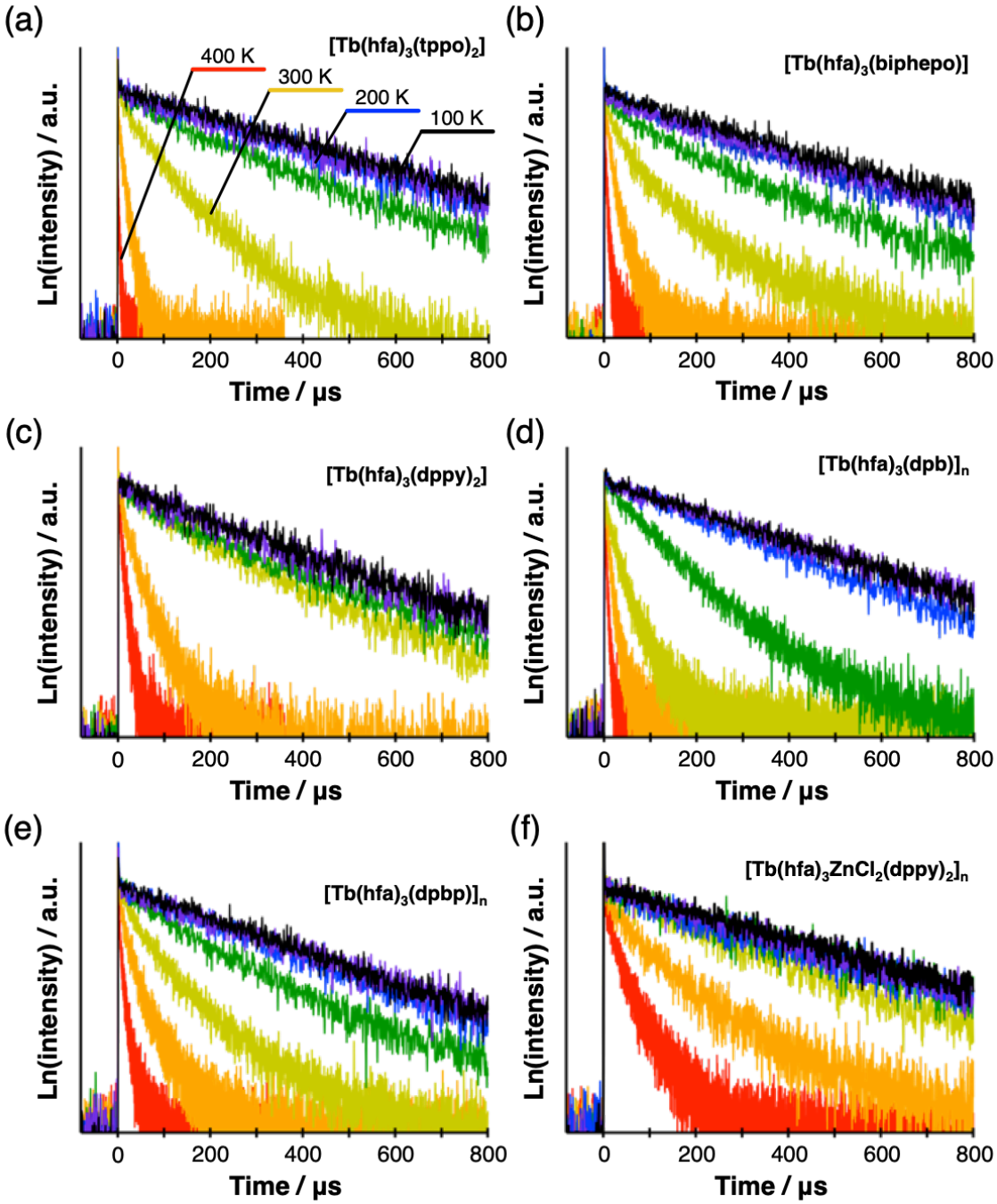

Figure 3-5. Temperature-dependent emission lifetime decays of each $Tb(hfa)_3$ complex in the solid state among 100-400 K. Excited at 355 nm (third harmonics of Q-switched Nd:YAG laser. fwhm =5 ns, λ = 1064 nm, black line: 100 K, purple line: 150 K, blue line: 200 K, green line: 250 K, yellow line: 300K, orange line: 350 K, red line 400 K.)

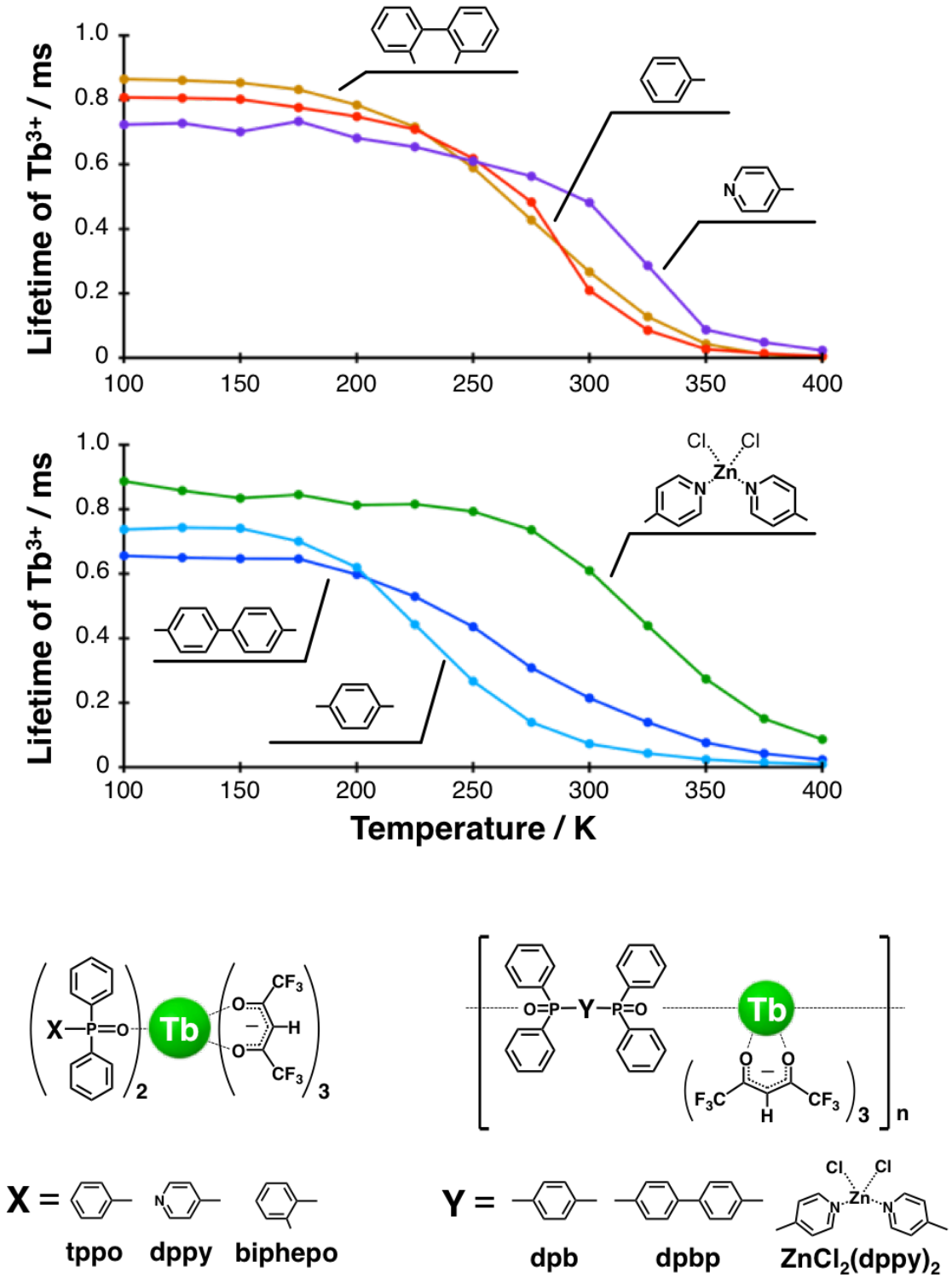

Figure 3-6. Temperature-dependent emission lifetime of each $Tb(hfa)_3$ complex in the solid state among 100-400 K.

To analyze the BEnT mechanism, the BEnT rate constants (k_{BEnT}) were estimated by kinetic analysis. The temperature dependence of k_{BEnT} is expected to follow Arrhenius-type equation with an activation energy ΔE_a,[17] k_{BEnT} is given by

$$\ln\left(\frac{1}{\tau_{obs}}-\frac{1}{\tau_{90K}}\right)=\ln k_{BEnT}=\ln A-\frac{\Delta E_a}{R}\cdot T^{-1} \qquad (3.1)$$

where τ_{obs}, τ_{90K}, A, ΔE_a, R and T are the observed emission lifetime, standard emission lifetime at 90 K, frequency factor, activation energy, gas constant and temperature, respectively. Arrhenius plots of BEnT for the mononuclear [Tb(hfa)$_3$(AEC)] and polynuclear [Tb(hfa)$_3$(AEC)]$_n$ are shown in Figure 3-7. Arrhenius plots of mononuclear [Tb(hfa)$_3$(AEC)] and polynuclear [Tb(hfa)$_3$(AEC)]$_n$ were fitted with linear approximation by least-squares regression. These results indicate that the BEnT process is only composed of between Tb^{3+} ion and hfa ligand. The ΔE_a and A values estimated using equation 3.1 are summarized in Table 3-5. The ΔE_a values of polynuclear [Tb(hfa)$_3$(AEC)]$_n$ ([Tb(hfa)$_3$(dpb)]$_n$, [Tb(hfa)$_3$(dpbp)]$_n$ and [Tb(hfa)$_3$ZnCl$_2$(dppy)]$_n$) were smaller than those of mononuclear [Tb(hfa)$_3$(AEC)] ([Tb(hfa)$_3$(tppo)$_2$], [Tb(hfa)$_3$(biphepo)] and [Tb(hfa)$_3$(dppy)$_2$]). The A values of polynuclear [Tb(hfa)$_3$(AEC)]$_n$ were also smaller than those of mononuclear [Tb(hfa)$_3$(AEC)].

To be more precise in the polynuclear [Tb(hfa)$_3$(AEC)]$_n$, the ΔE_a value of [Tb(hfa)$_3$(dpb)]$_n$ (ΔE_a = 1700 cm^{-1}) and [Tb(hfa)$_3$(dpbp)]$_n$ (ΔE_a = 1900 cm^{-1}) were smaller than those of [Tb(hfa)$_3$ZnCl$_2$(dppy)]$_n$ (ΔE_a = 2500 cm^{-1}). The A value of [Tb(hfa)$_3$(dpb)]$_n$ (A = 4.06×10^7 s^{-1}) and [Tb(hfa)$_3$(dpbp)]$_n$ (A = 3.68×10^7 s^{-1}) were also smaller than those of [Tb(hfa)$_3$ZnCl$_2$(dppy)]$_n$ (A = 7.92×10^7 s^{-1}). The smaller ΔE_a and A values of

polynuclear $[Tb(hfa)_3(AEC)]_n$ promote effective activation of BEnT at lower temperatures, resulting in high-sensitive temperature-dependent phosphor materials over a wide range temperature. The phosphine oxide ligand (activation energy controller: AEC) should dominate not only the Tb^{3+} molecular structures (mononuclear or polymer) but also the BEnT process (ΔE_a and A values).

Table 3-5. Arrhenius parameters of $[Tb(hfa)_3(AEC)]$.

	Confomation	ΔE_a	A
		cm^{-1}	s^{-1}
$[Tb(hfa)_3(tppo)_2]$	Mononuclear	3200	1.98×10^{10}
$[Tb(hfa)_3(biphepo)]$	Mononuclear	4000	3.56×10^{11}
$[Tb(hfa)_3(dppy)_2]$	Mononuclear	3600	1.06×10^{10}
$[Tb(hfa)_3(dpb)]_n$	Polynuclear	1700	4.06×10^{7}
$[Tb(hfa)_3(dpbp)]_n$	Polynuclear	1900	3.68×10^{7}
$[Tb(hfa)_3ZnCl_2(dppy)_2]_n$	Polynuclear	2500	7.92×10^{7}

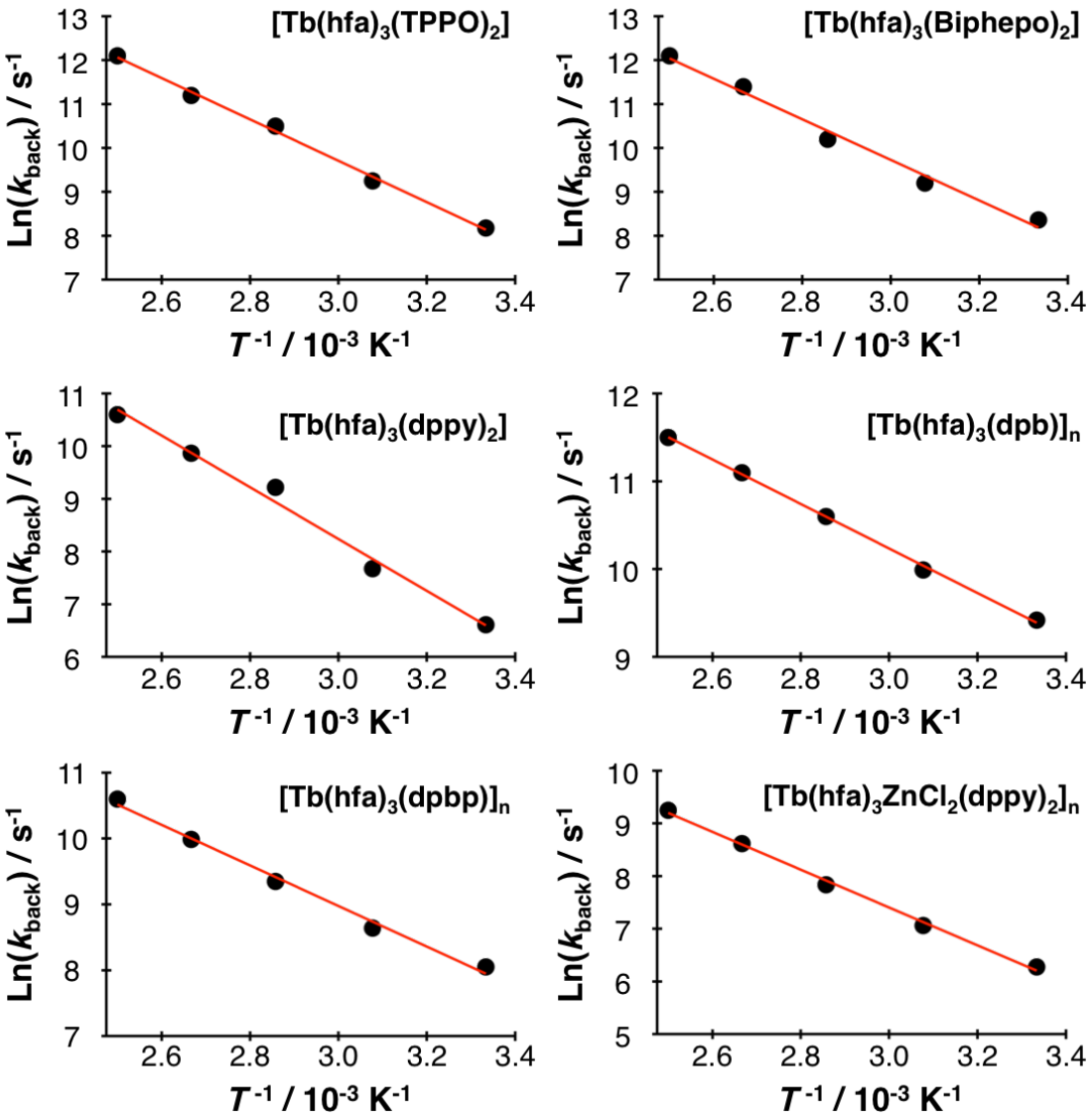

Figure 3-7. Arrhenius plots of each $Tb(hfa)_3$ complex in the solid state.

The BEnT process diagram is shown in Figure 3-8. The activation energy ΔE_a means the energy barrier for the excitation energy transfer from Tb^{3+} ion to hfa ligand. The frequency factor *A* means the event probability of the BEnT process. From Table 3-5, the *A* values of mononuclear $[Tb(hfa)_3(AEC)]$ were 1000 times larger than those of polynuclear $[Tb(hfa)_3(AEC)]_n$. The author considers that the *A* values are correlated with the overlapping of molecular orbital between Tb^{3+} ion and hfa ligand. It is assumed that different excited states are formed between Tb^{3+} ion and hfa ligand with mononuclear $[Tb(hfa)_3(AEC)]$ and polynuclear $[Tb(hfa)_3(AEC)]_n$. Mononuclear $[Tb(hfa)_3(AEC)]$ has strong electron correlation between Tb^{3+} ion and hfa ligand and occurs localization of the excited state, resulting in a high *A* value. On the other hand, polynuclear $[Tb(hfa)_3(AEC)]_n$ has weak electron correlation between Tb^{3+} ion, resulting in a small *A* value. The excited state of Tb ion in polynuclear $[Tb(hfa)_3(AEC)]_n$ is delocalized through the polymer chain. (Figure 3-9)

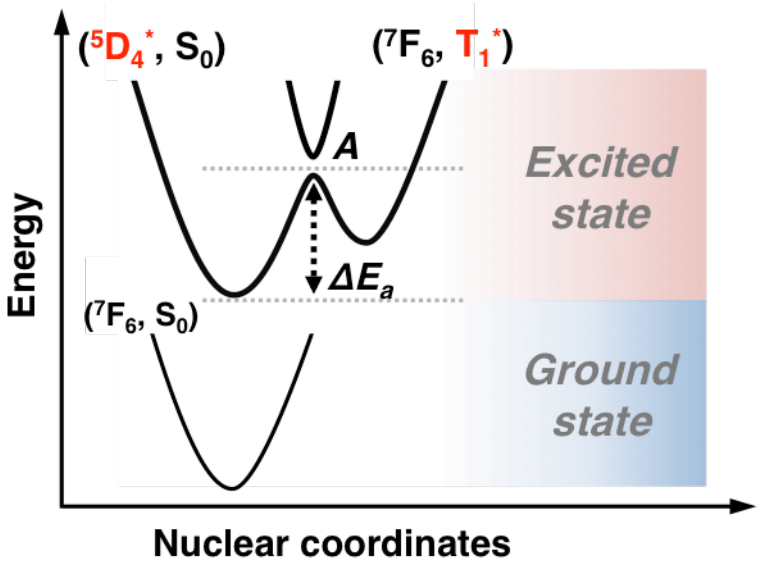

Figure 3-8. Proposal energy diagram of $Tb(hfa)_3$ complex.

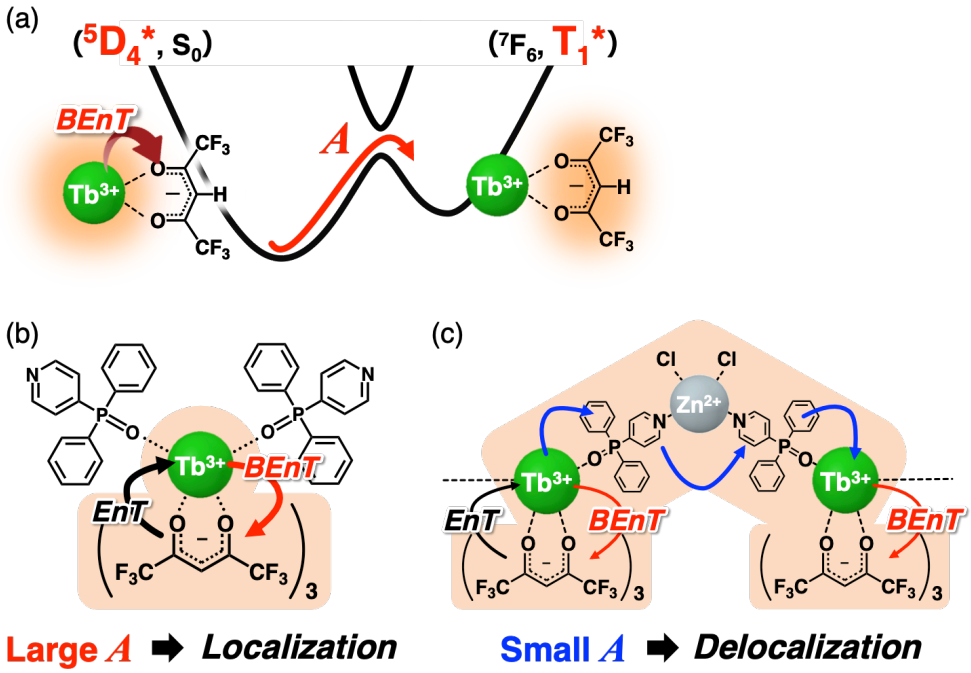

Figure 3-9. (a) Interpretation of frequency facter *A*. (b) Excitation enegy localization image of mononuclear $[Tb(hfa)_3(dppy)_2]$. (c) Excitation enegy delocalization image of polynuclear $[Tb(hfa)_3ZnCl_2(dppy)_2]$.

Based on above assumptions, it shows that the results of Φtot were opposite between Tb^{3+} and Eu^{3+} complexes. According to Tb^{3+} complexes, the Φ_{tot} values of $[Tb(hfa)_3(dppy)_2]$ and $[Tb(hfa)_3ZnCl_2(dppy)_2]_n$ were 10% and 35%, respectively. In the mononuclear complex $[Tb(hfa)_3(dppy)_2]$, the localization effect of the excited state leads to enhance both of photosensitized energy transfer and back energy transfer. For this reason, the effective BEnT process from excited Tb^{3+} ion leads to increase the non-radiative rate constant (k_{nr}), and the mononuclear complex $[Tb(hfa)_3(dppy)_2]$ showed a low Φ_{tot}. In the case of the polymer complex $[Tb(hfa)_3ZnCl_2(dppy)_2]_n$, the delocalization effect of the excited state between Tb^{3+} ion and hfa ligand leads to

suppress both of photosensitized energy transfer and back energy transfer. As the result, the effective BEnT process from excited Tb^{3+} ion leads to decrease the k_{nr}, and the polynuclear complex $[Tb(hfa)_3ZnCl_2(dppy)_2]_n$ showed a high Φ_{tot}.

On the other hand, the Φ_{tot} values of $[Eu(hfa)_3(dppy)_2]$ and $[Eu(hfa)_3ZnCl_2(dppy)_2]_n$ were 64% and 28%, respectively. $Eu(hfa)_3$ complexes do not show the BEnT process like $Tb(hfa)_3$ complexes. The localization effect of the excited state leads to enhance the photosensitized energy transfer, and the mononuclear complex $[Eu(hfa)_3(dppy)_2]$ showed a high Φ_{tot}. In the case of the polymer complex $[Eu(hfa)_3ZnCl_2(dppy)_2]_n$, the delocalization effect of the excited state between Eu^{3+} ion and hfa ligand leads to suppress the photosensitized energy transfer, resulting in a low Φ_{tot}.

Table 3-6. Emission quantum yields Φ_{tot} of Tb^{3+} and Eu^{3+} complexes.

	Φ_{tot}		Φ_{tot}
	%		%
$[Tb(hfa)_3(tppo)_2]$	9.2	$[Eu(hfa)_3(tppo)_2]$	51
$[Tb(hfa)_3(biphepo)]$	11	$[Eu(hfa)_3(biphepo)]$	55
$[Tb(hfa)_3(dppy)_2]$	10	$[Eu(hfa)_3(dppy)_2]$	64
$[Tb(hfa)_3(dpb)]_n$	9.7	$[Eu(hfa)_3(dpb)]_n$	31
$[Tb(hfa)_3(dpbp)]_n$	17	$[Eu(hfa)_3(dpbp)]_n$	29
$[Tb(hfa)_3ZnCl_2(dppy)_2]_n$	35	$[Eu(hfa)_3ZnCl_2(dppy)_2]_n$	28

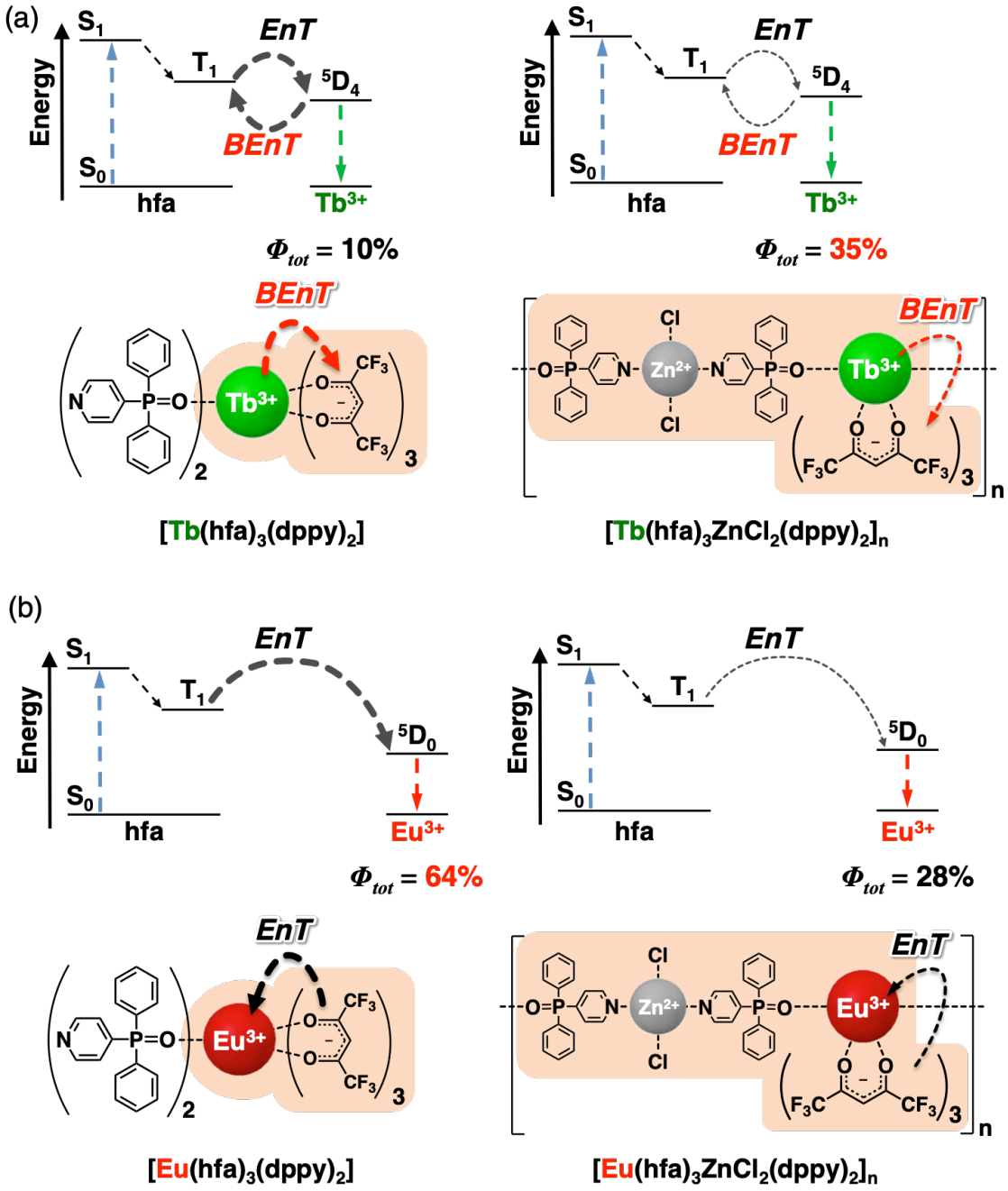

Figure 3-10. (a) Relationships between Φ_{tot} and A of $Tb(hfa)_3$ complexes. (b) Relationships between Φ_{tot} and A of $Eu(hfa)_3$ complexes.

3.3.4 Phosphorescence properties of mononuclear [Gd(hfa)$_3$(AEC)] and polynuclear [Gd(hfa)$_3$(AEC)]$_n$

The calculated ΔE_a and A values of mononuclear [Tb(hfa)$_3$(AEC)] and polynuclear [Tb(hfa)$_3$(AEC)]$_n$ are directly linked to the triplet levels of hfa ligands in the Tb(hfa)$_3$ complexes. In this chapter, to estimate the triplet levels of the hfa ligands, mononuclear [Gd(hfa)$_3$(AEC)] and polynuclear [Gd(hfa)$_3$(AEC)]$_n$ ([Gd(hfa)$_3$(tppo)$_2$], [Gd(hfa)$_3$(biphepo)], [Gd(hfa)$_3$(dppy)$_2$], [Gd(hfa)$_3$(dpb)]$_n$, [Gd(hfa)$_3$(dpbp)]$_n$ and [Gd(hfa)$_3$ZnCl$_2$(dppy)]$_n$) were prepared by the same synthetic method as that used to prepare the mononuclear [Tb(hfa)$_3$(AEC)] and polynuclear [Tb(hfa)$_3$(AEC)]$_n$. Generally, the triplet state properties of photosensitized ligands in lanthanide complexes can be evaluated by phosphorescence measurements of the Gd^{3+} complexes, because the excited energy level of the Gd^{3+} ion is higher than the T_1 level of photosensitized hfa ligand. The phosphorescence spectra of the mononuclear [Gd(hfa)$_3$(AEC)] and polynuclear [Gd(hfa)$_3$(AEC)]$_n$ in solid states at 100 K are shown in Figure 3-9. The phosphorescence spectrum shapes of the polynuclear [Gd(hfa)$_3$(dpb)]$_n$ and [Gd(hfa)$_3$(dpbp)]$_n$ are broader than those of the mononuclear [Gd(hfa)$_3$(AEC)] and polynuclear [Gd(hfa)$_3$ZnCl$_2$(dppy)$_2$]$_n$ complexes. These results indicate that the vibrational structure of the excited hfa ligand in the polynuclear [Gd(hfa)$_3$(dpb)]$_n$ and [Gd(hfa)$_3$(dpbp)]$_n$ complexes are considerably different from those of the mononuclear [Gd(hfa)$_3$(AEC)] and polynuclear [Gd(hfa)$_3$ZnCl$_2$(dppy)$_2$]$_n$ complexes. The broader phosphorescence bands of [Gd(hfa)$_3$(dpb)]$_n$ and [Gd(hfa)$_3$(dpbp)]$_n$ could be caused by the change of the potential curvature of the triplet state in the excited hfa ligands.

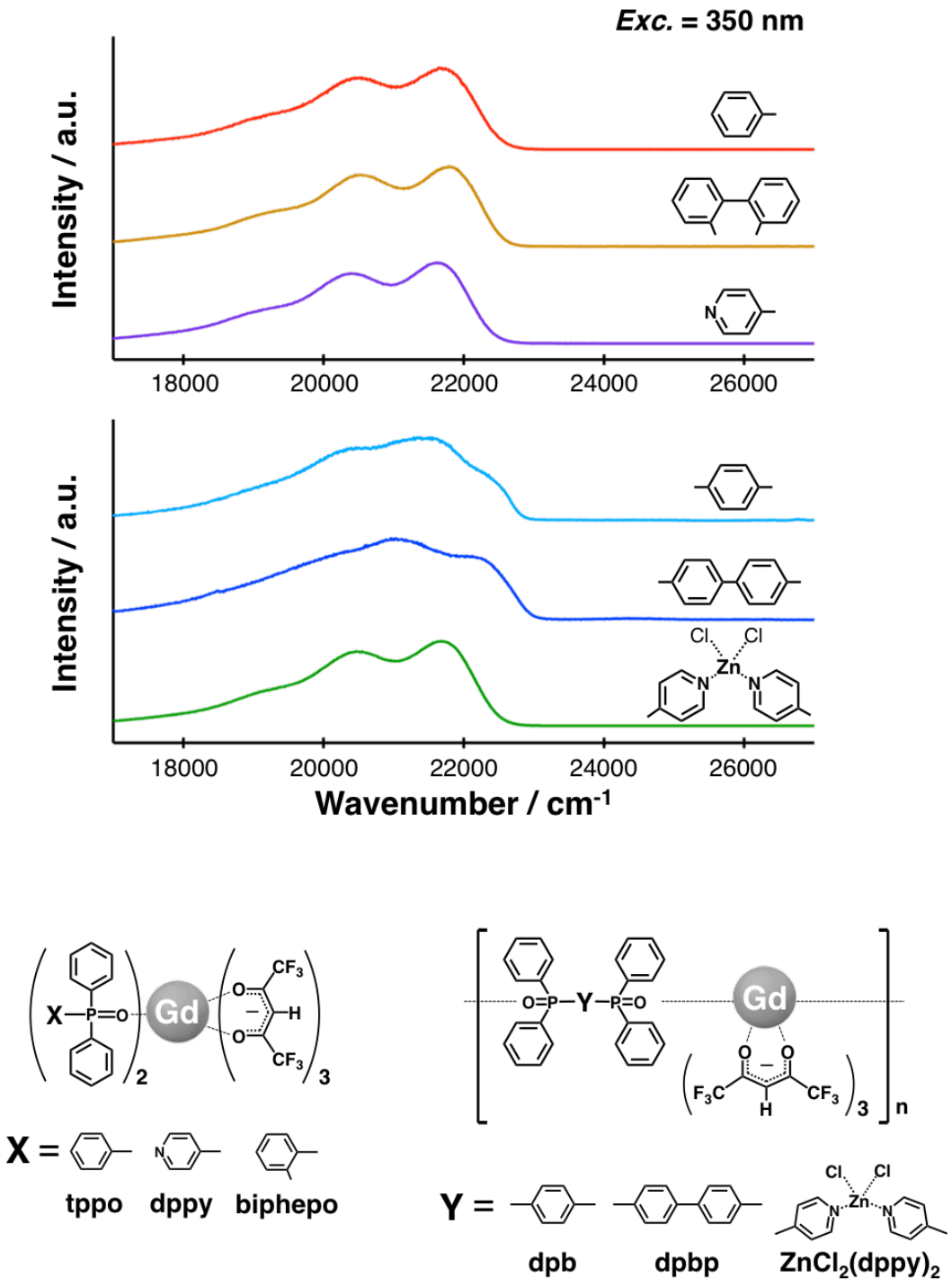

Figure 3-11. Phosphorescence spectra of mononuclear $[Gd(hfa)_3(AEC)]$ and polynuclear $[Gd(hfa)_3(AEC)]_n$ in the solid state at 100 K. Excited at 350 nm. Chemical structure of $Gd(hfa)_3$(phosphine oxide) complexes.

From the phosphorescence spectra, the estimated triplet energy levels of the hfa ligands in the Gd^{3+} complexes $E(T_1)$ are summarized in Table 3-6. The energy gap $\Delta E(T_1\text{-}^5D_4)$ between the T_1 level of the hfa ligands and emitting level of Tb^{3+} (energy gap of $^5D_4$ = 20400 cm^{-1}) are also summarized in Table 3-6. The $\Delta E(T_1\text{-}^5D_4)$ values of the polynuclear Tb^{3+} complexes $[Tb(hfa)_3(dpb)]_n$ and $[Tb(hfa)_3(dpbp)]_n$ were larger than those of mononuclear $[Tb(hfa)_3(AEC)]$ complexes, although the ΔE_a values of the BEnT process for $[Tb(hfa)_3(dpb)]_n$ and $[Tb(hfa)_3(dpbp)]_n$ are smaller than those of mononuclear $[Tb(hfa)_3(AEC)]$ complexes. From these photophysical conflicts, the author propose that the BEnT process is related to the triplet states lifetimes of hfa ligands in our systems.

Table 3-7. Triplet energies and phosphorescence lifetimes of hfa ligands.

	Conformation	$E(T_1)$	$\Delta E(T_1\text{-}^5D_4)$	$\tau_{obs,\,1}$	$\tau_{obs,\,2}$
		cm^{-1}	cm^{-1}	ms	ms
$[Gd(hfa)_3(tppo)_2]$	Mononuclear	21700	1300	2.00 (70%)	9.12 (30%)
$[Gd(hfa)_3(biphepo)]$	Mononuclear	21800	1400	2.94 (68%)	9.41 (32%)
$[Gd(hfa)_3(dppy)_2]$	Mononuclear	21600	1200	1.96 (71%)	8.25 (29%)
$[Gd(hfa)_3(dpb)]_n$	Polynuclear	22400	2000	3.31 (79%)	9.54 (21%)
$[Gd(hfa)_3(dpbp)]_n$	Polynuclear	22300	1900	3.30 (80%)	10.2 (20%)
$[Gd(hfa)_3ZnCl_2(dppy)_2]_n$	Polynuclear	21700	1300	2.02 (65%)	7.75 (35%)

Here, the time-resolved phosphorescence measurements were performed to estimation of the triplet state lifetimes on the excited hfa ligands. The logarithmic lifetime profiles of the Gd^{3+} complexes are shown in Figure 3-10, and the calculated phosphorescence lifetimes are summarized in Table 3-6. The time-resolved emission profiles exhibited double exponential decay at 100 K. Note that the $Tb(hfa)_3$ units is composed of three identical hfa ligands from single-crystal X-ray structural analyses. The double exponential decay of hfa phosphorescence is caused by the presence of at least two types of excited hfa ligands in the solid state. The phosphorescence lifetimes of the polynuclear $[Gd(hfa)_3(dpb)]_n$ and $[Gd(hfa)_3(dpbp)]_n$ complexes are longer than those of the mononuclear $[Gd(hfa)_3(AEC)]$ and polynuclear $[Gd(hfa)_3ZnCl_2(dppy)_2]_n$ complexes.

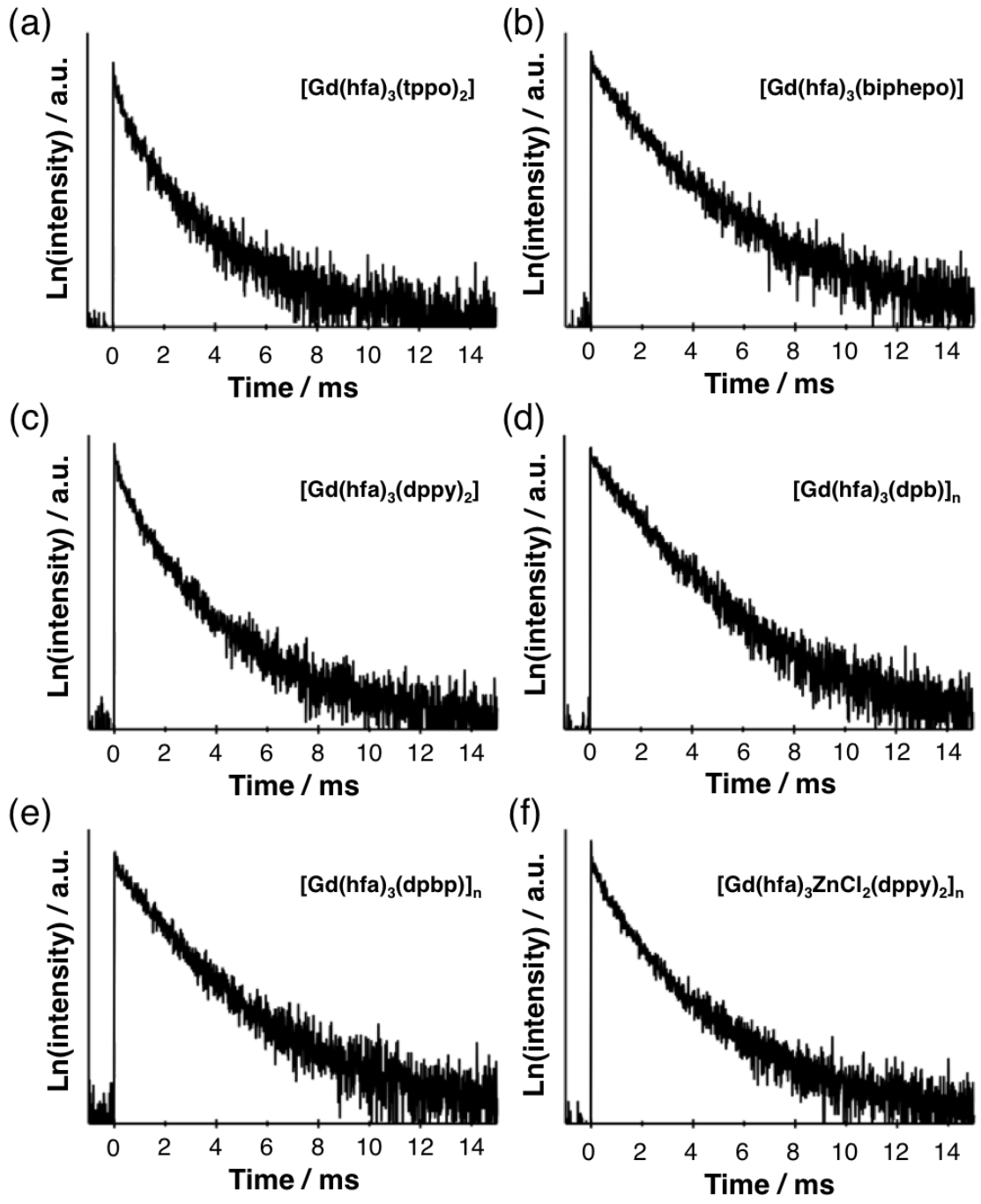

Figure 3-12. Phosphorescence lifetime decays of each $Gd(hfa)_3$ complex in the solid state at 100 K. Excited at 355 nm. (Time delay = 0 ms, third harmonics of Q-switched Nd:YAG laser. fwhm =5 ns, λ = 1064 nm).

Here, the author considers that the polynuclear $[Gd(hfa)_3(dpb)]_n$ and $[Gd(hfa)_3(dpbp)]_n$ complexes promote energy transfer hopping (migration) of excited Tb^{3+} ions on the dpb and dpbp linker ligands, [36] resulting in delocalization of the excited triplet state of hfa ligand. This excited delocalization is related to the broader phosphorescence spectra and long phosphorescence lifetimes of the hfa ligands, which promotes ligand-assisted BEnT (Figure 3-11a). The excited states of mononuclear $[Tb(hfa)_3(AECs)]$ complexes with large ΔE_a and large A values only depend on localization between Tb^{3+} and hfa ligands in the forward and back energy transfer process, resulting in short phosphorescence lifetime and large frequency factor A (Figure 3-11b). For the polynuclear $[Tb(hfa)_3ZnCl_2(dppy)_2]_n$ complex, the ΔE_a and A values are similar to those of the polynuclear $[Tb(hfa)_3(dpb)]_n$ and $[Tb(hfa)_3(dpbp)]_n$ complexes. However, the phosphorescence spectrum shape of the polynuclear $[Gd(hfa)_3ZnCl_2(dppy)_2]_n$ complex is the same as that of mononuclear $[Gd(hfa)_3(dppy)_2]$ complex. From these results, the author considers that $[Tb(hfa)_3ZnCl_2(dppy)_2]_n$ shows localized forward and back energy transfer between the hfa and Tb^{3+} ions (short phosphorescent lifetimes and phosphorescent spectrum shapes), and delocalized energy hopping of excited Tb^{3+} ions via the phosphine oxide linker ligands (show small ΔE_a and small A) (Figure 3-11c).

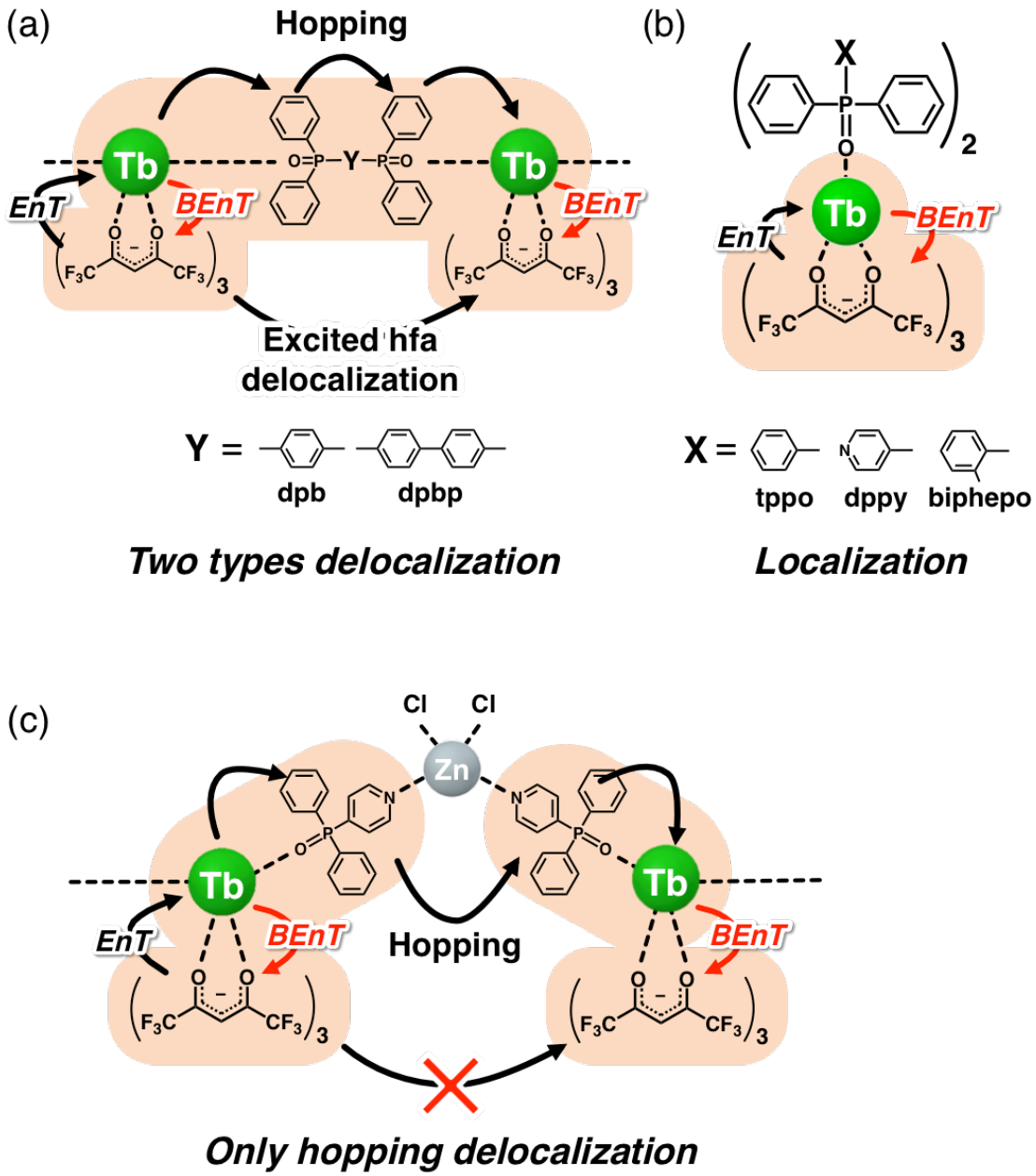

Figure 3-13. (a) Excited energy delocalization image of polynuclear $[Tb(hfa)_3(dpb)]_n$ and $[Tb(hfa)_3(dpbp)]_n$. (b) Excited energy localization image of mononuclear $[Tb(hfa)_3(AEC)]$. (c) Excited energy delocalization image of polynuclear $[Tb(hfa)_3ZnCl_2(dppy)_2]$.

3.4 Conclusion

Introduction of phosphine oxide ligands (Activation Energy Controllers: AECs) to $Tb(hfa)_3$ complexes leads to control of the BEnT process (the ligand-assisted BEnT). From Arrhenius analysis based on the temperature-dependent emission lifetime measurements, the ΔE_a and A values are smaller for the polynuclear $[Tb(hfa)_3(AEC)]_n$ complexes than for the mononuclear $[Tb(hfa)_3(AEC)]$ complexes. In particular, $[Tb(hfa)_3ZnCl_2(dppy)_2]_n$ shows a wider sensing range and larger emission quantum yields than the previous reported chameleon luminophore structure $[Tb_{0.99}Eu_{0.01}(hfa)_3(dpbp)]_n$.[17,36] The phosphorescent lifetimes of the hfa ligands in the Gd^{3+} coordination polymers are longer than those in mononuclear $[Gd(hfa)_3(AEC)]$ complexes. The author considers that the energy hopping of excited Tb^{3+} ions and hfa ligands is introduced by the phosphine oxide linker ligand in polynuclear $[Gd(hfa)_3(AEC)]_n$ complexes. The ΔE_a and A values in the BEnT process are strongly correlated with the excitation lifetimes of the hfa ligands. Introduction of phosphine oxide ligands to $Tb(hfa)_3$ complexes is expected to control the BEnT process. This is the first report of the thermosensing properties of the $Tb(hfa)_3$ complex by ligand-assisted BEnT.

3.5

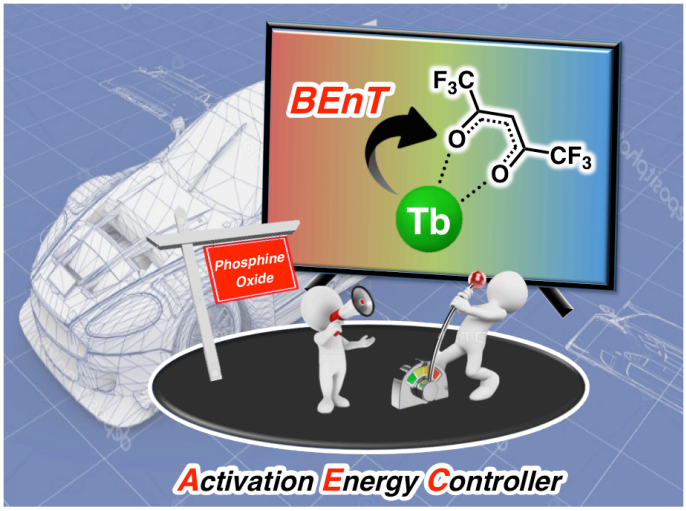

References

[1] X.-D. Wang, O. S. Wolfbeis, R. J. Meier, *Chem. Soc. Rev.,* **2013**, *42*, 7834–7869.

[2] S. Claucherty, H. Sakaue, *Sens. Actuator B.,* **2017**, *251*, 958–962.

[3] V. Ondrus, R. J. Meier, C. Klein, U. Henne, M. Schäferling, U. Beifuss, *Sens. Actuators A,* **2015**, *233*, 434–441.

[4] D. Ross, M. Gaitan, L. E. Locascio, *Anal. Chem.,* **2001**, *73*, 4117–4123.

[5] X. Guan, Z. Su, *Polym. Adv. Technol.,* **2008**, *19*, 385–392.

[6] J. Feng, K. Tian, D. Hu, S. Wang, S. Li, Y. Zeng, Y. Li, G. Yang, *Angew. Chem. Int. Ed.,* **2011**, *50*, 8072–8076.

[7] K. Maruszewski, D. Andrzejewski, W. Strek, *J. Lumin.,* **1997**, *72–74*, 226–228.

[8] L. H. Fischer, C. Karakus, R. J. Meier, N. Risch, O. S. Wolfbeis, E. Holder, M. Schäferling, *Chem. Eur. J.,* **2012**, *18*, 15706–15713.

[9] J. Stehr, J. M. Lupton, M. Reufer, G. Raschke, T. A. Klar, J. Feldmann, *Adv. Mater.,* **2004**, *16*, 2170–2174.

[10] V. A. Vlaskin, N. Janssen, J. van Rijssel, R. M. Beaulac, D. R. Gamelin, *Nano Lett.,* **2010**, *10*, 3670–3674.

[11] R. Liang, R. Tian, W. Shi, Z. Liu, D. Yan, M. Wei, D. G. Evans, X. Duan, *Chem. Commun.* **2013**, *49*, 969–971.

[12] A. Sedlmeier, D. E. Achatz, L. H. Fischer, H. H. Gorris, O. S. Wolfbeis, *Nanoscale*, **2012**, *4*, 7090–7096.

[13] J.-C. G. Bünzli, *Chem. Rev.,* **2010**, *110*, 2729–2755.

[14] M. Mitsuishi, S. Kikuchi, T. Miyashita, Y. Amao, *J. Mater. Chem.,* **2003**, *13*, 2875–2879.

[15] J. H. S. K. Monteiro, F. A. Sigoli, A. de Bettencourt-Dias, *Can. J. Chem.,* **2018**, *96*, 859–864.

[16] S. Katagiri, Y. Hasegawa, Y. Wada, S. Yanagida, *Chem. Lett.,* **2004**, *33*, 1438–1439.

[17] K. Miyata, Y. Konno, T. Nakanishi, A. Kobayashi, M. Kato, K. Fushimi, Y. Hasegawa, *Angew. Chem. Int. Ed.,* **2013**, *52*, 6413–6416.

[18] X. Liu, S. Akerboom, M. de jong, I. Mutikainen, S. Tanase, A. Meijerink, E. Bouwman, *Inorg. Chem.,* **2015**, *54*, 11323–11329.

[19] Z. Wang, D. Ananias, A. Carné-Sánchez, C. D. S. Brites, I. Imaz, D. Maspoch, J. Rocha, L. D. Carlos, *Adv. Funct. Mater.,* **2015**, *25*, 2824–2830.

[20] Y. Cui, H. Xu, Y. Yue, Z. Guo, Z. Chen, J. Gao, Y. Yang, G. Qian, B. Chen, *J. Am. Chem. Soc.,* **2012**, *134*, 3979–3982.

[21] K. Yanagisawa, Y. Kitagawa, T. Nakanishi, T. Seki, K. Fushimi, H. Ito, Y. Hasegawa, *Chem. Eur. J.,* **2018**, *24*, 1956–1961.

[22] C. D. S. Brites, P. P. Lima, N. J. O. Silva, A. Millan, V. S. Amaral, F. Palacio, L. D. Carlos, *Adv. Mater.*, **2010**, *22*, 4499–4504.

[23] M. Latva, H. Takalo, V.-M. Mukkala, C. Matachescu, J. C. Rodriguez-Ubis, J. Kankare, *J. Lumin.,* **1997**, *75*, 149–169.

[24] V. I. Tasryuk, A. V. Vologzhanina, K. P. Zhuravlev, V. A. Kudryshova, *J. Fluorine Chem.,* **2017**, *197*, 87–93.

[25] S. Katagiri, Y. Tsukahara, Y. Hasegawa, Y. Wada, *Bull. Chem. Soc. Jpn.,* 2007, **80**, 1492–1503.

[26] Q. Xu, Z. Li, Y. Wang, H. Li, *Photochem. Photobiol. Sci.,* **2016**, *15*, 405–411.

[27] S. Omagari, T. Nakanishi, T. Seki, Y. Kitagawa, Y. Takahata, K. Fushimi, H. Ito, Y. Hasegawa, *J. Phys. Chem. A,* **2015**, *119*, 1943–1947.

[28] F. Gutierrez, C. Tedeschi, L. Maron, J-.P. Daudey, R. Poteau, J. Azema, P. Tisnes, C. Picard, *Dalton Trans.,* **2004**, *0*, 1334–1347.

[29] Y. Hirai, T. Nakanishi, Y. Kitagawa, K. Fushimi, T. Seki, H. Ito, Y. Hasegawa, *Angew. Chem. Int. Ed.,* **2016**, *55*, 12059–12062.

[30] T. Koizuka, M. Yamamoto, Y. Kitagawa, T. Nakanishi, K. Fushimi, Y. Hasegawa, *Bull. Chem. Soc. Jpn.,* **2017**, *90*, 1287–1292.

[31] S. Omagari, T. Nakanishi, T. Seki, Y. Kitagawa, T. Seki, K. Fushimi, H. Ito, A. Meijerink, Y. Hasegawa, *Sci. Rep.,* **2016**, *6*, 37008-370019.

[32] Y. Hasegawa, Y. Wada, S. Yanagida, *J. Photochem. Photobiol. C,* **2004**, *5*, 183–202.

[33] K. Nakamura, Y. Hasegawa, H. Kawai, N. Yasuda, N. Kanehisa, Y. Kai, T. Nagamura, S. Yanagida, Y. Wada, *J. Phys. Chem. A,* **2007**, *111*, 3029–3037.

[34] M. Yamamoto, T. Nakanishi, Y. Kitagawa, K. Fushimi, Y. Hasegawa, *Mater. Lett.,* **2016**, *167*, 183–187.

[35] K. Miyata, T. Ohba, A. Kobayashi, M. Kato, T. Nakanishi, K. Fushimi, Y. Hasegawa, *ChemPlusChem,* **2012**, *77*, 277–280.

[36] M. Hatanaka, Y. Hirai, Y. Kitagawa, T. Nakanishi, Y. Hasegawa, K. Morokuma, *Chem. Sci.,* **2017**, *8*, 423–429.

Chapter 4

Luminescent lanthanide coordination polymers cross-linked with palladium and aluminum complex ligands

Based on

Synthesis and Photophysical Properties of Eu(III) Complexes with phosphine oxide ligands including metal ions

M. Yamamoto, T. Nakanishi, Y. Kitagawa, T. Seki, H. Ito, K. Fushimi, Y. Hasegawa, *Bulletin of the Chemical Society of Japan*, **2017**, *91*, 6-11.

4.1 Introduction

Three-dimensional building blocks composed of metal ions and organic bridged ligands are called “coordination polymers” or “metal-organic frameworks”. Transition metal-organic frameworks (MOFs) with catalytic and ion-sensing properties have been reported.[1-3] Various types of metalloporphyrin aggregates such as coordination polymers for study of artificial photosynthesis have also been reported.[4-5] Thermostable luminescent coordination polymers with lanthanide ions have been presented for future photonic materials.[6-7] MOFs and metal coordination polymers with characteristic chemical and physical properties can be synthesized by suitable selection of metal ions and bridged organic ligands (Figure 4-1a).

Generally, three-dimensional structures of metal coordination polymers and MOFs are dominated by the coordination number and geometrical structure of the metal ions. The coordination number and geometrical structure in metal coordination polymers are directly linked to their chemical and physical performances for functional molecular materials. Here, the luminescent coordination polymers composed of luminescent and joint metal blocks show in Figure 4-1b. The structural and physical properties of these coordination polymers can be tuned by changing the composition of luminescent and joint metal blocks.

According to the luminescent metal block, the author selected lanthanide complexes with 4*f*-4*f* transitions. The 4*f*-4*f* transitions of lanthanide complexes lead to narrow emission bands (FWHM < 10 nm) and long emission lifetime ($\tau > 1$ μs), resulting in the formation of remarkable luminescent materials for various applications such as

display devices and bio-imaging applications.[8-9] Strong and characteristic luminescence of lanthanide complexes containing Eu^{3+}, Tb^{3+}, Sm^{3+}, Nd^{3+}, Er^{3+}, Yb^{3+} and Pr^{3+} ions have been reported.[10-17] In earlier studies, the luminescent properties of lanthanide complexes were shown to depend on two parameters, radiative and non-radiative rate constants (k_r and k_{nr}).[18, 19] The radiative rate constant depends on the geometrical symmetry of the coordination structure in lanthanide complexes. It has been widely accepted that the radiative transition probability between 4*f* orbitals is enhanced by structures.[18] The non-radiative rate constant is influenced by the vibrational structures of lanthanide complexes. Previously, Hasegawa prepared an Eu^{3+} complex with low-vibrational frequency (LVF) hexafluoroacetylacetonato (hfa) and phosphine oxide ligands. The coordination structure composed of LVF hfa (C-F: 1200 cm^{-1}) and phosphine oxide (P=O: 1125 cm^{-1}) ligands provides a luminescent Eu^{3+} complex with a high emission quantum yield (> 65%) and a relatively small non-radiative rate constant.[20-21]

In order to construct joint metal blocks, the author considered the use of *p*- and *d*-block metal complexes with various coordination structures. The *p*- and *d*-block metal complexes generally provide four, five and six coordination structures.[22-24] Based on the characteristic coordination structures of *p*- and *d*-block metal complexes, one-, two- and three-dimensional networks as a joint metal block are promoted for construction of novel coordination polymer. The author here designed some joint metal blocks composed of metal ions and 4-pyridyldiphenylphosphine oxide (dppy) (Figure 4-1b). The dppy molecule in joint metal blocks possesses a phosphine oxide group,

which plays an important role in effective connection with luminescent lanthanide blocks such as an LVF phosphine oxide. The pyridyl group in dppy is linked to the *p*- and *d*-block metal ions for formation of joint metal blocks. By using dppy molecules, Pd^{2+} complexes [*trans*-$PdCl_2(dppy)_2$], Zn^{2+} complexes [$ZnCl_2(dppy)_2$], and Al^{3+} complexes [$AlCl_3(dppy)_4$] were prepared as joint metal blocks.

In this chapter, $[Eu(hfa)_3(dppy)_2PdCl_2]_n$ (Eu-Pd) and $[Eu(hfa)_3(dppy)_4AlCl_3]_n$ (Eu-Al) are prepared. The author focuses on the heavy element such as Pd^{2+} ions, and the light element, Al^{3+} ions, which have higher coordination number than that of Zn^{2+} ions. The effects to photphysical properties of these Eu^{3+} coordination polymers by using different metal ions were reported. The predicted structures were estimated by single-crystal X-ray structural analyses and DFT calculations. Photophysical properties were evaluated based on the emission lifetimes and emission quantum yields. The preparation, structures and photophysical properties of new Eu^{3+} coordination polymers linked with joint metal blocks are described.

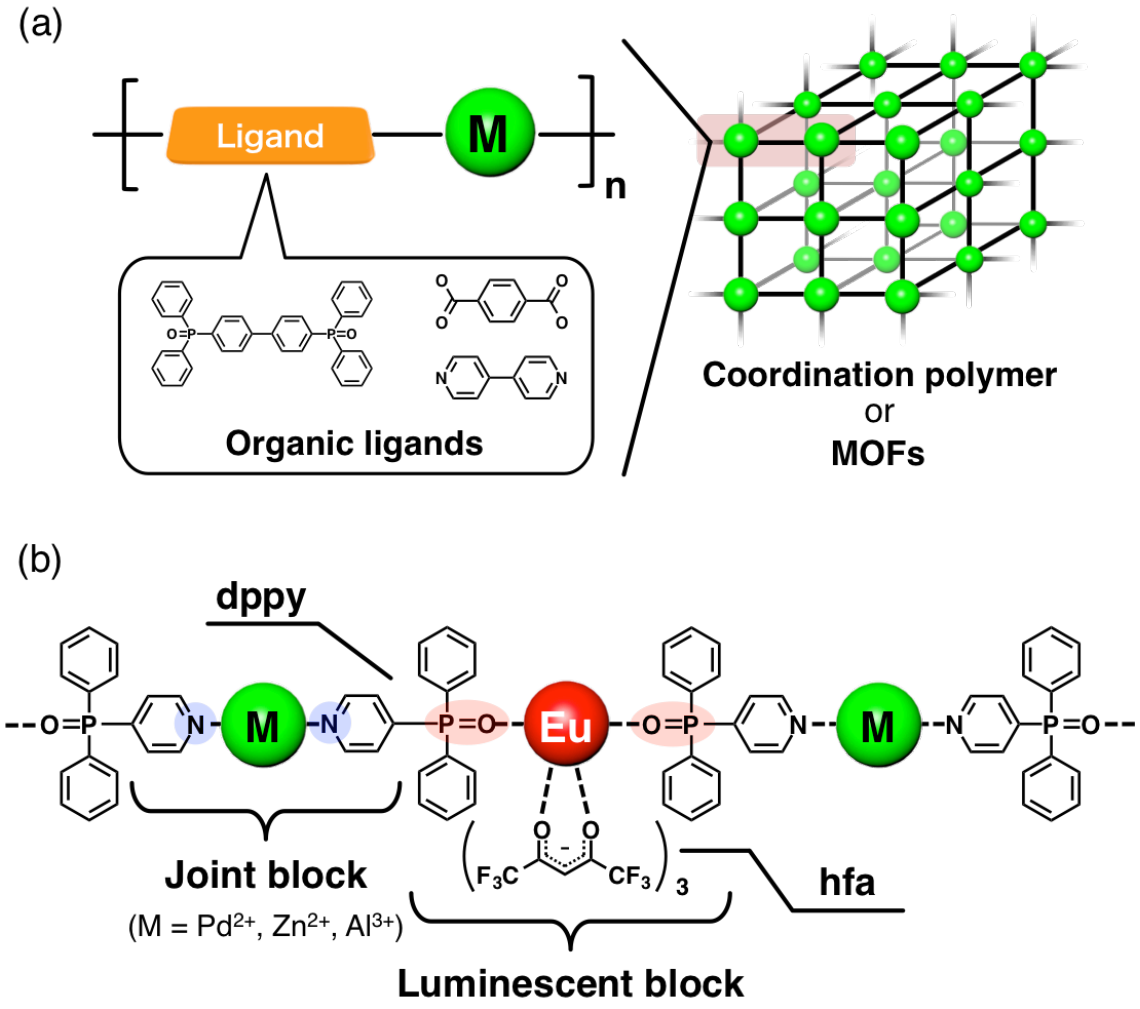

Figure 4-1. (a) General images of coordination polymers or MOFs. (b) Structural image of Eu^{3+} coordination polymer (M = Pd^{2+}, Zn^{2+} and Al^{3+}).

4.2 Experimental section

Materials

4-Bromopyridine hydrochloride (98%), tetrakis(triphenylphosphine)palladium (97%), diphenylphosphine (90%) and hexafluoroacetylacetone (95%) were purchased from Tokyo Chemical Industry Co., Ltd. Europium(III) acetate *n*-hydrate (99.9%), palladium(II) chloride(98%), zinc(II) chloride (99.9%) and aluminum(III) chloride (99%) were obtained from Wako Pure Chemical Industries, Ltd. All chemicals were reagent grade and were used without further purification.

Apparatuses

^{1}H NMR spectra were recorded on a JEOL JNM-ECS400 (400 MHz). ^{1}H NMR chemical shifts were determined by tetramethylsilane (TMS) as an internal standard. Elemental analyses were performed using a J-SCIENCE MICRO CORDER JM10. ESI-MS and FAB-MS were performed using a JEOL JMS-T100LP and a JEOL JMS-700TZ, respectively.

Preparation of 4-pyridyl diphenyl phosphine oxide (dppy) $C_{17}H_{14}NOP$

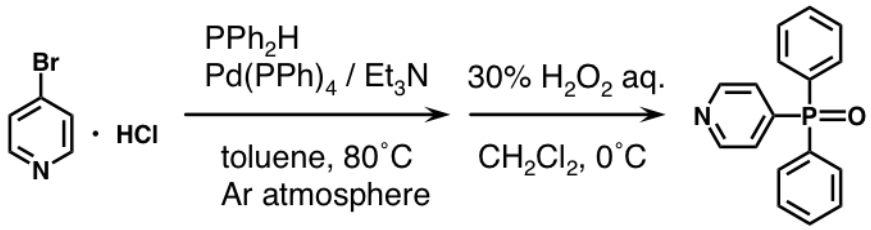

The dppy ligand was prepared according to chapter 2.2.[25]

^{1}H NMR (400 MHz, $CDCl_3$ / TMS) : δ8.74-8.79 (t, 2H, py), 7.48-7.71 (m, 12H, Ar)ppm. ESI-MS calcd. for $[M + H]^+$: 280.09 Found, 280.09. Elemental analysis calcd. (%) for $C_{17}H_{14}NOP$: C 73.11, H 5.05, N 5.02; found: C 73.03, H 5.07, N 4.95.

Preparation of Pd^{2+} complex [trans-$PdCl_2(dppy)_2$] $C_{34}H_{28}Cl_2N_2O_8P_2Pd$

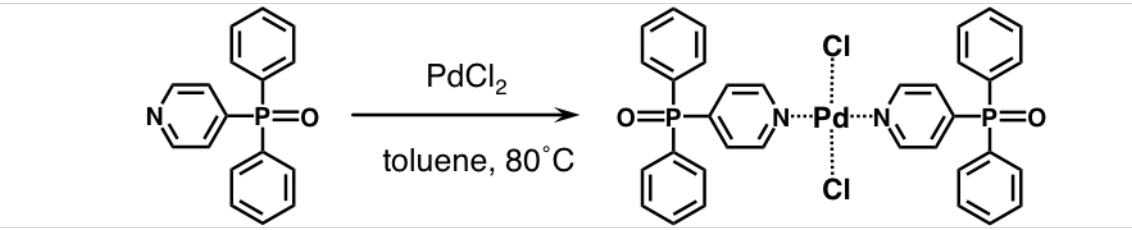

Palladium(II) chloride (88.6 mg, 0.50 mmol) and 4-pyridyl diphenyl phosphine oxide (0.28 g, 1.00 mmol) were dissolved in toluene (40 mL). The solution was heated at 100˚C and refluxed while stirring for 48 h. The solvent was evaporated to afford a yellow powder. Recrystallization from methanol gave yellow crystals of the titled compound. (0.27 g, 72%) ^{1}H NMR (400 MHz, $CDCl_3$ / TMS) : δ8.92-8.97 (t, 4H, py), 7.49-7.68 (m, 24H, Ar)ppm. ESI-MS calcd. for $[M + Cl]^+$: 770.97 Found, 770.94. Elemental analysis calcd. (%) for $C_{34}H_{28}Cl_2N_2O_8P_2Pd+CH_3OH$: C 54.74, H 4.20, N 3.65; found: C 54.62, H 3.84, N 3.77.

Preparation of Zn^{2+} complex $[ZnCl_2(dppy)_2]$ $C_{34}H_{28}Cl_2N_2O_2P_2Zn$

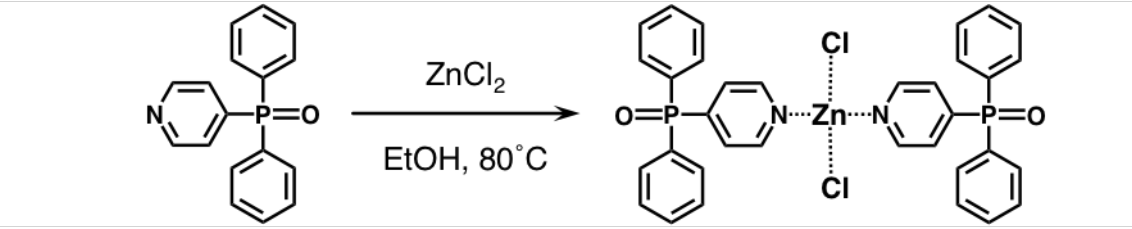

The Zn^{2+} complex ligand $[ZnCl_2(dppy)_2]$ was prepared according to chapter 2.2. [25]

^1H NMR (400 MHz, $CDCl_3$ / TMS) : δ8.84-8.89 (t, 4H, py), 7.71-7.77 (d, 4H, py), 7.62-7.70 (m, 12H, Ar), 7.50-7.57 (m, 8H, Ar)ppm. ESI-MS calcd. for $[ZnCl(dppy)_2]^-$: 692.03 Found, 692.03. Elemental analysis calcd. (%) for $C_{34}H_{28}Cl_2N_2O_2P_2Zn$: C 58.77, H 4.06, N 4.03; found: C 59.27, H 4.31, N 3.73.

Preparation of Al^{3+}complex $[AlCl_3(dppy)_4]$ $C_{68}H_{56}Cl_3N_4O_4P_4Al$

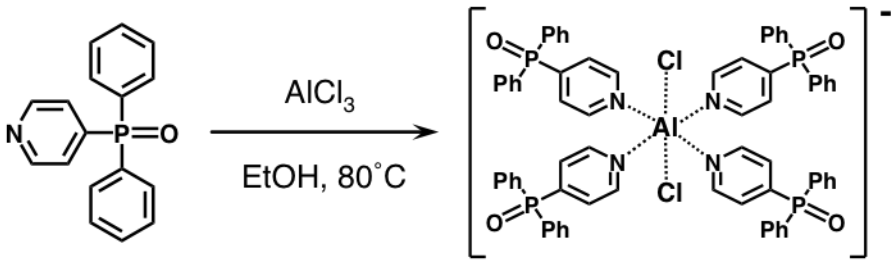

Aluminum(III) chloride (74.4 mg, 0.56 mmol) and 4-pyridyl diphenyl phosphine oxide (0.50 g, 1.81 mmol) were dissolved in chloroform (40 mL). The solution was heated at 60˚C and refluxed while stirring for 24 h. The solvent was evaporated to afford a withe powder of the titled compound. (91.0 mg, 13%) ^1H NMR (400 MHz, MeOD / TMS) : δ8.84-8.89 (t, 8H, py), 7.89-7.96 (d, 8H, py), 7.68-7.76 (m, 24H, py), 7.58-7.65 (m, 16H, Ar)ppm. ESI-MS calcd. for $[AlCl_3(dppy)_4 \cdot 5H_2O + H]^+$: 1339.27 Found, 1339.16.

Preparation of Eu-Pd complex $[Eu(hfa)_3(dppy)_2PdCl_2]_n$ $C_{49}H_{31}Cl_2EuF_{18}N_2O_8P_2Pd$

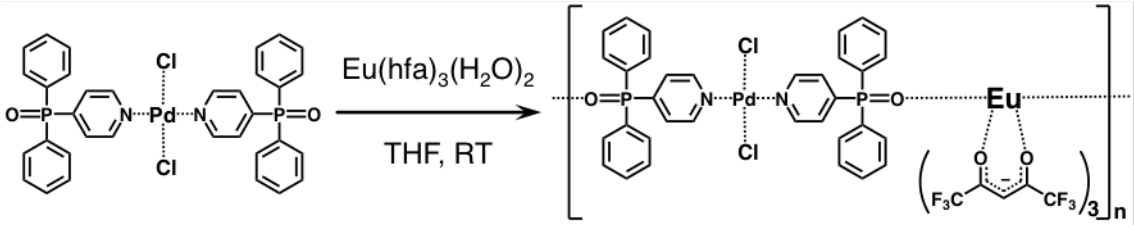

Pd^{2+} complex [*trans*-$PdCl_2(dppy)_2$] (1 equiv.) and $[Eu(hfa)_3(H_2O)_2]$ (1 equiv.) were dissolved in THF. The solution was refluxed while stirring for 5 h, and the reaction mixture was concentrated to dryness. A single crystal suitable for X-ray structural determination of Eu-Pd complex was obtained by diffusion method of methanol-chloroform solution at room temperature. FAB-MS calcd. for $[Eu(hfa)_3(dppy)PdCl_2]^+$: 1300.90 Found, 1300.9. Elemental analysis calcd (%) for $C_{49}H_{31}Cl_2EuF_{18}N_2O_8P_2Pd$: C 39.00, H 2.07, N 1.86, Cl 4.70; found: C 38.83, H 2.41, N 1.80, Cl 4.73.

Preparation of Eu-Zn complex $[Eu(hfa)_3(dppy)_2ZnCl_2]_n$ $C_{49}H_{31}Cl_2EuF_{18}N_2O_8P_2Zn$

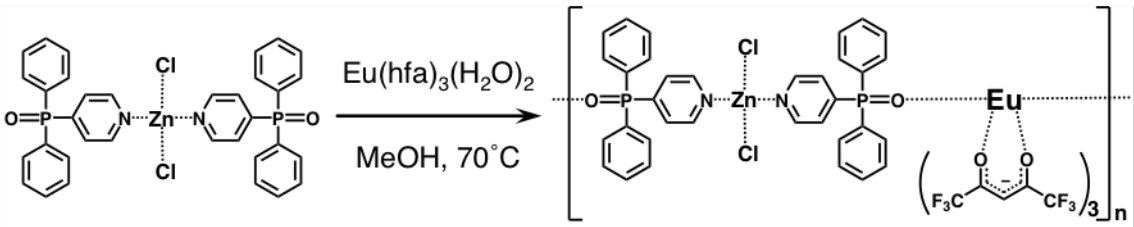

The $[Eu(hfa)_3ZnCl_2(dppy)_2]_n$ was prepared according to chapter 2.2.

FAB-MS calcd. for $[Eu(hfa)_3(dppy)ZnCl_2]^+$: 1258.93 Found, 1259.9. Elemental analysis calcd (%) for $C_{49}H_{31}Cl_2EuF_{18}N_2O_2P_2Zn+2H_2O$: C 39.13, H 2.35, N 1.86; found: C 38.73, H 2.25, N 1.88.

Preparation of Eu-Al complex $[Eu(hfa)_3(dppy)_4AlCl_3]_n$ $C_{83}H_{59}Cl_3EuF_{18}N_4O_{10}P_4Al$

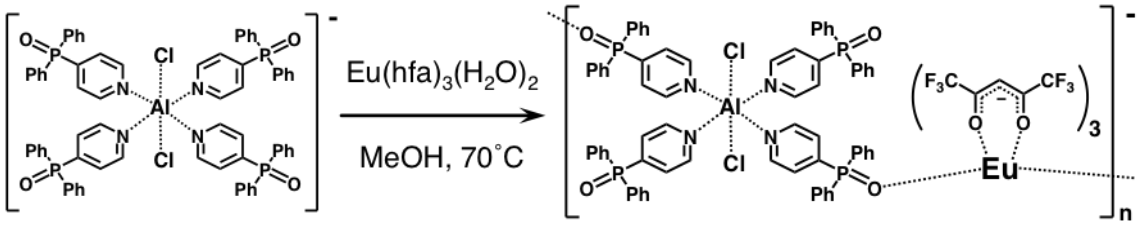

Al^{3+} complex $[AlCl_3(dppy)_4]$ (1 equiv.) and $[Eu(hfa)_3(H_2O)_2]$ (2 equiv.) were dissolved in methanol. The solution was refluxed while stirring for 5 h, and the reaction mixture was concentrated to dryness. ^1H NMR (400 MHz, $CDCl_3$ / TMS) : δ8.91-8.73 (br, 8H, py), 8.10-7.36 (br, 48H, Ar), 5.05 (s, 3H, hfa-H)ppm. FAB-MS calcd. for $[Eu(hfa)_2(dppy)_4AlCl_2]^+$: 1952.16 Found, 1952.5.

Computational details

Density functional theory (DFT) geometry optimizations of joint Zn^{2+} block $[ZnCl_2(dppy)_2]$ and joint Al^{3+} block $[AlCl_3(dppy)_4]$ were carried out with Gaussian09 Rev D.01 by employing the three-parameter hybrid functional of Becke based on the correlation functional of Lee, Yang, and Parr (B3LYP).[26,27] The 6-31G(d) basis set was used for all other atoms.

Crystallography

Colorless single crystals of Eu^{3+} and Pd^{2+} complex were mounted on the MiTeGen micromesh using paraffin oil. All measurements were made by using a Rigaku RAXIS

RAPID imaging-plate area detector with graphite-monochromated Mo-Kα radiation. Non-hydrogen atoms were refined anisotropically. All calculations were performed by using the crystal-structure crystallographic software package. CIF data was confirmed by using the checkCIF/PLATON service. CCDC-1507442 for $[Eu(hfa)_3(dppy)_2]$ and CCDC-1510581 for [*trans*-$PdCl_2(dppy)_2$] contain the supplementary crystallographic data for this chapter. These data can be obtained free of charge from The Cambridge Crystallographic Data Centre via www.ccdc.cam.ac.uk/data_request/cif.

Optical measurements

Emission and excitation spectra of Eu^{3+} complexes were measured with a HORIBA Fluorolog-3 spectrofluorometer and corrected for the response of the detector system. Emission lifetimes (τ_{obs}) of Eu^{3+} complexes were measured using the third harmonics (355 nm) of a Q-switched Nd:YAG laser (Spectra Physics, INDI-50, FWHM = 5 ns, λ = 1064 nm) and a photomultiplier (Hamamatsu Photonics, R5108, response time ≤ 1.1 ns). The Nd:YAG laser response was monitored with a digital oscilloscope (Sony Tektronix, TDS3052, 500 MHz) synchronized to the single-pulse excitation. Emission lifetimes were determined from the slope of logarithmic plots of the decay profiles.

4.3 Results and discussion

4.3.1 Structural analyses

The 4-pyridyldiphenylphosphine oxide (dppy) contains selective coordination sites for lanthanide ions (P=O) and metal ions (N atoms). The dppy was synthesized by the coupling reaction of 4-bromopyridine hydrochloride with diphenylphosphine and Pd^0 complex as a catalyst, and then oxidized using hydrogen peroxide. Joint metal blocks were prepared by the complexation of metal chlorides (palladium, zinc and aluminum chlorides) with dppy in an organic solvent under a reflux condition. Finally, $[Eu(hfa)_3(dppy)_2PdCl_2]_n$ (Eu-Pd), $[Eu(hfa)_3(dppy)_2ZnCl_2]_n$ (Eu-Zn) and $[Eu(hfa)_3(dppy)_4AlCl_3]_n$ (Eu-Al) were prepared by the complexation of $[Eu(hfa)_3(H_2O)_2]$ with a *p*- or *d*-metal joint block. The chemical structures were confirmed by MS (ESI- and FAB-MS) and elemental analyses. Single crystals of $[Eu(hfa)_3(dppy)_2]$ and [*trans*-$PdCl_2(dppy)_2$] for X-ray structural analyses were successfully prepared by recrystallization from solutions in diethyl ether/hexane and methanol, respectively. However, single crystals of Eu-Zn and Eu-Al were not obtained. The structures of $[ZnCl_2(dppy)_2]$ and $[AlCl_3(dppy)_4]$ were estimated using DFT calculation (B3LYP/6-31G(d)) based on previous X-ray crystal data for a pyridyl metal complex derivative. [28, 29]

Structural images and crystal data of $[Eu(hfa)_3(dppy)_2]$ and $[Eu(hfa)_3PdCl_2(dppy)_2]_n$ are shown in Figure 4-2, 4-3 and Table 4-1, respectively. From the result of single-crystal X-ray diffraction, the coordination site of the luminescent Eu^{3+} block $[Eu(hfa)_3(dppy)_2]$ is comprised of three hexafluoroacetylacetonato (hfa) ligands

and two phosphine oxide (dppy) ligands (Figure 4-2). The calculation of the shape measure factor *S* to estimate the degree of distortion of the coordination structure in the Eu^{3+} coordination sphere was carried out. The *S* value is given by Equation (1):

$$S = \min \sqrt{\left(\frac{1}{m}\right)\sum_{i=1}^{m}(\delta_i - \theta_i)^2} \ , \qquad 1$$

where m , δ_i , and θ_i are the number of possible edges (m = 18 in this chapter), the observed dihedral angle between planes along the *i* th edge, and the dihedral angle for the ideal structure, respectively. According to the crystals data of $[Eu(hfa)_3(dppy)_2]$, the *S* values for 8-SAP (point group D_{4d} , S = 7.92) are smaller than those for 8-TDH (point group D_{2d} , S = 9.37), suggesting that the 8-SAP structure is less distorted than the 8-TDH structure in the systems. The *S* values of around Eu^{3+} ions in $[Eu(hfa)_3PdCl_2(dppy)_2]_n$ were estimated to be 4.41 for 8-SAP and 11.0 for 8-TDH. Thus, coordination geometries of $[Eu(hfa)_3(dppy)_2]$ and $[Eu(hfa)_3PdCl_2(dppy)_2]_n$ were determined to be 8-SAP like structures (see Table 4-2 and 4-3).

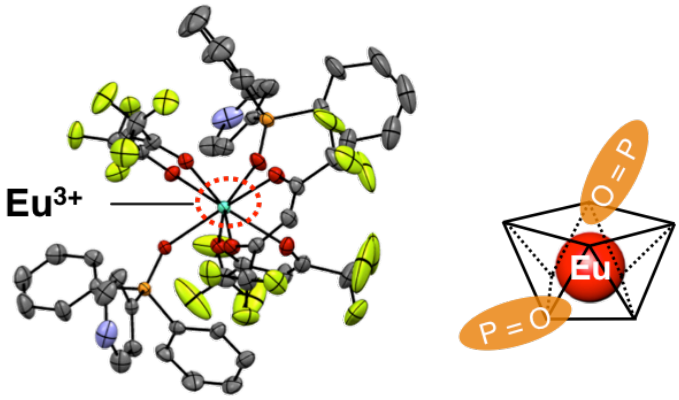

Figure 4-2. ORTEP views of $[Eu(hfa)_3(dppy)_2]$, showing 50% probability displacement ellipsoids. Hydrogen atoms have been omitted for clarity. Green: Tb, red: O, gray: C, yellow: F, and orange: P.

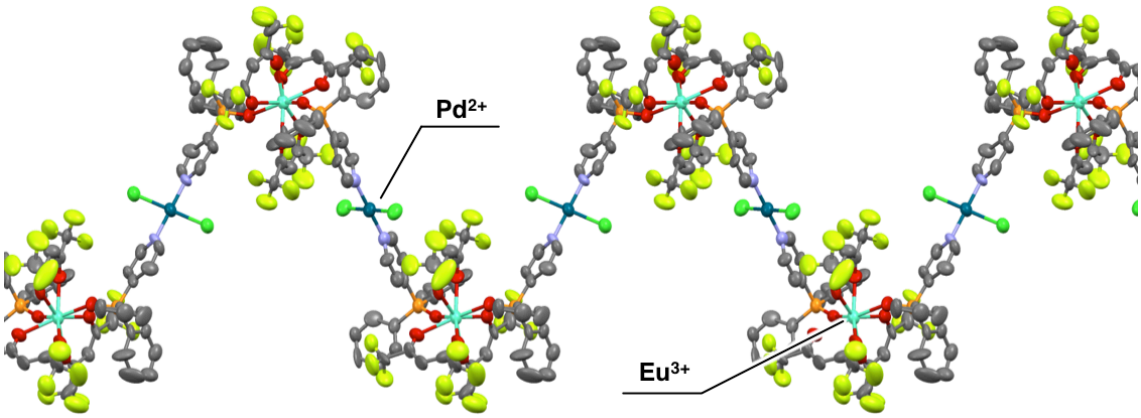

Figure 4-3. ORTEP view of Eu-Pd coordination polymer: $[Eu(hfa)_3PdCl_2(dppy)_2]_n$.

Table 4-1. Crystal data of luminescent Eu^{3+} block: $[Eu(hfa)_3(dppy)_2]$, joint Pd^{2+} block: $[PdCl_2(dppy)_2]$ and Eu-Pd programming polymer.

	$[Eu(hfa)_3(dppy)_2]$	$[PdCl_2(dppy)_2]$	Eu-Pd
chemical formula	$C_{49}H_{31}EuF_{18}N_2O_8P_2$	$C_{34}H_{28}Cl_2N_2O_2P_2Pd$ (CH_4O)	$C_{49}H_{31}Cl_{12}EuF_{18}N_2$ O_8P_2Pd
formula weight	1331.67	799.91	1508.97
crystal color, habit	colorless, block	yellow, needle	yellow, needle
crystal system	triclinic	monoclinic	triclinic
space group	P -1	P 21/c	P -1
a / Å	13.0614(9)	18.4663(15)	10.702(4)
b / Å	13.6957(9)	7.0606(6)	12.815(5)
c / Å	15.4953(10)	14.4406(12)	22.546(8)
α / deg	76.172(2)	90	82.583(9)
β / deg	83.696(2)	104.342(2)	77.775(11)
γ / deg	78.579(2)	90	76.235(11)
V / Å	2632.6(3)	1824.1(3)	2925.1(19)
Z	2	2	2
d_{calc} / g cm^{-3}	1.680	1.456	1.810
T / ˚C	123	123	123
μ(Mo Kα) / cm^{-1}	13.70	7.83	17.17
Max 2θ / deg	27.485	27.484	27.490
measured reflections	33479	10885	5462
Unique reflections	12000	4167	12976
R $(I > 2\sigma(I))$ [a)]	0.0362	0.0576	0.1656
R_w $(I > 2\sigma(I))$ [b)]	0.1246	0.1820	0.4008

a) $R = \Sigma||F_o| - |F_c|| / \Sigma|F_o|$.

b) $R_w = [\Sigma w(|F_o| - |F_c|)^2 / \Sigma wF_o^2]^{1/2}$.

Table 4-2. Observed dihedral angles (δ_i), dihedral angles of idealized square antiprism (θ_i) and measure shape criteria, S (D_{4d}) for $Tb(hfa)_3(tppo)_2$, $[Tb(hfa)_3(dpb)]_n$ and $[Tb(hfa)_3(dpbp)]_n$.

	[Eu(hfa)$_3$(dppy)$_2$]			Eu-Pd		
Edge	θ_i	δ_i	$\delta_i - \theta_i$	θ_i	δ_i	$\delta_i - \theta_i$
O1-O2	0	22.02	22.02	0	11.22	11.22
O6-O7	77.1	67.78	-9.32	77.1	79.67	2.57
O1-O3	77.1	72.23	-4.87	77.1	75.59	-1.51
O1-O4	77.1	67.53	-9.57	77.1	72.90	-4.20
O2-O3	77.1	68.1	-9	77.1	80.22	3.12
O2-O4	0	1.46	1.46	0	3.73	3.73
O6-O5	77.1	72.37	-4.73	77.1	74.59	-2.51
O6-O8	77.1	81.69	4.59	77.1	76.49	-0.61
O7-O8	77.1	72.33	-4.77	77.1	76.23	-0.87
O7-O5	77.1	83.23	6.13	77.1	81.29	4.19
O5-O2	51.6	45.05	-6.55	51.6	46.86	-4.74
O5-O4	51.6	59.2	7.6	51.6	57.10	5.5
O6-O1	51.6	47.63	-3.97	51.6	47.28	-4.32
O6-O4	51.6	52.73	1.13	51.6	52.66	1.06
O8-O1	51.6	46.95	-4.65	51.6	49.33	-2.27
O8-O3	51.6	60.39	8.79	51.6	59.83	8.23
O7-O2	51.6	47.3	-4.3	51.6	51.18	-0.42
O7-O3	51.6	56.15	4.55	51.6	49.90	-1.70
	$S(D_{4d}) = 7.92$			$S(D_{4d}) = 4.41$		

Table 4-3. Observed dihedral angles (δ_i), dihedral angles of idealized trigonal dodecahedron (θ_i) and measure shape criteria, S (D_{2d}) for $Tb(hfa)_3(tppo)_2$, $[Tb(hfa)_3(dpb)]_n$ and $[Tb(hfa)_3(dpbp)]_n$.

	[Eu(hfa)$_3$(dppy)$_2$]			Eu-Pd		
Edge	θ_i	δ_i	$\delta_i - \theta_i$	θ_i	δ_i	$\delta_i - \theta_i$
O1-O2	29.86	22.02	22.02	29.86	11.22	-18.64
O6-O7	61.48	67.78	-9.32	61.48	79.67	18.19
O1-O3	74.29	72.23	-4.87	74.29	75.59	1.3
O1-O4	74.29	67.53	-9.57	74.29	72.9	-1.39
O2-O3	61.48	68.1	-9	61.48	80.22	18.74
O2-O4	29.86	1.46	1.46	29.86	3.73	-26.13
O6-O5	61.48	72.37	-4.73	61.48	74.59	13.11
O6-O8	74.29	81.69	4.59	74.29	76.49	2.2
O7-O8	76.62	72.33	-4.77	76.62	76.23	-0.39
O7-O5	74.84	83.23	6.13	74.84	81.29	6.45
O5-O2	54.51	45.05	-6.55	54.51	46.86	-7.65
O5-O4	48.09	59.2	7.6	48.09	57.1	9.01
O6-O1	47.76	47.63	-3.97	47.76	47.28	-0.48
O6-O4	54.48	52.73	1.13	54.48	52.66	-1.82
O8-O1	52.57	46.95	-4.65	52.57	49.33	-3.24
O8-O3	52.85	60.39	8.79	52.85	59.83	6.98
O7-O2	47.34	47.3	-4.3	47.34	51.18	3.84
O7-O3	52.63	56.15	4.55	52.63	49.9	-2.73
	$S(D_{2d}) = 9.37$			$S(D_{2d}) = 11.0$		

From the result of single-crystal X-ray diffraction, the coordination site of the joint Pd^{2+} block [*trans*-$PdCl_2(dppy)_2$] is composed of two chloride ions and two phosphine oxide ligands (Figure 4-4a). The Pd^{2+} complex shows four planar coordination structures without structural distortion, being similar to those of a previously reported Pd^{2+} complex.[30] The result of structural analysis was determined that the structure of Pd complex was formed trans-isomer.

According to Zn^{2+} complex with pyridyl group, Englert and co-workers have reported [$ZnCl_2(3,5\text{-}Me_2py)_2$] (3,5-$Me_2$py: 3,5-dimethylpyridine) with tetrahedral structure.[28] The structure of joint Zn^{2+} block was estimated by DFT calculation based on the previous X-ray single crystal data. The results of DFT calculation showed that the joint Zn^{2+} block was also composed of chloride ions and phosphine oxide ligands (Figure 4-4b). The coordination geometry of the joint Zn^{2+} block provides a tetrahedral structure.

Kemniz and co-workers have also described octahedral Al^{3+} complex [$AlBr_3(py)_4$] (py: pyridine). They also reported that the counter anion of bromide ion existed around Al^{3+} complex. [29] These results suggested that the counter anion of chloride ion existed around joint Al^{3+} block. Thus, the structural optimization of the joint Al^{3+} block was evaluated by DFT calculation based on the $[AlCl_2(dppy)_4]^+$. The joint Al^{3+} block shows an octahedral structure with three chloride ions and four phosphine oxide ligands (Figure 4-4c).

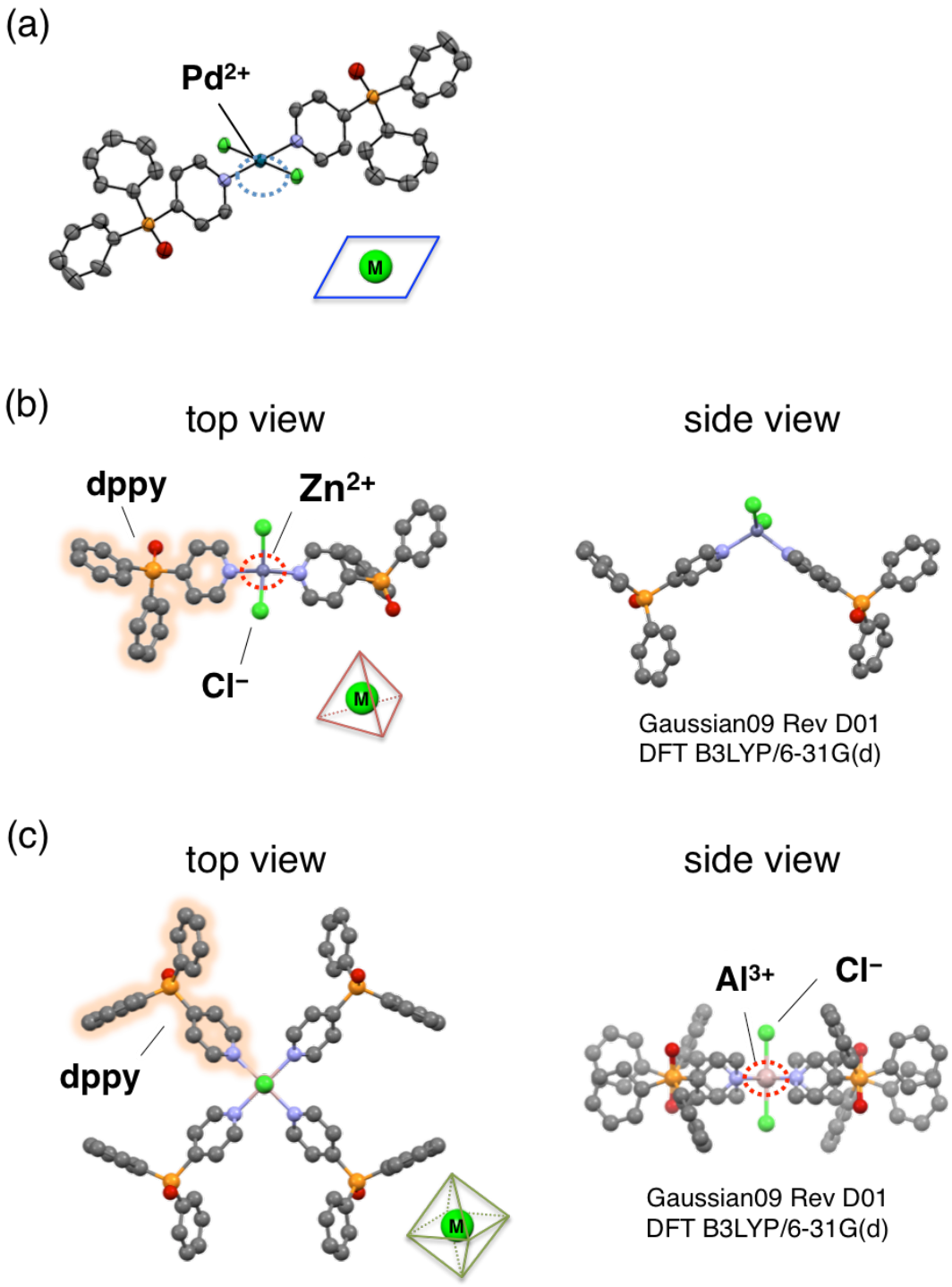

Figure 4-4. Structures of joint metal blocks, (a) ORTEP views of joint Pd^{2+} block: [*trans*-$PdCl_2(dppy)_2$]. Structure optimizations of (b) joint Zn^{2+} block: [$ZnCl_2(dppy)_2$] and (c) joint Al^{3+} block: [$AlCl_3(dppy)_4$] using DFT calculations.

The joint Zn^{2+} block in Eu-Zn is formed tetrahedral structure with two chloride ions and two phosphine oxide ligands, resulting in the formation of a one- dimensional Eu-Zn polymer structure. The ESI-MS fragment of Eu-Zn ($[Eu(hfa)_2(dppy)_2ZnCl_2]^+$) is similar to that of the one-dimensional structure of Eu-Pd ($[Eu(hfa)_2(dppy)_2ZnCl_2]^+$).

From these findings, Eu-Zn polymer is formed the one-dimensional structure. On the other hand, the joint Al^{3+} blocks in Eu-Al seems to be constructed with an octahedral structure by two chloride ions and four phosphane oxide ligands. The Eu-Al polymer is shown the three-dimensional network structure. From these findings, the author considered that Eu-Pd, Eu-Zn and Eu-Al complexe were formed a one-dimensional network structure (Figure 4-5).

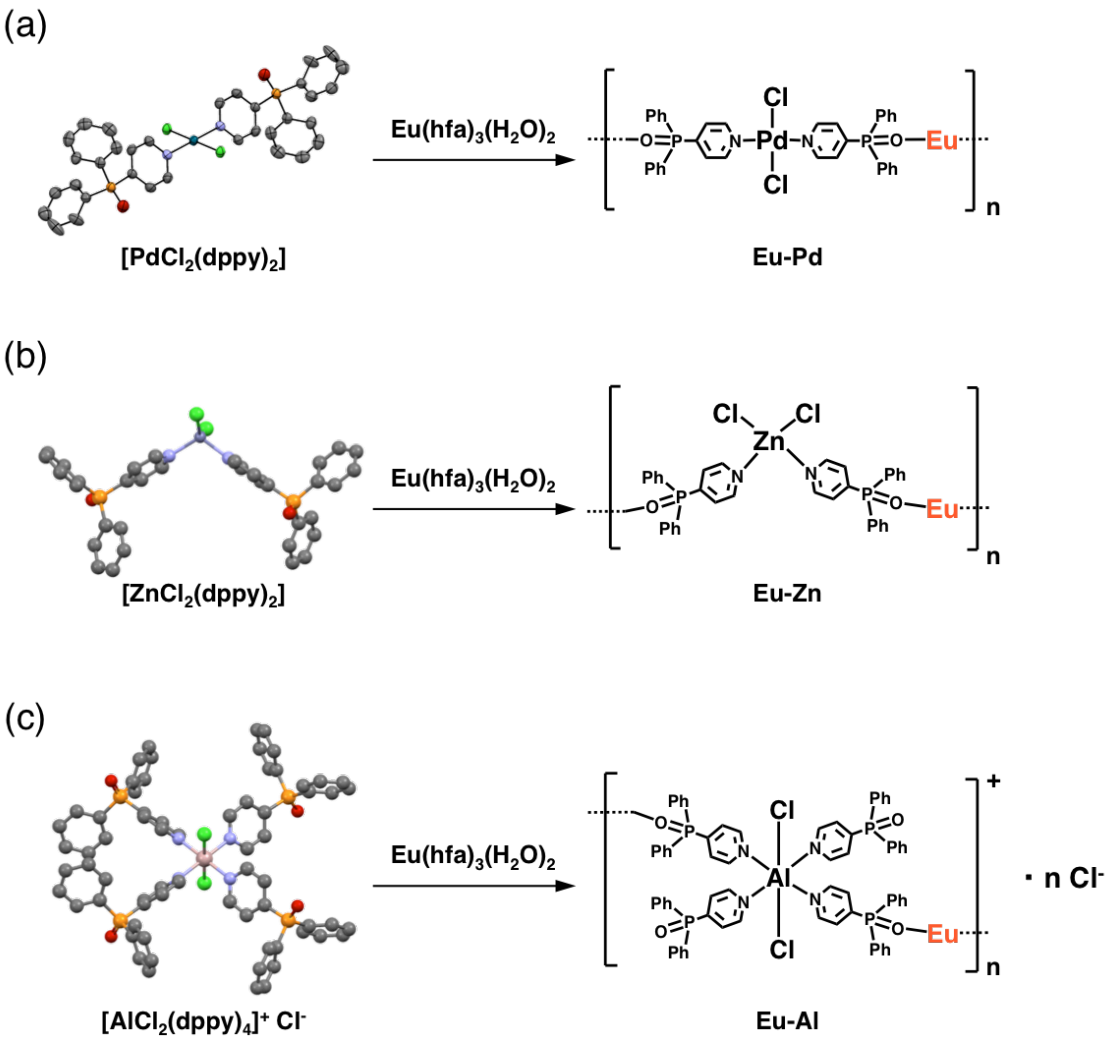

Figure 4-5. Estimated polymer structures of Eu^{3+} complexes: (a) Eu-Pd, (b) Eu-Zn and (c) Eu-Al.

4.3.2 Photophysical properties

The emission spectra for Eu-Al and Eu-Pd complex in a solid state are shown in Figure 4-6a. Emission bands were observed at around 578, 592, 613, 650, and 698 nm, and they are attributed to 4*f*– 4*f* transitions of Eu^{3+} ($^5D_0 \rightarrow {}^7F_J$: J = 0, 1, 2, 3, and 4), respectively. The spectra were normalized with respect to the magnetic dipole transition intensities (MD) at 592 nm ($^5D_0$–$^7F_1$), which are insensitive to the surrounding environment of the Eu^{3+} ions. The emission bands at around 613 nm are due to the electric dipole (ED) transitions, which are strongly dependent on the coordination geometry.[18] The spectral shapes of emission bands at around 613 nm of Eu-Al and Eu-Pd complex are related to their coordination geometry. The ED transition intensity of Eu-Al is larger than those of Eu-Pd. The large ED transition intensity is linked to the asymmetric structure of Eu-Al and enhanced k_r constant.

Emission lifetimes observed from the $^5D_0$ excited level (τ_{obs}) were determined from the slope of the logarithmic decay profiles (Figure 4-6b). The time-resolved emission profile of Eu-Al shows a single exponential decay with millisecond-scale lifetime. The emission lifetime for Eu-Al was determined to be 0.80 ms. In contrast, the time-resolved emission profile of Eu-Pd also shows a single exponential decay with microsecond-scale lifetime. The emission lifetime for Eu-Pd was determined to be 22 μs.

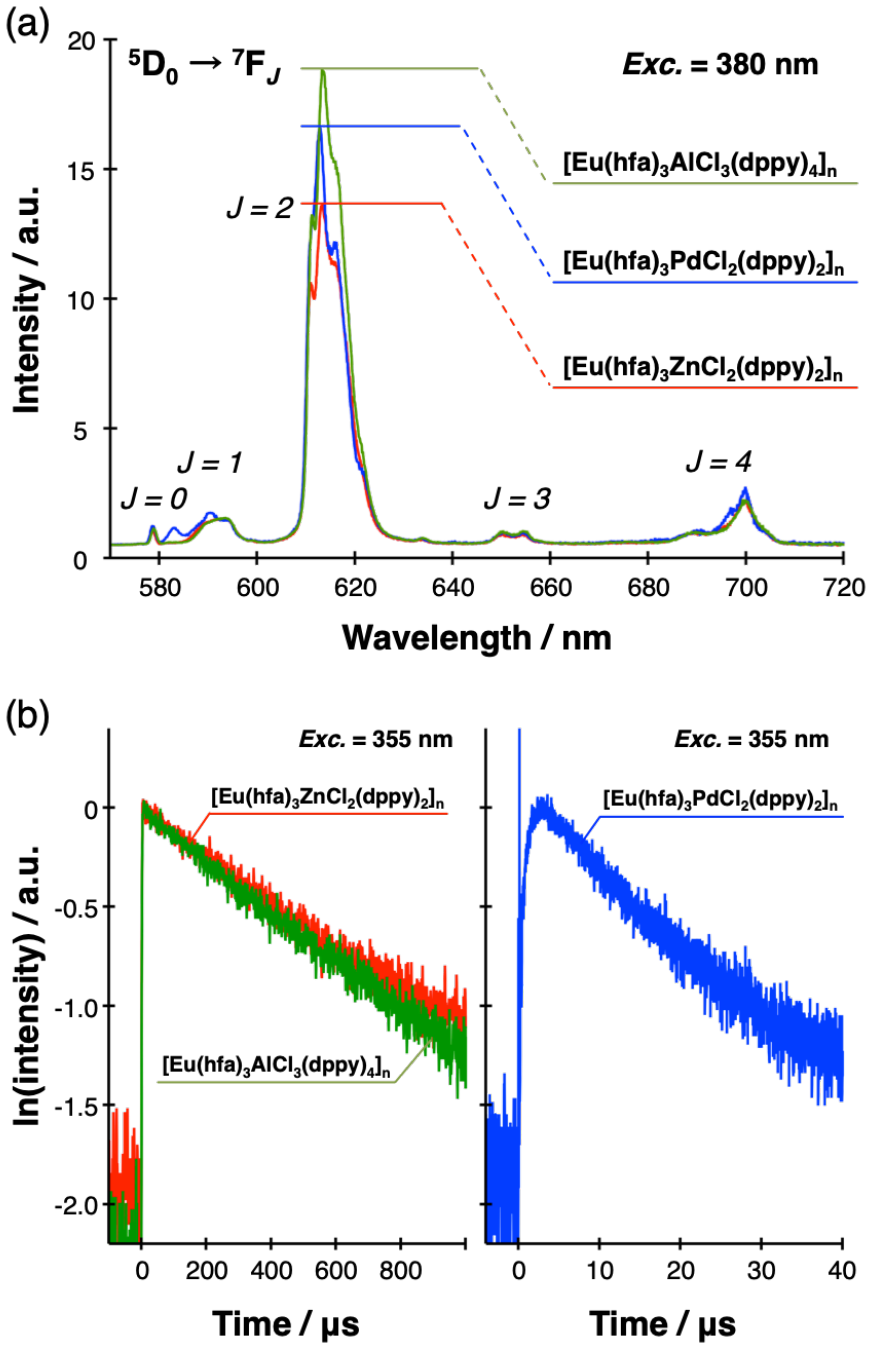

Figure 4-6. (a) Emission spectra of Eu^{3+} complexes in solid state at room temperature excited at 350 nm. (b) Emission lifetime decays of Eu^{3+} complexes (left: Eu-Zn and Eu-Al, right: Eu-Pd) in solid state at room temperature excited at 355nm and detected at 610 nm.

The values of k_r, k_{nr}, and Φ_{ff} were calculated using τ_{obs} and emission spectra by the following equations. [31-33] The photophysical properties of Eu^{3+} complexes linked with joint metal blocks are summarized in Table 4-4. The emission quantum yield of Eu-Al and Eu-Pd were estimated to be 72 and 1.3%, respectively. The Eu-Al complex shows a large emission quantum yield (Φ_{ff} = 72%), which is based on the large k_r and small k_{nr}. The large k_r of Eu-Al is most likely caused by the enhancement of the ED transition based on the asymmetric coordination geometry. In the previous study, Hasegawa found that the radiative rate constant k_r of luminescent Eu^{3+} complexes was enhanced by the asymmetric coordination geometry with various types of phosphine ligands, and these Stark splitting in emission spectra are dependent on the sterical structures of lanthanide complexes with phosphine ligands.[21] It should be noted that the coordination site of Eu^{3+} ions of Eu-Al, Eu-Zn, and Eu-Pd are similar structure, which are comprised of three hfa ligands and two dppy ligands. Thus, the radiative rate constants k_r of these Eu^{3+} complexes were expected to be similar value. The value of k_r in Eu-Al is larger than that of Eu-Pd, although the Stark splitting shape of Eu-Al is similar to that of Eu-Pd (see Figure 4-6a). From these photophysical findings, large k_r of Eu-Al seems to be affected by not only the asymmetric coordination geometry but also electronic structure of joint Al^{3+} parts. The small k_{nr} of Eu-Al is probably caused by the rigid three-dimensional network structure.The small k_{nr} of Eu-Al is probably caused by the rigid network structure. The emission quantum yield of Eu-Al is larger than those of Eu-Zn and Eu-Pd complex.

The photo-sensitized energy transfer efficiency η_{sens} is also calculated based

on the Φ_{ff} and $\Phi_{\pi\pi^*}$. In Table 4-4, η_{sens} of Eu-Al (η_{sens} = 72%) is much larger than those of Eu-Zn (η_{sens} = 48%). The η_{sens} of Eu-Al is also much larger from that of pervious $[Eu(hfa)_3(dpbp)_2]_n$ (η_{sens} = 40%).[34] The value of η_{sens} is related to the absorption band of joint metal block and effective enhancement of η_{sens} is affected by 3D-network coordination of Al^{3+} ions. The author consider that the polymeric structure effect from rigid zig-zag structure led to enhance the η_{sens}.[35]

Table 4-4. Photophysical properties of Eu^{3+} complexes in the solid state.

	Φ_{ff}[a]	Φ_{tot}[b]	η_{sens}[c]	τ_{obs}[d]	k_r[e]	k_{nr}[f]
	%	%	%	μs	s^{-1}	s^{-1}
$[Eu(hfa)_3AlCl_2(dppy)_4]_n^+$	72	52	72	800	9.0×10^2	3.5×10^2
$[Eu(hfa)_3PdCl_2(dppy)_2]_n$	1.3	-[g]	-	22	6.0×10^2	4.5×10^4
$[Eu(hfa)_3ZnCl_3(dppy)_2]_n$	59	28	48	850	7.0×10^2	4.8×10^2

[a] The intrinsic emission quantum yields were calculated from $\Phi_{ff} = k_r/(k_r+k_{nr}) = \tau_{obs}/\tau_{rad}$. [b] The total emission quantum yields Φ_{tot} were measured by integrating sphere (excitation at 370 nm). [c] The photo-sensitization efficiencies were calculated from $\eta_{sens} = \Phi_{tot}/\Phi_{ff}$. [d] Emission lifetime (τ_{obs}) of Eu^{3+} complexes were measured by excitation at 355 nm (Nd:YAG 3ω). [e] Radiative rate constants (k_r) for Eu^{3+} complexes estimated from $1/\tau_{rad} = A_{MD}n^3(I_{tot}/I_{MD})$.[31,32] [f] Non-radiative rate constant $k_{nr} = 1/\tau_{obs} - 1/\tau_{rad}$. [g] I could not observe. Emission was very weak.

The Eu-Pd complex shows a much smaller emission quantum yield. The author proposes that both the characteristic emission lifetime profile and smaller quantum yield of Eu-Pd are caused by the excited quenching from the emitting level of Eu^{3+} ions. The weak emission spectrum of joint Pd^{2+} block [*trans*-$PdCl_2(dppy)_2$] at 88 K was observed at around 760 nm, which is attributed to MLCT transitions from the Pd^{2+} ion to phosphine oxide ligands (see Figure 4-7).[36] The energy transfer diagram of Eu^{3+} complex linked with Pd^{2+} complexes is shown in Figure 4-8. The energy level of MLCT of the Pd^{2+} complex is lower than that of the excited $^5D_0$ state of Eu^{3+} ions. The small emission quantum yield of the Eu-Pd complex is caused by the energy transfer from luminescent Eu^{3+} blocks to joint Pd^{2+} blocks.

It is well known that the radiative and non-radiative rate constants of a lanthanide complex are dependent on the organic ligand or the solvent molecules.[37] In this study, all of the Eu^{3+} coordination sites in Eu^{3+} complexes were attached to three hfa and two dppy ligands. The photophysical properties of the Eu^{3+} complexes could be linked to moieties of metal ions (steric and electronic properties) in the joint metal blocks.

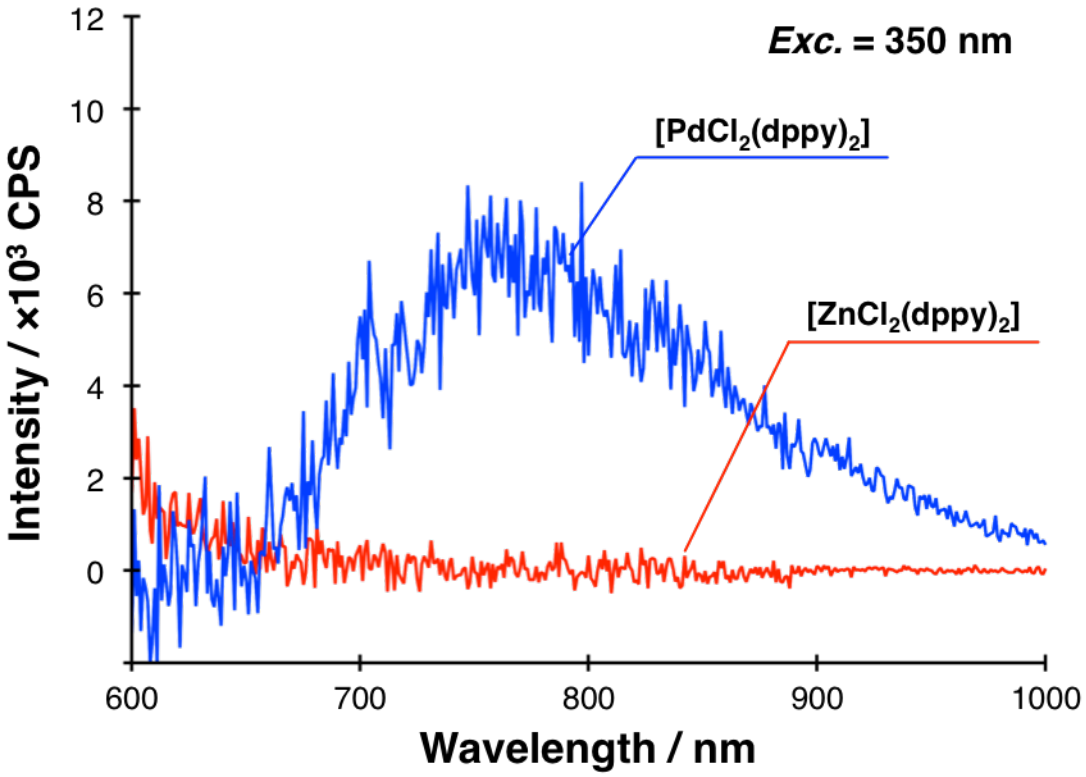

Figure 4-7. Emission spectra of (a) joint Pd^{2+} block: $[PdCl_2(dppy)_2]$ and (b) joint Zn^{2+} block: $[PdCl_2(dppy)_2]$ in the solid state at 88 K excited at 350 nm. Two type of photomultiplier tubes were used for measurements in UV-Vis and NIR regions, respectively.

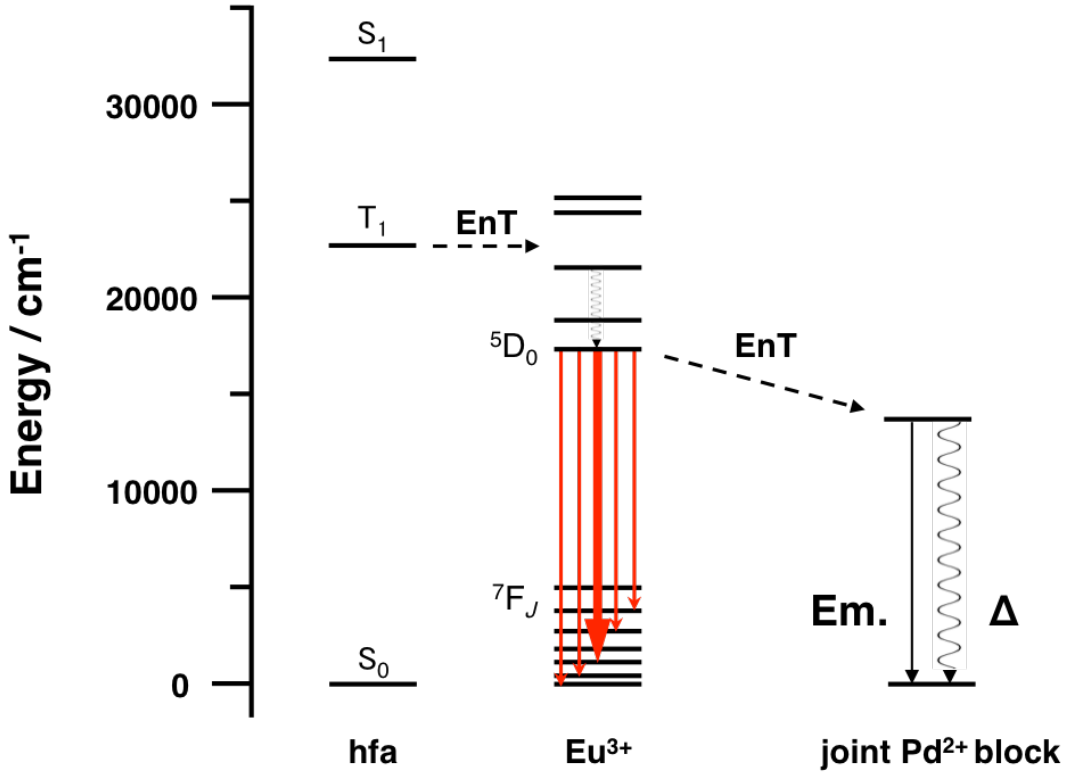

Figure 4-8. Energy diagram of Eu^{3+} complexes linked with joint Pd^{2+} blocks (EnT: energy transfer).

4.4 Conclusion

The Eu^{3+} complex composed of luminescent Eu^{3+} and joint Al^{3+} and *trans*-Pd^{2+} complexes were synthesized. The structures and photophysical properties of these Eu^{3+} complexes are dependent on the joint metal blocks. The emission quantum yield of the Eu-Al complex is the largest in these Eu^{3+} complex linked with joint metal blocks.

The author considers that the network structure of the Eu-Al complex based on the coordination structure of joint Al^{3+} blocks leads to a large radiative rate constant and small non-radiative rate constant, resulting in a high emission quantum yield (Φ_{ff} = 72%). The highly triplet energy level of joint metal blocks such as Al^{3+} ions might promote effective luminescence. In contrast, the emission quantum yields of Eu-Pd was found to be 1.3%. The small emission quantum yield of the Eu-Pd complex is caused by the energy transfer from luminescent Eu^{3+} ions to joint Pd^{2+} complexes. In this chapter, a new design of Eu^{3+} complex linked with joint metal blocks for control of geometrical structure and photophysical properties were provided.

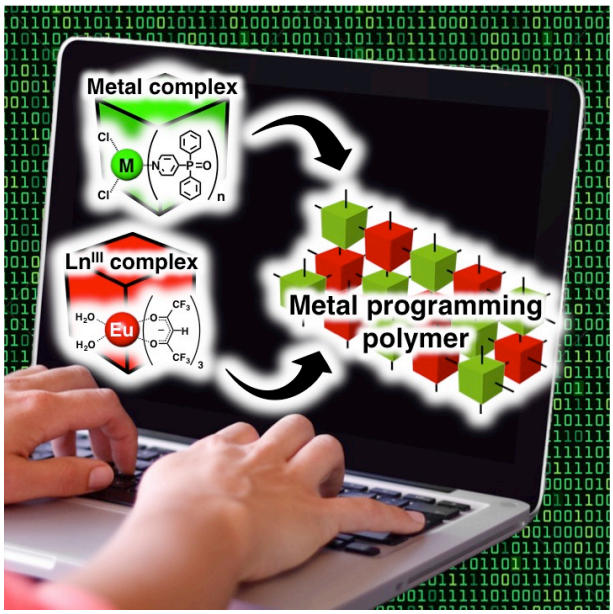

4.5 References

[1] H.-J. Son, S. Jin, S. Pawardhan, S. J. Wezenberg, N. C. Jeong, M. So, C. E. Wilmer, A. A. Sarjeant, G. C. Schatz, R. Q. Snurr, O. K. Farha, G. P. Wiederrecht, *J. Am. Chem. Soc.,* **2013**, *135*, 862-869.

[2] T. Zhang, W. Lin, *Chem. Soc. Rev.,* **2014**, *43*, 5982-5993.

[3] J. Lee, O. K. Farha, J. Roberts, K. A. Scheidt, S. T. Nguyen, J. T. Hupp, *Chem. Soc. Rev.,* **2009**, *38*, 1450-1459.

[4] B. Chen, L. Wang, F. Zapata, G. Qian, E. B. Lobkovsky, *J. Am. Chem. Soc.,* **2008**, *130*, 6718-6719.

[5] J. Heine, K. Müller-Buschbaum, *Chem. Soc. Rev.,* **2013**, *42*, 9232-9242.

[6] H. Zhang, L. Zhou, J. Wei, Z. Li, P. Lin, S. Du, *J. Mater. Chem.*, **2012**, *22*, 21210-21217.

[7] K. Miyata, Y. Konno, T. Nakanishi, A. Kobayashi, M. Kato, K. Fushimi, Y. Hasegawa, *Angew. Chem., Int. Ed.,* **2013**, *52*, 6413-6416.

[8] G. Shao, H. Yu, N. Zhang, Y. He, K. Feng, X. Yang, R. Cao, M. Gong, *Phys. Chem. Chem. Phys.,* **2014**, *16*, 695-702.

[9] S. J. Butler, L. Lamarque, R. Pal, D. Parker, *Chem. Sci.,* **2014**, *5*, 1750-1756.

[10] N. M. Shavaleev, S. V. Eliseeva, R. Scopelliti, J.-C. G. Bünzli, *Chem. -Eur. J.,* **2009**, *15*, 10790-10802.

[11] W.-S. Lo, J. Zhang, W.-T. Wong, G.-L. Law, *Inorg. Chem.,* **2015**, *54*, 3725-3727.

[12] O. A. Blackburn, N. F. Chilton, K. Keller, C. E. Tait, W. K. Myers, E. J. McInnes, A. M. Kenwright, P. D. Beer, C. R. Timmel, S. Faulkner, *Angew. Chem. Int. Ed.,* **2015**, *127*, 10933-10936.

[13] L. J. Daumann, D. S. Tatum, B. E. R. Snyder, C. Ni, G. Law, E. I. Solomon, K. N. Reymond, *J. Am. Chem. Soc.,* **2015**, *137*, 2816-2819.

[14] M. M. Nolasco, P. M. Vaz, V. T. Freitas, P. P. Lima, P. S. André, R. A. S. Ferreira, P. D. Vaz, P. Ribeiro-Claro, L. D. Carlos, *J. Mater. Chem. A,* **2013**, *1*, 7339-7350.

[15] V. Haquin, M. Etienne, C. Daiguebonne, S. Freslon, G. Calvez, K. Bernot, L. L. Pollès, S. E. Ashbrook, M. R. Mitchell, J.-C. Bünzli, S. V. Eliseeva, O. Guillou, *Eur. J. Inorg. Chem.,* **2013**, 3464-3476.

[16] L. Song, J. Wang, J. Hu, X. Liu, Z. Zhen, *J. Alloys Compd.,* **2009**, *473*, 201-205.

[17] A. Ishii, S. Kishi, H. Ohtsu, T. Iimori, T. Nakabayashi, N. Ohta, N. Tamai, M. Melnik, M. Hasegawa, Y. Shigesato, *ChemPhysChem.,* **2007**, *8*, 1345-1351.

[18] Y. Hasegawa, Y. Wada, S. Yanagida, *J. Photochem. Photobiol. C,* **2004**, *5*, 183-202.

[19] A. F. Kirby, F. S. Richardson, *J. Phys. Chem.,* **1983**, *87*, 2544-2522.

[20] K. Nakamura, Y. Hasegawa, H. Kawai, N. Yasuda, N. Kanehisa, Y. Kai, T. Nagamura, S. Yanagida, Y. Wada, *J. Phys. Chem. A,* **2007**, *111*, 3029-3037.

[21] K. Miyata, T. Nakagawa, R. Kawakami, Y. Kita, K. Sugimoto, T. Nakashima, T. Harada, T. Kawai, Y. Hasegawa, *Chem.-Eur. J.,* **2011**, *17*, 521-528.

[22] J. Ni, Y.-G. Wang, H.-H. Wang, L. Xu, Y.-Q. Zhao, Y.-Z. Pan, J.-J. Zhang, *Dalton Trans.,* **2014**, *43*, 352-360.

[23] A. Rana, P. K. Panda, *Chem. Commun.,* **2015**, *51*, 12239-12242.

[24] M. Sjödin, J. Gätjens, L.C. Tabares, P. Thuéry, V. L. Pecoraro, S. Un, *Inorg. Chem.,* **2008**, *47*, 2897-2908.

[25] M. Yamamoto, T. Nakanishi, Y. Kitagawa, K. Fushimi, Y. Hasegwa, *Mater. Lett.,* **2016**, *167*, 183-187.

[26] C. Lee, W. Yang, R. G. Parr, *Phys. Rev. B,* **1988**, *37*, 785-789.

[27] A. D. Becke, *J. Chem. Phys.,* **1993**, *98*, 5648-5652.

[28] C. Hu, U. Englert, *CrystEngComm,* **2002**, *4*, 20-25.

[29] A. Dimitrov, D. Heidemann, K. I. Khallow, E. Kemnitz, *Inorg. Chem.,* **2012**, *51*, 11612-11622.

[30] G. Dahm, E. Borré, C. Fu, S. Bellemin-Laponnaz, M. Mauro, *Chem.-Asian. J.,* **2015**, *10*, 2368-2379.

[31] L. Prodi, M. Maestri, R. Ziessel, V. Balzani, *Inorg. Chem.,* **1991**, *30*, 3798-3802.

[32] M. H. V. Werts, R. T. F. Jukes, J. W. Verhoeven, *Phys. Chem. Chem. Phys.* **2002**, *4*, 1542-1548.

[33] R. Pavithran, N. S. Saleesh Kumar, S. Biju, M. L. P. Reddy, S. A. Junior, R. O. Freire, *Inorg. Chem.,* **2006**, *45*, 2184-2192.

[34] K. Miyata, T. Ohba, A. Kobayashi, M. Kato, T. Nakanishi, K. Fushimi, Y. Hasegaw a, *ChemPlusChem,* **2012**, *77*, 277-280.

[35] Y. Hirai, T. Nakanishi, Y. Kitagawa, K. Fushimi, T. Seki, H. Ito, Y. Hasegawa, *Angew. Chem., Int. Ed.,* **2016**, *55*, 12059-12062.

[36] A. Krogul, J. Cedrowski, K. Wiktorska, W. P. Ozimiński, J. Skupińska, G. Litwinienko, *Dalton Trans.,* **2012**, *41*, 658-666.

[37] M. Morikawa, S. Tsunofuri, N. Kimizuka, *Langmuir,* **2013**, *29*, 12930-12930.

Chapter 5

Summary and outlook

5.1 Summary of the results

The author aimed to synthesize lanthanide coordination polymers crosslinked with metal complex and reveal that the photophysical propaties of lanthanide ions were effected by introducing metal complex ligands. The results obtained in this thesis were summarized as follows.

In **Chapter 1**, coordination structures, in particular how to construct coordination polyhedral, for lanthanide complexes were introduced. The scientific background about luminescent lanthanide complexes was also described.

In **Chapter 2**, a structural design of new luminescent lanthanide coordination polymers composed of Eu^{3+} complex and Zn^{2+} complexes are introduced. The Eu^{3+} coordination polymer $[Eu(hfa)_3(dppy)_2ZnCl_2]n$ (Eu-Zn) (hfa: hexafluoroacetylacetonato, dppy: 4-pyridyldiphenylphosphaneoxide) were synthesized by the complexation of $Eu(hfa)_3(H_2O)_2$ with $ZnCl_2(dppy)_2$. The structure was characterized using XRD and TG-DTA. The photophysical properties were estimated using the emission spectra, the

emission lifetimes, and the emission quantum yields. The emission quantum yields are larger then that of precursor $Eu(hfa)_3(H_2O)_2$. The emission quantum yield of Eu-Zn was found to be 59%. The preparations, structures and photophysical properties of Eu-Zn are demonstrated as a new luminescent Eu3+ coordination polymer for the first time.

In **Chapter 3**, luminescent Tb^{3+} complex with hexafluoroacetylacetone (hfa) ligand shows back energy transfer (BEnT), which leads to high temperature sensitivity for thermo-sensitive paint. Ligand-assisted BEnT by introducing of phosphine oxide into $Tb(hfa)_3$ complex defines as an effect of controlling activation energy (ΔE_a) and frequency factor (A) in BEnT process between Tb^{3+} ion and hfa ligands. From Arrhenius analysis based on the temperature-dependent emission lifetime measurements, the ΔE_a and A values are smaller for the polynuclear Tb^{3+} complexes than for the mononuclear Tb^{3+} complexes. The difference of ΔE_a and A value between polynuclear and mononuclear Tb^{3+} complexes are caused by the formation of different excited states.

In **Chapter 4**, Lanthanide (Ln^{3+}) complexes composed of luminescent Eu^{3+} complex and joint metal blocks (Al^{3+} and Pd^{2+} complexes) are reported. The Eu^{3+} complexes $[Eu(hfa)_3(dppy)_2PdCl_2]_n$ (Eu-Pd) and $[Eu(hfa)_3(dppy)_4AlCl_3]_n$ (Eu-Al) (hfa: hexafluoroacetylacetonato, dppy: 4-pyridyldiphenylphosphine oxide) were synthesized by the complexation of $[Eu(hfa)_3(H_2O)_2]$ with $[MCl_n(dppy)_m]$ (M = Pd^{2+} and Al^{3+}). These predicted structures were estimated using single-crystal X-ray structural analyses and DFT calculations. Photophysical properties of these complexes were evaluated based on the emission lifetimes and emission quantum yields. The emission quantum yields

are dependent on the moiety of the joint metal blocks. Eu-Al complex shows the largest emission quantum yield (Φ_{ff} = 72%). In contrast, the emission quantum yield of Eu-Pd is found to be 1.3%. The structures and photophysical properties of Eu^{3+} complexes linked with joint metal blocks are demonstrated.

5.2 Outlook

Novel lanthanide coordination polymers cross-linked with Zn^{2+}, Pd^{2+}, and Al^{3+} complex as bridging ligands were demonstrated for the first time. The photophysical properties of these lanthanide coordination polymers were dependent on structural and electronic properties of each metal complex ligand. In addition, the author proposed the new molecular design guideline for lanthanide complexeswith thermo-sensitivity function. In lanthanide complexes with thermo-sensitivity material, the polymer-type structure exhibit a tendency to remarkable thermo-sensitivity in a wide temperature range.

In this thesis, the relationship of the photophysical properties between the metal complexes and lanthanide complexes in the identical polymer structure was clarified for the first time. The author hopes that this thesis contributes to build the foundation of the science of lanthanide complex. Based on this thesis, the author also hope to contribute the research and development of thermo-sensitive paints, such as further high sensitivity and sensitivity control of temperature region.

List of publications

[1] **M. Yamamoto**, T. Nakanishi, Y. Kitagawa, K. Fushimi, Y. Hasegawa, “Luminescent Eu(III) coordination polymer cross-linked with Zn(II) complexes”, *Materials Letters*, **2016**, *167*, 183-187.

[2] **M. Yamamoto**, T. Nakanishi, Y. Kitagawa, T. Seki, H. Ito, K. Fushimi, Y. Hasegawa, “Synthesis and Photophysical Properties of Eu(III) Complexes with phosphine oxide ligands including metal ions”*, Bulletin of the Chemical Society of Japan*, **2017**, *91*, 6-11.

[3] **M. Yamamoto**, Y. Kitagawa, T. Nakanishi, K. Fushimi, Y. Hasegawa, “Ligand-assisted Back Energy Transfer in Luminescent Tb(III) Complexes for Thermo-sensing Properties”*, Chemistry A European Journal*, **2018**, in press. DIO: 10.1002/chem.201804392

Other publications

[1] Y. Suzuki, H. Moritomo, A. Fuji, K. Satomi, J. Kawamata, **M. Yamamoto**, Y. Hasegawa, “Three-photon-induced Luminescence of Europium Acetylacetonate-type Complexes”, *Chemistry Letters*, **2016**, *45*, 538-540.

[2] S. Murai, M. Saito, H. Sakamoto, **M. Yamamoto**, R. Kamakura, T. Nakanishi, K. Fujita, M. A. Verschuuren, Y. Hasegawa, K. Tanaka, “Directional outcoupling of photoluminescence from Eu(III)-complex thin films by plasmonic array”, *APL Photonics*, **2017**, *2*, 026104.

[3] Y. Hasegawa, S. Tateno, **M. Yamamoto**, T. Nakanishi, Y. Kitagawa, T. Seki, H. Ito, K. Fushimi, “Effective Photo- and Triboluminescent Eu(III) Coordination Polymers with Rigid Triangular Spacer Ligands”, *Chemistry A European Journal*, **2017**, *23*, 2666-2672.

[4] M. Saito, S. Murai, H. Sakamoto, **M. Yamamoto**, R. Kamakura, T. Nakanishi, K. Fujita, Y. Hasegawa, K. Tanaka, “Effect of Cylinder Height on Directional Photoluminescence from Highly Luminous Thin Films on Periodic Plasmonic Arrays”, *MRS Advances*, **2017**, *2*, 173-178.

[5] T. Koizuka, **M. Yamamoto**, Y. Kitagawa, T. Nakanishi, K. Fushimi, Y. Hasegawa, “Photosensitized luminescence of highly thermostable mononuclear Eu(III) complexes with π-expanded β-diketonate ligands”, *Bulletin of the Chemical Society of Japan*, **2017**, *90*, 1287-1292.

List of presentations

[1] ○**山本昌紀**, 中西貴之, 北川裕一, 関朋宏, 伊藤肇, 伏見公志, 長谷川靖哉, 「平面四配位Pd(II)錯体で架橋されたEu(III)配位高分子の合成と光物性」(口頭), 日本化学会第 94 春季年会, 名古屋大学, 2014. 3. 28.

[2] ○**M. Yamamoto**, T. Nakanishi, K. Fushimi, Y. Hasegawa, "Synthesis and photophysical properties of Eu(III) coordination polymers cross-linked with transition metal complexes" (Poster), 10th International Workshop on Supramolecular Nanoscience of Chemically Programmed Pigments (SNCPP14), Ritumeikan Univ., Japan, 2014. 5. 31.

[3] ○**山本昌紀**, 中西貴之, 北川裕一, 関朋宏, 伊藤肇, 伏見公志, 長谷川靖哉, 「金属錯体で架橋した Eu(III)配位高分子の合成と光物性」(ポスター), 第 26 回配位化合物の光化学討論会, 首都大学東京, 2014. 8. 6.

[4] ○**M. Yamamoto**, T. Nakanishi, T. Seki, H. Ito, K. Fushimi, Y. Hasegawa, " Synthesis of Eu(III) coordination polymers cross-linked with metal complexes directed to create 3D coordination polymers and photophysical properties"(Poster), 15th Chitose International Forum on Photonics Science & Technology (CIF'15), Chitose institute of science and technology, Japan, 2014. 10. 2.

[5] ○**山本昌紀**, 中西貴之, 北川裕一, 関朋宏, 伊藤肇, 伏見公志, 長谷川靖哉, 「金属錯体で架橋された Eu(III)錯体ポリマーの光物性」(ポスター), 2014 年光化学討論会, 北海道大学, 2014. 10. 13.

[6] ○**山本昌紀**, 中西貴之, 北川裕一, 関朋宏, 伊藤肇, 伏見公志, 長谷川靖哉, 「金属錯体を用いた高次構造を有する Eu(III)錯体ポリマーの光物性評価」(ポスター), 第 4 回 CSJ 化学フェスタ, タワーホール船堀, 2014. 10. 15.

[7] ○**M. Yamamoto**, T. Nakanishi, T. Seki, H. Ito, K. Fushimi, Y. Hasegawa, "Synthesis and photophysical properties of Eu(III) coordination polymers cross-linked with Pd(II) complexes" (Poster), The 2nd International Symposium on AMBITIOUS LEADER'S PROGRAM Fostering Future Leaders to Open New Frontiers in Materials Science, Hokkaido Univ., Japan, 2014. 12. 11.

[8] ○**山本昌紀**, 中西貴之, 北川裕一, 関朋宏, 伊藤肇, 伏見公志, 長谷川靖哉, 「金属錯体で架橋した Eu(III)錯体ポリマーの合成と光物性評価」(口頭), 北海道支部 2015 年夏季研究発表会, 北海道教育大学函館校, 2015. 7. 18.

[9] ○**山本昌紀**, 中西貴之, 北川裕一, 関朋宏, 伊藤肇, 伏見公志, 長谷川靖哉, 「金属架橋部位に依存した希土類錯体ポリマーの発光特性評価」(ポスター), 2015 年光化学討論会, 大阪市立大学, 2015. 9. 9.

[10] ○**山本昌紀**, 中西貴之, 北川裕一, 関朋宏, 伊藤肇, 伏見公志, 長谷川靖哉, 「金属架橋部位に依存した Eu(III)錯体ポリマーの発光特性」(ポスター), 第 5 回 CSJ 化学フェスタ 2015, タワーホール船堀, 2015. 10. 15.

[11] ○**M. Yamamoto**, T. Nakanishi, Y. Kitagawa, T. Seki, H. Ito, K. Fushimi, Y. Hasegawa, "Photophysical properties of lanthanide coordination polymers dependent on metal complex ligands" (Poster), Third International Symposium on the Photofunctional Chemistry of Complex Systems (ISPCCS2015), Makena Beach & Golf Resort, USA, 2015. 12. 13.

[12] ○**M. Yamamoto**, T. Nakanishi, Y. Kitagawa, T. Seki, H. Ito, K. Fushimi, Y. Hasegawa, "Luminescent Eu(III) coordination polymers cross-linked with transition metal ions"(Poster), The 2015 International Chemical Congress of Pacific Basin Societies (Pacifichem 2015), Hawaii Convention Center, USA, 2015. 12. 18

[13] ○**山本昌紀**, 中西貴之, 北川裕一, 関朋宏, 伊藤肇, 伏見公志, 長谷川靖哉, 「*p*-および *d*-金属錯体で架橋した新規希土類錯体ポリマーの合成と光物性評価」(ポスター), 元素ブロック高分子材料の創出 第 4 回合同修士論文発表会, 大阪府立大学, 2016. 3. 4.

[14] ○**M. Yamamoto**, T. Nakanishi, Y. Kitagawa, K. Fushimi, Y. Hasegawa, "Photophysical properties of lanthanide coordination polymers cross-linked with metal complexes" (Poster), The International Symposium on Lanthanide Coordination Chemistry (ISLCC 2016), Aoyama Gakuin Univ., Japan, 2016. 6. 4.

[15] ○**M. Yamamoto**, T. Nakanishi, Y. Kitagawa, K. Fushimi, Y. Hasegawa, "Photophysical properties of Eu(III) coordination polymers cross-linked with Zn(II) complexes"(Poster), Rare Earths 2016 in Sapporo, Hokkaido Univ., Japan, 2016. 6. 9.

[16] ○**山本昌紀**, 中西貴之, 北川裕一, 関朋宏, 伊藤肇, 伏見公志, 長谷川靖哉, 「金属架橋で架橋された Eu(III)錯体ポリマーの合成と光物性評価」（ポスター）,第 16 回北大若手研究者交流会, 北海道大学, 2016. 8. 19.

[17] ○**山本昌紀**, 立野栞, 中西貴之, 北川裕一, 伏見公志, 長谷川靖哉,「希土類錯体ポリマーにおけるトリボ発光の機能評価」（ポスター）, 2016 年光化学討論会, 東京大学, 2016. 9. 7.

[18] ○**山本昌紀**, 中西貴之, 北川裕一, 関朋宏, 伊藤肇, 伏見公志, 長谷川靖哉, 「金属錯体部位に依存した Eu(III)錯体ポリマーの発光特性評価」(英語口頭), 第 65 回高分子討論会, 神奈川大学, 2016. 9. 15.

[19] ○**M. Yamamoto**, T. Nakanishi, Y. Kitagawa, T. Seki, H. Ito, K. Fushimi, Y. Hasegawa, “Synthesis and photophysical properties of three dimensional Eu(III) coordination polymers linked with transition metal complexes” (Poster), HOKUDAI-NCTU Joint Symposium on Nano, Photo and Bio Sciences in 2016, Hokkaido Univ., Japan, 2016. 10. 4.

[20] ○**山本昌紀**, 立野栞, 中西貴之, 北川裕一, 伏見公志, 長谷川靖哉,「Eu(III)錯体ポリマーにおけるトリボ発光の機能評価」（ポスター）,第 6 回 CSJ 化学フェスタ 2016, タワーホール船堀, 2016. 11. 15.

[21] ○**M. Yamamoto**, T. Nakanishi, Y. Kitagawa, T. Seki, H. Ito, K. Fushimi, Y. Hasegawa, “Synthesis and photophysical properties of novel coordination polymers composed of luminescent Europium and metal joint blocks” (Poster), 28th Rare Earth Research Conference, Iowa state Univ., Ames, Iowa, USA, 2017. 6. 19.

[22] ○**山本昌紀**, 北川裕一, 中西貴之, 伏見公志, 長谷川靖哉,「ホスフィンオキシド配位子との特異的な相互作用による Tb(III)錯体の Back energy transfer への影響とその効果」(英語口頭), 2017 年光化学討論会, 東北大学, 2017. 9. 4.

[23] ○**M. Yamamoto**, T. Nakanishi, Y. Kitagawa, T. Seki, H. Ito, K. Fushimi, Y. Hasegawa, “Synthesis and photophysical properties of Eu(III) coordination polymers linked with metal complexes”(Poster), 6th German-Japanese Joint seminar High-speed Molecular Imaging Technology for Interdisciplinary Research, University of Hohenheim, Stuttgart, Germany, 2017. 9. 26.

[24] ○**山本昌紀**, 北川裕一, 中西貴之, 伏見公志, 長谷川靖哉,「ホスフィンオキシド配位子に依存した $Tb(hfa)_3$ 錯体の感温特性への影響」（ポスター）, 第 13 回学際領域における分子イメージングフォーラム 2017, JAXA　調布航空宇宙センター, 2017. 11. 17.

[25] ○**山本昌紀**, 北川裕一, 中西貴之, 伏見公志, 長谷川靖哉,「異なるホスフィンオキシド配位子の導入による $Tb(hfa)_3$ 錯体の逆エネルギー移動過程への影響」（口頭）, 第 30 回配位化合物の光化学討論会, 札幌・定山渓ビューホテル, 2018. 7. 14.

List of patents

[1] 長谷川靖哉, **山本昌紀**, 中西貴之, 伏見公志,「配位子、高分子錯体およびその製造方法」特願 2014-023813　2014. 2. 10.

[2] 川俣純, 鈴木康孝, 守友博紀, 藤井旺成, 長谷川靖哉, **山本昌紀**,「三光子励起により発光する発光性組成物」特願 2014-205115　2014. 10. 3.

[3] 長谷川靖哉, **山本昌紀**, 中西貴之, 伏見公志,「配位子、高分子錯体およびその製造方法」　特願 PCT/JP2015/ 053463　2015. 2. 10.

List of awards

[1] 2015 年 10 月
第 5 回 CSJ 化学フェスタ 2015 において、**優秀ポスター賞** を受賞

[2] 2016 年 8 月
第 16 回北大若手研究者交流会において、**優秀ポスター賞** を受賞